

1 Mediterranean intense desert dust outbreaks and their vertical structure based on 2 remote sensing data

3

4 A. Gkikas¹, S. Basart¹, N. Hatzianastassiou², E. Marinou^{3,9}, V. Amiridis³, S. Kazadzis^{4,5}, J. Pey⁶, X.
5 Querol⁷, O. Jorba¹, S. Gassó⁸ and J.M. Baldasano^{1,8}

6

7 ¹Earth Sciences Department, Barcelona Supercomputing Center, Barcelona, Spain

8 ²Laboratory of Meteorology, Department of Physics, University of Ioannina, Ioannina, Greece

9 ³Institute for Astronomy, Astrophysics, Space Applications and Remote Sensing, National Observatory of Athens, Athens,
10 15236, Greece

11 ⁴Physikalisch-Meteorologisches Observatorium Davos, World Radiation Center, Switzerland

12 ⁵Institute of Environmental Research and Sustainable Development, National Observatory of Athens, Athens, Greece

13 ⁶Spanish Geological Survey. Zaragoza IGME Unit, Zaragoza, Spain

14 ⁷Institute of Environmental Assessment and Water Research, IDÆA-CSIC C/Jordi Girona, 18–26, 08034 Barcelona, Spain

15 ⁸Environmental Modelling Laboratory, Technical University of Catalonia, Barcelona, Spain

16 ⁹Laboratory of Atmospheric Physics, Department of Physics, Aristotle University of Thessaloniki, Thessaloniki, Greece

17

18

19 Corresponding author: Antonis Gkikas (antonis.gkikas@bsc.es)

20

21 Abstract

22 The main aim of the present study is to describe the vertical structure of the intense Mediterranean
23 dust outbreaks, based on the use of satellite and surface-based retrievals/measurements. Strong and
24 extreme desert dust (DD) episodes are identified at $1^\circ \times 1^\circ$ spatial resolution, over the period Mar. 2000
25 – Feb. 2013, through the implementation of an updated objective and dynamic algorithm. According to
26 the algorithm, strong *DD* episodes occurring at a specific place correspond to cases in which the daily
27 aerosol optical depth at 550nm (AOD_{550nm}) exceeds or equals the long-term mean AOD_{550nm} (*Mean*)
28 plus two standard deviations (*Std*) value being smaller than $Mean+4*Std$. Extreme *DD* episodes
29 correspond to cases in which the daily AOD_{550nm} value equals or exceeds $Mean+4*Std$. For the
30 identification of *DD* episodes additional optical properties (Ångström exponent, fine fraction, effective
31 radius and Aerosol Index) derived by the MODIS-Terra & Aqua (also *AOD* retrievals), OMI-Aura and
32 EP-TOMS databases are used as inputs. According to the algorithm using MODIS-Terra data, over the
33 period Mar. 2000 – Feb. 2013, strong *DD* episodes occur more frequently (up to 9.9 episodes yr^{-1}) over

34 the western Mediterranean while the corresponding frequencies for the extreme ones are smaller (up to
35 3.3 episodes yr^{-1} , central Mediterranean Sea). In contrast to their frequency, dust episodes are more
36 intense ($AODs$ up to 4.1), over the central and eastern Mediterranean Sea, off the northern African
37 coasts. Slightly lower frequencies and higher intensities are found when the satellite algorithm operates
38 based on MODIS-Aqua retrievals, for the period 2003–2012. The consistence of the algorithm is
39 successfully tested through the application of an alternative methodology for the determination of DD
40 episodes, which produced similar features of the episodes' frequency and intensity, with just slightly
41 higher frequencies and lower intensities. The performance of the satellite algorithm is assessed against
42 surface-based daily data from 109 sun-photometric (AERONET) and 22 PM_{10} stations. The agreement
43 between AERONET and MODIS AOD is satisfactory ($R=0.505-0.750$) improving considerably when
44 MODIS level 3 retrievals with higher sub-grid spatial representativeness and homogeneity are
45 considered. The CALIOP vertical profiles of pure and polluted dust observations and the associated
46 total backscatter coefficient at 532 nm (β_{532nm}), indicate that dust particles are mainly detected between
47 0.5 and 6 km, though they can reach 8 km between the parallels 32° N and 38° N in warm seasons,
48 while an increased number of CALIOP dust records at higher altitudes is observed with increased
49 latitude, northwards to 40° N, revealing an ascending mode of the dust transport. However, the overall
50 intensity of DD episodes is maximum (up to $0.006 \text{ km}^{-1} \text{ sr}^{-1}$) below 2 km and at the southern parts of
51 the study region (30° N - 34° N). Additionally, the average thickness of dust layers gradually decreases
52 from 4 to 2 km moving from south to north. In spring, dust layers of moderate-to-high β_{532nm} values (\sim
53 $0.004 \text{ km}^{-1} \text{ sr}^{-1}$) are detected over the Mediterranean (35° N - 42° N), extending from 2 to 4 km. Over
54 the western Mediterranean, dust layers are observed between 2 and 6 km, while their base height is
55 decreased down to 0.5 km for increasing longitudes underlying the role of topography and thermal
56 convection. The vertical profiles of CALIOP β_{532nm} confirm the multilayered structure of the
57 Mediterranean desert dust outbreaks on both annual and seasonal basis, with several dust layers of
58 variable geometrical characteristics and intensities. A detailed analysis of the vertical structure of
59 specific DD episodes using CALIOP profiles reveals that consideration of the dust vertical structure is
60 necessary when attempting comparisons between columnar MODIS AOD retrievals and ground PM_{10}
61 concentrations.

62 1. Introduction

63 The Mediterranean basin, due to its proximity to the major dust source arid areas of Northern
64 Africa and Middle East (Middleton and Goudie, 2001; Prospero et al., 2002; Ginoux et al., 2012) is
65 frequently affected by transported high dust loads referred to as episodes or events. The suspension and

66 accumulation of mineral particles into the atmosphere over the Saharan and Arabian Peninsula's
67 deserts are determined by various factors such as the enhanced turbulence, soil conditions (reduced
68 vegetation cover and soil moisture), reduced precipitation amounts, latitudinal shift of the Intertropical
69 Convergence Zone (*ITCZ*) as well as by small scale meteorological processes (e.g. haboobs). However,
70 dust particles can be transported far away from their sources, mainly towards the Atlantic Ocean (e.g.
71 Prospero and Lamb, 2003; Ben-Ami et al., 2010; Huang et al., 2010) and Europe (e.g. Mona et al.,
72 2006; Mona et al., 2012; Papayannis et al., 2008; Basart et al., 2012; Bègue et al., 2012; Pey et al.,
73 2013), favored by the prevailing atmospheric circulation patterns, from planetary to synoptic scales.
74 Due to their frequent transport in the Mediterranean, mineral dust particles, constitute the predominant
75 aerosol type there (Barnaba and Gobbi, 2004; Basart et al., 2012), as shown by the good agreement, in
76 spatial terms, between the geographical distributions of dust episodes' *AOD* (Gkikas et al., 2013) and
77 average *AOD* conditions (Papadimas et al., 2008).

78 Dust particles play an important role for the shortwave (*SW*) and longwave (*LW*) radiation budget
79 (e.g. Kaufman et al., 2002; Tegen et al., 2003; Heinold et al., 2008) and climate (IPCC, 2013). They
80 affect atmospheric heating/cooling rates (e.g. Mallet et al., 2009) while they can also result in a
81 modification of atmospheric dynamics and large atmospheric circulations like monsoons (e.g. Lau et
82 al., 2006; Bollasina et al., 2011), cloud properties and precipitation (e.g. Huang et al., 2006; Solmon et
83 al., 2008). Moreover, it has been shown that the consideration of their radiative impacts in numerical
84 simulations can improve the forecasting accuracy of weather models (Pérez et al., 2006). Dust particles
85 also affect air quality in urban areas (Basart et al., 2012) causing adverse health effects (Díaz et al.,
86 2012; Karanasiou et al., 2012; Pérez García-Pando et al., 2014). All these consequences of dust aerosol
87 are relevant and maximize under maximum dust loads, namely dust episodes, highlighting thus the
88 significance of analyzing the spatial and temporal characteristics of such events. To this aim, many
89 studies have been carried out using either surface (e.g. Cachorro et al., 2006) or satellite (e.g. Moulin et
90 al., 1998) observations, as well as modelling techniques (e.g. Heinold et al., 2007) focusing on the
91 broader Mediterranean area. These studies have been done either for specific cases (e.g. Kubilay et al.,
92 2003; Balis et al., 2006) or for extended periods at specific locations (e.g. Meloni et al., 2007; Toledano
93 et al., 2007a; Gobbi et al., 2013; Mona et al., 2014). Recently, Gkikas et al. (2013) developed an
94 objective and dynamic algorithm relying on satellite retrievals, which enabled an overall view of dust
95 episodes over the entire Mediterranean and the characterization of their regime (i.e., frequency of
96 occurrence, intensity and duration).

97 Extensive research has been also carried out on the mechanisms of Mediterranean dust outbreaks.
98 Therefore, several mechanisms and processes of transport, apart from dust emissions in source areas,
99 have been proposed as controlling factors. Moulin et al. (1997) showed that the exported dust loads
100 from Northern Africa towards the Atlantic Ocean and the Mediterranean are controlled by the phase of
101 the North Atlantic Oscillation (*NAO*). Other studies, focused on the description of atmospheric
102 circulation characteristics favoring the occurrence of desert dust outbreaks over the central (Barkan et
103 al., 2005; Meloni et al., 2008) or western (Querol et al., 1998; Rodriguez et al., 2001; Salvador et al.,
104 2014) Mediterranean, but on a synoptic scale. An objective classification, based on multivariate
105 statistical methods, of the atmospheric circulation patterns related to dust intrusions over the
106 Mediterranean, has been presented by Gkikas et al. (2015) and Varga et al. (2014).

107 The concentration of dust aerosols in the Mediterranean is characterized by strong spatial and
108 temporal variability, associated with the seasonal variability of cyclones dominating or affecting the
109 broader Mediterranean basin (Trigo et al., 2002). According to Moulin et al. (1998), dust *AOD* levels
110 are higher in spring and summer compared to the wet seasons of the year. Moreover, dust intrusions are
111 mainly recorded over the southeastern Mediterranean in spring and winter, over the western parts in
112 summer and over the central ones in autumn (Gkikas et al., 2013).

113 Dust transport over the Mediterranean is characterized by a multi-layered structure (Hamonou et
114 al., 1999; Papayannis et al., 2008) in contrast to the Atlantic Ocean, which is well confined to the
115 Saharan Air Layer (*SAL*, Karyampudi et al., 1999). The vertical distribution of dust load into the
116 troposphere as well as the profile of dust aerosols' optical properties at different altitudes, control the
117 impacts on atmospheric dynamics induced by the mineral particles (Zhang et al., 2013). In order to
118 describe the geometrical features of dust transport, many researchers have used ground lidar
119 measurements, model simulations (Alpert et al., 2004; Kishcha et al. 2005) or they have relied on a
120 synergistic use of satellite observations and ground lidar profiles (Berthier et al., 2006). The vertical
121 extension of the Saharan dust intrusions over Europe, during the period 2000-2002, was the subject of a
122 comprehensive study by Papayannis et al. (2008), who used lidar measurements from the EARLINET
123 (European Aerosol Research Lidar Network, Bösenberg et al., 2003). Over the Mediterranean stations,
124 the mean base, top and thickness of dust layers was found to vary from 1356 to 2980 m, 3600 to 5900
125 m and 726 to 3340 m, respectively. According to the obtained results, tracers of dust particles can be
126 detected up to 10 km, as also reported by Gobbi et al. (2000), who studied a Saharan dust event in
127 Crete (south Greece) during spring of 1999.

128 Several similar studies have been also performed for specific Mediterranean locations based on
129 EARLINET lidar measurements. For example, Mona et al. (2006) analyzed the vertical structure of 112
130 Saharan intrusions that occurred over Potenza (Italy), from May 2000 to April 2003. The authors found
131 that these outbreaks are confined between 1.8 and 9 km while their mass center is located at 3.5 km
132 above sea level (a.s.l.). A similar analysis for Athens and Thessaloniki over the period 2000-2002, was
133 conducted by Papayannis et al. (2005) who demonstrated that dust layers are recorded mainly between
134 2 and 5 km while their thicknesses vary from 0.2 to 3 km. The geometrical characteristics of dust layers
135 over Athens, during the period 2004 – 2006, have been also presented by Papayannis et al. (2009), who
136 pointed out that the center of mass of dust layers is located at 2.9 km being in a very good agreement
137 with Kalivitis et al. (2007) findings (around 3 km) for the eastern Mediterranean. Additionally, the
138 authors reported that the dust layers mainly extend from 1.6 to 5.8 km while mineral particles can be
139 detected, at very low concentrations, up to 8 km a.s.l.. Gobbi et al. (2013) found that dust plumes, over
140 Rome, mainly extend from 0 to 6 km while their center of mass is located at around 3 km. In the
141 southern parts of Italy (Potenza), dust layers' base is found between 2 and 3 km, their geometrical
142 height extends from 2.5 to 4 km while tracers of dust particles can be detected up to 10 km, based on a
143 dataset of 310 dust events analyzed by Mona et al. (2014). Finally, Pisani et al. (2011) stated that the
144 mean base and top of dust layers is found at 1.5 km and 4.6 km a.s.l., respectively, while their mean
145 thickness is equal to 3.1 km, based on a statistical analysis of 45 desert dust episodes observed over
146 Naples (Italy), from May 2000 to August 2003.

147 Surface-based lidar measurements like those used in the aforementioned studies provide useful
148 information about the geometrical and optical properties of dust layers, but they are representative only
149 for specific locations. Yet, a more complete knowledge about the vertical structure of dust outbreaks is
150 necessary in order to adequately understand and determine their possible effects. The limitation
151 imposed by the use of surface-based lidar observations can be overcome by utilizing accurate satellite
152 retrievals, as a complementary tool, which provide extended spatial coverage. Since 2006, vertical
153 resolved observations of aerosols and clouds from space were made possible thanks to the CALIOP
154 (Cloud-Aerosol Lidar with Orthogonal Polarization) lidar flying onboard the CALIPSO (Cloud-
155 Aerosol Lidar and Infrared Pathfinder Satellite Observations) satellite (Winker et al., 2009). Based on
156 CALIOP observations, Liu et al. (2008) analyzed the global vertical distribution of aerosols for one
157 year, while other studies focused on the vertical structure of dust outflows towards the Atlantic Ocean
158 (e.g. Ben-Ami et al., 2009; Adams et al., 2012; Tsamalis et al., 2013) and the Pacific Ocean (e.g.
159 Eguchi et al., 2009; Hara et al., 2009). On the contrary, over the broader Mediterranean area, only a

160 small number of studies has been made aiming at describing the vertical distribution of dust aerosols
161 (Amiridis et al., 2013) or specifying the vertical structure of dust events (Amiridis et al., 2009).
162 Nevertheless, they only dealt with a single dust event (18-23 May 2008, Amiridis et al., 2009) and thus
163 cannot satisfy the need to know the general vertical structure of Mediterranean dust episodes.

164 The main target of the present study is to describe the Mediterranean desert dust outbreaks' vertical
165 structure. For this purpose, satellite retrievals derived by the MODIS-Terra/Aqua, EP-TOMS, OMI-
166 Aura and CALIOP-CALIPSO databases (Section 2) are used in a synergistic way. The dust outbreaks
167 are identified with an objective and dynamic algorithm, which uses appropriate aerosol optical
168 properties representative of suspended particles' load, size and nature (Section 3). First, the outputs of
169 the satellite algorithm are compared versus surface measurements provided by AERONET or PM_{10}
170 stations, located within the study region (Section 4.1). Additionally, useful information about various
171 optical and physical properties under intense dust episodes conditions is also derived from the
172 aforementioned analysis. Then, the primary characteristics of the intense Mediterranean desert dust
173 (*DD*) episodes, namely their frequency and intensity, are described in Section 4.2. Just in order to
174 assess the consistency of the algorithm' concept, an alternative methodology for the determination of
175 *DD* episodes is also applied and the obtained results are inter-compared with the basic methodology.
176 For the identified *DD* episodes, collocated CALIOP-CALIPSO vertical feature mask and total
177 backscatter coefficient at 532 nm retrievals are used in order to describe the annual and seasonal
178 variability of dust outbreaks' vertical extension over the Mediterranean (Section 4.3). Moreover, in
179 Section 4.4, a thorough analysis of specific Mediterranean *DD* episodes is made, in order to examine
180 how the vertical distribution of desert dust outbreaks can affect the agreement between MODIS *AOD*
181 and PM_{10} data. Finally, the summary and conclusions are drawn in Section 5.

182

183 **2. Satellite and surface-based data**

184 The different types of satellite retrievals that have been used as inputs to the objective and dynamic
185 satellite algorithm are described below, namely the MODIS (Section 2.1.1), EP-TOMS and OMI-Aura
186 (Section 2.1.2) databases. Also, CALIOP-CALIPSO vertically resolved satellite data, coincident with
187 the identified desert dust outbreaks by the satellite algorithm, are described in Section 2.1.3. Finally,
188 surface-based sun-photometric AERONET retrievals and PM_{10} concentrations, both used for the
189 comparison against the satellite algorithm's outputs, are described in Sections 2.2.1 and 2.2.2,
190 respectively.

191

192 2.1 Satellite data

193 2.1.1 MODIS

194

195 MODERate resolution Imaging Spectroradiometer (MODIS) onboard the Terra and Aqua satellites –
196 with daytime local equator crossing time at 10:30 and 13:30 UTC, respectively, and 2330 km viewing
197 swath – acquires measurements at 36 spectral bands between 0.415 and 14.235 μm with varying spatial
198 resolution of 250, 500 and 1000 m. Observations from Terra and Aqua are made continuously since
199 February 2000 and July 2002, respectively, and are available from the LAADS website
200 (<ftp://ladsweb.nascom.nasa.gov/>). Aerosol optical properties are retrieved through the Dark Target (DT)
201 algorithm (see e.g. Kaufman et al., 1997, 2001; Tanré et al., 1997; Levy et al., 2003; Remer et al.,
202 2005) where different assumptions are considered depending on the underlying surface type (land or
203 ocean). Several evaluation studies (e.g. Remer et al., 2008; Papadimas et al., 2009; Levy et al., 2010;
204 Nabat et al., 2013) have shown that aerosol optical depth (AOD) can be retrieved satisfactorily by
205 MODIS, nevertheless its performance is better over sea (uncertainty equal to $\pm 0.03 \pm 0.05 \times AOD$,
206 Remer et al., 2002) than over land ($\pm 0.05 \pm 0.15 \times AOD$, Levy et al., 2010).

207 The following daily MODIS-Terra and MODIS-Aqua Collection 051 (C051) level 3 satellite data
208 (MOD08_D3 and MYD08_D3 files) provided at $1^\circ \times 1^\circ$ latitude-longitude spatial resolution are used:
209 (i) AOD_{550nm} , (ii) Ångström exponent over land ($\alpha_{470-660nm}$), (iii) Ångström exponent over ocean
210 ($\alpha_{550-865nm}$), (iv) fine-mode fraction (FF) of AOD over land and ocean and (v) Effective radius over
211 ocean (r_{eff}). It must be mentioned that the size parameters (α , FF) over land are less reliable compared
212 to the corresponding ones over sea, since they are highly sensitive to spectral dependent factors such as
213 errors in the surface model or sensor calibration changes. Over sea, the accuracy of size parameters is
214 strongly dependent on wind conditions.

215 Similar data have been used by Gkikas et al. (2013), however, in the present study we have
216 improved data quality by using the quality assurance-weighted (QA) level 3 data ([http://modis-
217 atmos.gsfc.nasa.gov/docs/QA_Plan_2007_04_12.pdf](http://modis-atmos.gsfc.nasa.gov/docs/QA_Plan_2007_04_12.pdf)) derived from the level 2 retrievals (10 km x 10
218 km spatial resolution). Each level 2 retrieval, is flagged with a bit value (from 0 to 3) corresponding to
219 confidence levels (No confidence: 0, Marginal: 1, Good: 2 and Very Good: 3). Based on this, the level
220 3 QA-weighted spatial means are obtained by the corresponding level 2 retrievals considering as
221 weight their confidence level (bit value). In addition, the day cloud fraction as well as the number of

222 level 2 counts, which are both relevant to the performance of the satellite algorithm, are also used in
223 this study. The time series of daily MODIS aerosol data cover the 13-yr period March 2000-February
224 2013 (Terra) and the 10-yr period January 2003-December 2012 (Aqua).

225 2.1.2 EP/TOMS and OMI-Aura

226 The selected retrievals from MODIS provide information about particles' load (*AOD*) and size (α ,
227 FF , r_{eff}), which are both necessary to identify dust episodes. However, since dust is not the only coarse
228 aerosol, for example sea-salt can be so as well, another optical property indicative of particle
229 absorption efficiency is also required by the algorithm. To address this issue, the Absorption Aerosol
230 Index (*AI*) daily data were also used, derived from measurements taken by the Total Ozone Mapping
231 Spectrometer (TOMS) instrument onboard the NASA's Earth-Probe satellite (2000-2004) and the
232 Ozone Monitoring Instrument (OMI) onboard the NASA's Aura satellite (2005-2013). *AI* is the
233 primary TOMS aerosol product (Herman et al., 1997) based on a spectral contrast method in a *UV*
234 region (331-360 nm) where ozone absorption is very small and can be used for the distinction between
235 scattering (e.g. sea-salt) and absorbing (e.g. desert dust, smoke) aerosols. The retrieval algorithm (fully
236 described by Torres et al., 1998; 2002; 2005) takes advantage of the low surface albedo in the *UV*
237 spectrum range, even in arid and semi-arid areas, making thus possible the estimation of the *AOD* over
238 highly reflecting desert surfaces, where the major dust sources are located. Since the late 70's, the
239 TOMS sensor onboard Nimbus-7 (1978 – 1993) and Earth Probe (1996 – 2005) has been providing
240 global aerosol measurements. With the deployment of the EOS-Aura OMI (Ozone Monitoring
241 Instrument) in mid-2004 (Torres et al., 2007) the near *UV* aerosol record continues to be extended into
242 the foreseeable future. OMI is a hyperspectral sensor, covering the 270-500 nm range, launched
243 onboard the EOS-Aura satellite on July 15, 2004 (1:38 pm equator crossing time, ascending mode)
244 providing almost daily global coverage thanks to its wide viewing swath (2600 km with 13 km x 24 km
245 nadir resolution). Apart from *AI* measurements, OMI aerosol products include also the total and
246 absorption *AOD* and the single scattering albedo at 388 and 500 nm (Torres et al., 2007). Both EP-
247 TOMS and OMI-Aura retrievals are available via the Mirador ftp server (<http://mirador.gsfc.nasa.gov/>)
248 of the Goddard Earth Sciences Data and Information Services Center (GES DISC). OMI-Aura data, as
249 MODIS, are provided at 1° x 1° spatial resolution while the EP-TOMS retrievals have been regridded
250 from their raw spatial resolution (1° x 1.25°) in order to match with the other two datasets (OMI,
251 MODIS).

252

253 2.1.3 CALIOP-CALIPSO

254

255 The Cloud-Aerosol Lidar with Orthogonal Polarization (CALIOP) onboard the NASA's satellite
256 CALIPSO (Cloud-Aerosol Lidar and Infrared Pathfinder Satellite Observations), launched in April
257 2006, provides vertical resolved aerosol and cloud observations (Winker et al., 2009) since June 2006.
258 CALIPSO is flying in the A-Train constellation (Stephens et al., 2002; <http://atrain.nasa.gov/>) in a sun-
259 synchronous polar orbit at 705 km over the surface, with a 16-day repeat cycle, crossing the equatorial
260 plane at about 13:30 local solar time (Winker et al., 2009). CALIOP is an active sensor measuring the
261 backscatter signal at 532 nm and 1064 nm as well as the polarization at 532 nm (Winker et al., 2009).
262 These level 1 retrievals are further processed (calibration and range corrections) passing to Level 2 in
263 order to retrieve the backscatter and extinction coefficients, at 532 nm and 1064 nm, for aerosol and
264 cloud layers. The identification of cloud and aerosol layers within the atmosphere (Vaughan et al.,
265 2009) is made through the cloud aerosol discrimination (*CAD*) algorithm (Liu et al., 2009), which is
266 based on the probability distribution functions (*PDFs*) of altitude-and-latitude-dependent parameters
267 (integrated color ratio, layer-integrated volume depolarization ratio, mean attenuated backscatter
268 coefficient). *CAD* scores vary mainly from -100 to 100 indicating the presence of aerosols and clouds
269 when are negative and positive, respectively, while bins of confidence levels, both for aerosols and
270 clouds, are defined based on their absolute values
271 (https://eosweb.larc.nasa.gov/sites/default/files/project/calipso/quality_summaries/CALIOP_L2VFMPr
272 [oducts_3.01.pdf](https://eosweb.larc.nasa.gov/sites/default/files/project/calipso/quality_summaries/CALIOP_L2VFMPr)). More specifically, the performance of the classification scheme in the *VFM*
273 algorithm, either for aerosols or clouds, is more reliable for increasing *CAD* scores in absolute terms.
274 Aerosols are categorized in 6 primary types namely: (i) clean marine, (ii) dust, (iii) polluted
275 continental, (iv) clean continental, (v) polluted dust and (vi) smoke (Omar et al., 2009).

276 In the present analysis, we use the Version 3 (3.01 and 3.02) of the Level 2 Vertical Feature Mask
277 (*VFM*) and Aerosol Profile Products (*APro*) files, available from June 2006 to February 2013, both
278 derived from the NASA's Earth Observing System Data and Information System
279 (<http://reverb.echo.nasa.gov/>). The aerosol profile products are generated at a uniform horizontal
280 resolution of 5 km (http://www-calipso.larc.nasa.gov/products/CALIPSO_DPC_Rev3x6.pdf), while the
281 vertical resolution varies from 60 to 180 m depending on the altitude range and the parameter. The
282 scientific data sets which have been analyzed are the following: (i) aerosol subtype, (ii) *CAD* score and

283 (iii) Total Backscatter Coefficient at 532 nm (β_{532nm}), reported at several tropospheric and stratospheric
284 levels above mean sea level (Hunt et al., 2009).

285

286 2.2 Surface-based data

287

288 2.2.1 AERONET

289 The AErosol RObotic NETwork (AERONET, Holben et al., 1998) is a worldwide network of
290 installed CIMEL sun-sky radiometers obtaining sun-photometric observations in more than 1000
291 locations of the planet (<http://aeronet.gsfc.nasa.gov>). The solar irradiances received by the photometer
292 are inverted to columnar aerosol optical and microphysical properties through the implementation of
293 retrieval algorithms (e.g. Dubovik and King, 2000; O' Neill et al., 2003). The followed standardized
294 methods concerning instrument maintenance, calibration, cloud screening and data processing allow
295 aerosol monitoring and comparison between different study periods and areas (Smirnov et al., 2000).
296 From the global AERONET stations, 109 are located within the geographical limits of our study
297 region. For each station, the daily averages of cloud-screened and quality assured data (Level 2.0) of
298 direct sun and almucantar retrievals are used for: (i) *AOD* at 7 wavelengths from 340 to 1020 nm, (ii)
299 size distribution retrieved for 22 logarithmically equidistant discrete points (r_i) in the range of sizes
300 $0.05 \mu\text{m} \leq r \leq 15 \mu\text{m}$, (iii) Ångström exponent between 440 and 870 nm ($\alpha_{440-870nm}$), (iv) total effective
301 radius (r_{eff}), and (v) single scattering albedo (*SSA*) and asymmetry parameter (g_{aer}) both retrieved at 440
302 nm, 675 nm, 870 nm and 1020 nm. The uncertainty in the estimation of *AOD* depends on technical
303 (e.g. calibration method) factors and inversion assumptions, both described in detail in Holben et al.
304 (1998). Moreover, the accuracy of the retrieved *AOD* by the CIMEL radiometer is spectrally
305 dependent, being higher ($< \pm 0.01$) for wavelengths longer than 440 nm and lower ($< \pm 0.02$) for the *UV*
306 wavelengths (Eck et al., 1999). It should be also noted that the AERONET Level 2.0 inversion products
307 (e.g. *SSA*) are provided when *AOD* at 440 nm is higher than 0.4 ensuring the minimization of the
308 inversion uncertainties, which are also determined by other factors (e.g. scattering angle, particles'
309 sphericity) as stated in detail by Dubovik et al. (2000).

310

311 2.2.2 PM_{10}

312 Daily total and dust surface PM_{10} concentrations, over the period 2001-2011 from 22 regional
313 background and suburban background sites were used in this study. The monitoring sites are distributed

314 as follows: 10 in Spain; 2 in southern France; 5 in Italy; 3 in Greece; 1 in southern Bulgaria and 1 in
315 Cyprus. PM_{10} concentrations were obtained in most cases from gravimetric determinations on filters,
316 whereas in few cases they were determined by real time instruments (Querol et al., 2009b; Pey et al.,
317 2013) but corrected against gravimetric measurements carried out in annual field campaigns. The
318 disaggregation of the dust component to the total amount is made based on a statistical approach which
319 has been applied in several past studies (e.g. Rodríguez et al., 2001; Escudero et al., 2007; Querol et al.,
320 2009b; Pey et al., 2013). A full description of the methodology which is followed for the calculation of
321 dust particles' contribution to the total PM_{10} is presented in Escudero et al. (2007). Briefly, the net dust
322 PM_{10} amount is calculated through the subtraction of the regional background PM_{10} , which is obtained
323 by applying a monthly moving 30th percentile to the PM_{10} timeseries excluding days of dust transport,
324 from the corresponding values of the total PM_{10} concentrations. Most of the derived data were obtained
325 from the AirBase (<http://acm.eionet.europa.eu/databases/airbase/>) database, while for the stations
326 Finokalia (Crete) and Montseny (NE Spain) the relevant measurements have been acquired from the
327 EUSAAR (<http://www.eusaar.net/>) database.

328

329 **3. Identification of desert dust episodes**

330

331 Following the methodology proposed by Gkikas et al. (2013), desert dust (*DD*) episodes are
332 identified based on an objective and dynamic algorithm which consists a branch of a unified algorithm
333 (Gkikas et al., 2016) able to identify and characterize not only *DD* episodes, but also four other types of
334 aerosol episodes, namely biomass-urban (*BU*), dust/sea-salt (*DSS*), mixed (*MX*) and undetermined
335 (*UN*). The algorithm (see Figure 2 in Gkikas et al., 2013) operates in three steps and is applied in each
336 individual 1° x 1° geographical cell within the geographical limits of the study domain (29° N - 47° N
337 and 11° W - 39° E). First, the mean (*Mean*) and the associated standard deviation (*Std*) from the
338 available AOD_{550nm} retrievals are calculated for the whole study period. These primary statistics are
339 used for the definition of two threshold levels, which are equal to $Mean+2*Std$ and $Mean+4*Std$. The
340 geographical distributions of the computed statistics (*Mean* and *Std*) as well as the corresponding
341 spatial patterns of both threshold levels are displayed in Figures S1-a (MODIS-Terra, Mar. 2000 – Feb.
342 2013) and S1-b (MODIS-Aqua, 2003 – 2012) in the supplementary material. At the next step, the
343 algorithm analyzes the daily AOD_{550nm} timeseries and classifies an episode as a strong one when *AOD*
344 is between the two defined thresholds ($Mean+2*Std \leq AOD_{550nm} < Mean+4*Std$) and as an extreme
345 one when *AOD* is higher/equal than $Mean+4*Std$. The same approach was undertaken by Gkikas et al.

346 (2009) who classified the Mediterranean aerosol episodes over the period 2000-2007 according to their
347 strength and described their frequency and intensity. It must be clarified that according to our
348 methodology in areas frequently affected by dust episodes, both mean and standard deviation values
349 are expected to be high resulting to high thresholds which means that cases with moderate-to-high
350 *AODs*, also possibly relevant to radiative and health effects, are masked out from the dataset. In order
351 to investigate the possible impact of this, “unbiased” mean, standard deviation and thresholds of *AOD*
352 are also computed based on another methodology and the results are discussed comparatively to those
353 of the primary methodology in a separate paragraph. Moreover, it must be mentioned that the satellite
354 algorithm identifies only intense desert dust episodes since their *AOD* must be higher than
355 $Mean+2*Std$ which is considered as a high threshold level.

356 It should be noted that the representativeness of the calculated mean levels is possibly affected by
357 the availability of the *AOD* retrievals and particularly by the way these data are distributed both at
358 temporal and spatial scales. Thus, a possible underrepresentation of winter *AOD* data in the long-term
359 dataset, which is often the case in satellite retrievals of *AOD*, may result in a smaller mean *AOD* than
360 what would be in case of complete and balanced seasonal availability. Moreover, the spatiotemporal
361 availability of *AOD* is determined by the different satellite retrieval algorithm assumptions depending
362 on the underlying surface type (land or sea) and clouds (i.e. satellite retrievals are possible only under
363 clear skies conditions). In order to investigate the possible effect of temporal availability of daily *AOD*
364 data, we have calculated the percentage availability of *AOD* retrievals on a monthly, seasonal and year
365 by year basis, over the period 2000-2013 (results not shown here). Seasonal differences of *AOD*
366 availability are mainly encountered in the northernmost parts of the study region, attributed to the
367 enhanced cloud coverage, with lower values (20 to 40 %) from December to February against 50-85%
368 for the rest of the year. Differences of *AOD* availability are also found between land and sea surfaces
369 which are more pronounced in winter and summer and less remarkable during the transition seasons.
370 More specifically, across the Mediterranean Sea, in winter, the availability percentages range from 70
371 to 90 % while in summer the corresponding values are decreased, due to Sun glint, down to 60 % and
372 80 %, respectively. Over land, for both seasons, the spatial patterns of *AOD* availability are reversed. In
373 order to investigate furthermore how the spatiotemporal *AOD* variability and unbalanced seasonal
374 distribution of MODIS *AOD* data can affect the calculated mean *AOD* levels (calculated by daily
375 retrievals) we have repeated the calculations by utilizing monthly retrievals (calculated by the daily
376 ones) thus removing the unequal seasonal contribution to the long-term mean *AOD* values. According
377 to our results, only small differences are found, generally hardly exceeding 0.1 in absolute and 5% in

378 relative percentage terms, with the mean *AODs* over land being higher by up 10 % when they are
379 computed from daily than monthly data, while the opposite is found over sea. This finding reveals that
380 the unequal temporal distribution of *AOD* retrievals does not have critical impact on the computed
381 mean *AODs* and the resulting algorithm outputs presented in this study.

382 In a further step of the methodology, the strong and extreme *DD* episodes are identified separately
383 over land and sea surfaces of the study region. This is achieved through the usage of specific aerosol
384 optical properties, namely the Ångström exponent, effective radius, fine fraction and aerosol index,
385 which provide information about particles' size and nature. For each optical property, appropriate
386 upper or lower thresholds have been set up which must be valid concurrently in order to certify the
387 presence of dust particles in the atmosphere. Note that there are not any unanimously defined
388 acknowledged thresholds in literature. Therefore, these cut-off levels have been selected here according
389 to the literature findings, availability of raw data and several own sensitivity tests (more details are
390 provided in Gkikas et al., 2013) which have been applied individually to the MODIS size parameters
391 (i.e., α , *FF* and r_{eff}). Such analysis is essential when multi-parameter datasets are utilized and their
392 variations can possibly modify the satellite algorithm's outputs. To this aim, we have applied the
393 satellite algorithm modifying by 0.1 the α , *FF* and r_{eff} values within the ranges 0.6 – 0.8, 0.1 – 0.4 and
394 0.4 – 0.8, respectively. Our results indicate that the geographical patterns remain similar and the total
395 number of *DD* episodes is only slightly modified (less than 4 %) for the α and r_{eff} retrievals, whereas it
396 changes more for the *FF* retrievals (by up to 25% over sea for strong episodes). Here, the validity of
397 these thresholds is further evaluated against AERONET measurements and the corresponding results
398 are discussed in Section 4.1.1.4.

399 In order to address the issue of possible overestimation of the defined threshold levels, particularly
400 in the most dust affected areas as it has been mentioned above, we have also applied the satellite
401 algorithm using an alternative methodology (METHOD-B) in which dust-affected grid cells were
402 excluded. In this case, from the raw *AOD* retrievals we have masked out the “pure” desert dust grid
403 cells, which were identified based on the concurrent fulfillment of the defined criteria for dust
404 occurrence in the algorithm (for Ångström exponent, fine fraction, aerosol index and effective radius).
405 Then, from the remaining data (non-dust *AOD* retrievals), the mean, the associated standard deviation
406 as well as the defined thresholds of *AOD* are computed for the whole study period, for each pixel, as
407 also done in the primary methodology. Finally, also similarly to the way done in the primary
408 methodology, the *DD* episodes were classified into strong and extreme ones. The obtained results, i.e.

409 frequency of occurrence and intensity of *DD* episodes, based on the primary methodology and
410 METHOD-B are discussed in Section 4.2.

411 As explained, a similar methodology and data were used in the study by Gkikas et al. (2013).
412 Nevertheless, the present one is a significant extension mainly for five reasons: (i) *DD* episodes are
413 identified here over an extended period of study and for both MODIS platforms, i.e. Mar. 2000 – Feb.
414 2013 for MODIS-Terra and 2003 – 2012 for MODIS-Aqua, (ii) a second methodology (METHOD-B)
415 for the identification of *DD* episodes is tested, (iii) the quality of the input data is improved by using
416 QA-weighted level-3 data produced by weighting level-2 data based on their confidence flag instead of
417 regular ones ($QA \geq 1$), (iv) emphasis is given to the vertical structure of the intense *DD* episodes and (v)
418 the role of the detailed dust outbreaks' vertical structure for the level of agreement between columnar
419 MODIS *AOD* and ground PM_{10} concentrations is investigated. In addition, in the present analysis, the
420 satellite algorithm operates also using only *AODs* associated with cloud fractions (*CF*) lower/equal
421 than 0.8, in order to investigate possible modifications of our results due to the cloud contamination
422 effects on MODIS *AODs*. The critical value of 0.8 for *CF* has been defined according to Zhang et al.
423 (2005) and Remer et al. (2008), who stated that under extended cloud coverage conditions *AOD* levels
424 can be increased substantially.

425

426 **4. Results**

427 Before dealing with the horizontal patterns (sub-section 4.2) and the vertical structure of dust
428 outbreaks (sub-sections 4.3 and 4.4), it is very important to compare the algorithm's outputs against
429 quality AERONET and PM_{10} observations (sub-section 4.1) in order to ensure an accurate three-
430 dimensional view of the intense Mediterranean *DD* episodes. It must be clarified, that the comparison
431 of the satellite algorithm's outputs versus AERONET/ PM_{10} is made only for its default version and not
432 for the METHOD-B, since between the two methodologies are not found remarkable differences, as it
433 will be presented in Section 4.2. For the same reason, the synergistic implementation of the CALIOP-
434 CALIPSO lidar profiles is done only when the *DD* episodes are identified based on the primary
435 methodology. The present section has been organized accordingly and the results are given below.

436 4.1 Comparison of the satellite algorithm's outputs against AERONET and PM_{10} measurements

437 The ability of the satellite algorithm to identify satisfactorily *DD* episodes, is tested against ground
438 measurements from 109 AERONET (Fig. 1, orange squares) and 22 PM_{10} (Fig. 1, green triangles)
439 stations located in the broader Mediterranean area. This is an extended and thorough comparison which

440 exceeds largely a similar one done for the outputs of the previous version of satellite algorithm (2000-
441 2007, Gkikas et al., 2013), but only relying on 9 AERONET stations and using *AOD* and volume size
442 distribution data. Here, the comparison is repeated for the improved algorithm, being extended over a
443 longer time period, for a much larger number of AERONET stations, and an analysis of more optical
444 properties, namely the Ångström exponent, effective radius, single scattering albedo and asymmetry
445 parameter is made. The comparison is performed for both study periods and satellite platforms (Mar.
446 2000 – Feb. 2013 for Terra and 2003 – 2012 for Aqua) while the issue of possible cloud contamination
447 is also considered. However, since the obtained results revealed a very similar performance of the
448 algorithm for both periods and platforms, only the results for the period Mar. 2000 – Feb. 2013 are
449 given here.

450 In 46 out of 109 AERONET stations, depicted with yellow triangles in Figure 1, we have found at
451 least one strong or extreme dust episode, for which coincident satellite and ground measurements are
452 available. For the specific AERONET stations and episode days, the mean values of the selected
453 AERONET aerosol optical properties have been calculated separately for strong, extreme and all (both
454 strong and extreme) *DD* episodes identified by the satellite algorithm. Subsequently, these values were
455 compared to the corresponding ones calculated from all the available retrievals (climatological
456 conditions, *clim*) collected from the 109 Mediterranean AERONET stations, during the period Mar.
457 2000 – Feb. 2013, aiming at highlighting the effect of episodes on these optical properties.
458 Additionally, in 7 AERONET stations (cyan circles in Figure 1) the intense *DD* episodes have been
459 identified from ground (AERONET) and the corresponding results are compared with the satellite
460 algorithm outputs (Section 4.1.1.4). Finally, the performance of the algorithm is also tested against
461 surface PM_{10} measurements from 22 stations (Section 4.1.2).

462

463 4.1.1 AERONET

464 4.1.1.1 Aerosol optical depth

465 During the period Mar. 2000 – Feb. 2013, 346 pixel level intense *DD* episodes have been identified
466 by the satellite-based algorithm, in which coincident MODIS-Terra and AERONET retrievals are
467 available. The selected dataset corresponds to 1.06 % of the overall (strong and extreme) *DD* episodes
468 (32635) which have been identified during the study period. It should be noted that AERONET
469 AOD_{550nm} values have been calculated from available AERONET AOD_{870nm} and Ångström exponent

470 data ($\alpha_{440-870nm}$) by applying the Ångström equation (Ångström, 1929) to match the MODIS AOD_{550nm} .
471 For these intense *DD* episodes, the comparison between the satellite and ground aerosol optical depths
472 at 550 nm is given in Figure 2. Two similar scatterplots with matched MODIS-AERONET data pairs
473 are given. The first one (Fig. 2 i-a) is resolved by the number of level 2 (*L2*) measurements of 10 km x
474 10 km spatial resolution from which the compared $1^\circ \times 1^\circ$ level 3 (*L3*) *AODs* in the figure are derived.
475 The second scatterplot (Fig. 2 i-b) is resolved by the spatial standard deviation inside the $1^\circ \times 1^\circ$
476 geographical cell (level 3 *AODs*). Both scatterplots address the issue of level 3 *AOD* sub-grid spatial
477 variability, which is essential when attempting comparisons against local surface-based *AOD* data like
478 the AERONET.

479 The overall correlation coefficient (*R*) between MODIS and AERONET *AODs* is equal to 0.505,
480 with the satellite *AODs* being overestimated (bias=0.143). From the overall scatterplots, it is evident
481 the existence of outliers associated with small number of level 2 retrievals (< 20, blue color Fig. 2 i-a)
482 and/or high standard deviations (> 0.5, yellowish-reddish points, Fig. 2 i-b) inside the *L3* grid cell. This
483 finding underlines the role of homogeneity and representativeness of *L3* retrievals for the comparison
484 of MODIS *AODs* against AERONET. This role is better visualized in Fig. 2 ii-a, where are presented
485 the computed *R* values between MODIS level-3 and AERONET *AODs* depending on the number of *L2*
486 retrievals from which the *L3* products were derived. In general, it is known that the *L2* pixel counts
487 range from 0 to 121 while in polar regions (typically around 82° latitude) the maximum count numbers
488 can be even higher due to overlapping orbits and near nadir views intersect (Hubanks et al., 2008). It is
489 clear from our results that the correlation coefficients are gradually and essentially improved, from 0.49
490 to 0.75, with increasing representativeness of MODIS *AODs*, i.e. increasing counts of *L2* retrievals
491 attributed. A similar improvement has been reported by Amiridis et al. (2013) who found a better
492 agreement between MODIS/AERONET and CALIOP aerosol optical depths applying similar spatial
493 criteria. The agreement between MODIS and AERONET also improves when the former *AOD*
494 products are more spatially homogeneous, i.e. when they are characterized by smaller *AOD* standard
495 deviations at the grid-level (from < 0.25 down to < 0.05, Fig. 2 ii-b). However, our results also indicate
496 that apart from increasing correlation coefficients (up to 0.7-0.8) with increasing level-2 counts and
497 decreasing standard deviations, the number of intense *DD* episodes is decreased dramatically (about
498 40-50 for more than 50 counts and standard deviation smaller than 0.05).

499 In order to assess the performance of the satellite algorithm when operates with non- (Gkikas et al.,
500 2013) and weighted QA (present analysis) MODIS-Terra retrievals we have compared its outputs (*DD*
501 episodes' *AODs*) of both versions versus the corresponding AERONET *AODs* for the period Mar. 2000

502 – Feb. 2007 (Gkikas et al., 2013). Based on our results, the computed correlation coefficients are equal
503 to 0.53 (135 *DD* episodes) and 0.59 (177 *DD* episodes) for the old and new version of the satellite
504 algorithm, respectively, revealing thus a better performance when QA-weighted level 3 retrievals are
505 utilized as inputs to the satellite algorithm.

506 Finally, the spectral variation of the AERONET *AODs* at 7 wavelengths, from 340 to 1020 nm, in
507 climatological and dust episodes conditions has been investigated (results given in Figure S2,
508 supplementary material). The *AOD* boxplots produced for all the available daily AERONET
509 measurements (orange) and for the corresponding retrievals during strong (cyan), extreme (red) and all
510 *DD* (green) episodes identified by the satellite algorithm show that the spectral variation of aerosol
511 optical depth decreases in cases of dust episodes, with respect to the “climatological” conditions. This
512 is mainly attributed to the further increasing *AOD* levels at wavelengths longer than 500 nm (by about
513 6 times) than in (or near) the visible.

514

515 4.1.1.2 Aerosol volume size distribution

516 In Figure 3, are presented the mean aerosol volume size distributions (*AVSDs*) calculated from all
517 available AERONET data (orange curve) as well as under strong (cyan curve), extreme (red curve) and
518 all (green curve) *DD* episodes conditions. The results are given for Mar. 2000 – Feb. 2013 using
519 MODIS-Terra (346 intense *DD* episodes) retrievals as inputs to the satellite algorithm. In the
520 climatological curve, two modes are distinct centered at 0.15 μm for the fine mode and 2.24 μm for the
521 coarse mode. There is an about equal contribution of both modes, indicating the coexistence of fine
522 (e.g. urban aerosols) and coarse (e.g. dust aerosols) particles over the broader Mediterranean area. This
523 result is in agreement with previous studies for the Mediterranean (e.g. Fotiadi et al., 2006; Mallet et
524 al., 2013). However, under dust episodes conditions, although the *AVSD* still has two modes, there is a
525 dramatic increase of the coarse mode, which strongly dominates. More specifically, the peak of the
526 coarse mode (radius between 1.7 and 2.24 μm) is increased by factors of about 10, 15 and 11 for the
527 strong, extreme and all *DD* episodes. The differences between the strong and extreme *AVSDs* are
528 statistically significant (confidence level at 95 %) for almost all size bins (18 out of 22) except bin 1
529 (0.050 μm), 2 (0.065 μm), 6 (0.194 μm) and 7 (0.255 μm). Moreover, it should be noted that the
530 increment factors are slightly decreased when the algorithm operates only with *AODs* associated with
531 cloud fractions less than 0.8 which is reasonable since possible “overestimated” retrievals are masked
532 out from the analysis. Similar modifications in the shape of *AVSD* during dust outbreaks have been

533 pointed out by several studies in the past, either for the Mediterranean region (e.g. Kubilay et al., 2003;
534 Lyamani et al., 2005; Córdoba-Jabonero et al., 2011) or for other dust affected areas of the planet (e.g.
535 Alam et al., 2014; Cao et al., 2014).

536

537 *4.1.1.3 Size optical properties, single scattering albedo and asymmetry parameter*

538 The accuracy of the *DD* episodes identification method was further assessed by also using other
539 AERONET aerosol optical properties than *AOD*, namely the Ångström exponent (α) and the effective
540 radius (r_{eff}), able to provide information about particles' size. For both aerosol optical properties, the
541 boxplots for all the available AERONET retrievals as well as for the corresponding data during strong,
542 extreme and all *DD* episodes, have been produced and depicted in Figure S3 (supplementary material).

543 Based on our results, the appropriateness of the applied methodology is confirmed by the drastic
544 reduction of α and increase of r_{eff} values when dust outbreaks occur. When all available AERONET
545 retrievals are considered (*clim*), the majority (> 75%) of α values is higher than 1.04 indicating the
546 strong presence of fine particles in the study domain (Figure S3-i). On the contrary, during intense dust
547 episodes the majority of the corresponding values for all and strong *DD* episodes are lower than 0.54
548 while for the extreme ones are lower than 0.36. Such low Ångström exponent values, attributed to
549 transported mineral particles from the northern African deserts (Pace et al., 2006), have been reported
550 also in previous studies (e.g. Tafuro et al. 2006; Basart et al., 2009). The existence of coarse aerosols is
551 also confirmed by the increase of r_{eff} values under intense *DD* conditions compared to the
552 climatological levels (Figure S3-ii). For all *DD* episodes, the 75% of r_{eff} values is higher than 0.55 μm
553 reaching up to 1.4 μm , while the mean and the median values are equal to about 0.73, compared to
554 about 0.37 for the climatological conditions. These values are even higher when extreme *DD* episodes
555 are concerned.

556 Moreover, the spectral variations of the averaged AERONET single scattering albedo (*SSA*) and the
557 asymmetry parameter (g_{aer}) are also studied. During intense dust outbreaks the shape and magnitude of
558 spectral *SSA* (Figure S4-i) and g_{aer} (Figure S4-ii) are modified compared to the climatological
559 conditions. The spectral curves of both parameters become less and more flattened during dust episodes
560 for *SSA* and g_{aer} , respectively. For *SSA*, the steepening results from decreasing values in the visible and
561 increasing values in the near-infrared (by up to 0.04, reaching 0.97 at 1020 nm). The flattening for g_{aer}
562 arises from smaller and larger increments in visible and near-infrared values, by up to 0.04 and 0.09,

563 respectively. The differences between strong and extreme *DD* episodes *SSA* spectral curves are
564 statistically significant at 95 % confidence level only at 870 and 1020 nm. On the contrary, the
565 corresponding differences for the g_{aer} are statistically significant in all wavelengths. Our results are in
566 agreement with those presented for *SSA* by Mallet et al. (2013) in the Mediterranean and for g_{aer} by
567 Alados-Arboledas et al. (2008) during a dust episode over the southeastern parts of Spain.

568

569 *4.1.1.4 Intercomparison of surface-based and satellite algorithms used for the identification of the* 570 *desert dust episodes*

571 Despite their great usefulness, satellite aerosol retrievals still suffer from uncertainties, and
572 generally are considered as inferior to surface-based similar products, which are taken as the reference.
573 In order to examine this degree of uncertainty and to verify the successful performance of the
574 algorithm, we also tested using it along with AERONET retrievals. This has been made for 7
575 Mediterranean AERONET stations, depicted with cyan circles in Figure 1, during the periods for which
576 ground retrievals are available (Table 1). The selection of the AERONET stations was based on: (i)
577 data availability (see last column of Table 1), (ii) their location (i.e. near to the Northern African and
578 Middle East deserts) and (iii) the inclusion of sites where the aerosols' regime is complex (e.g. El
579 Arenosillo, FORTH Crete). The intense *DD* episodes were identified following the methodology
580 described in section 3, but using only *AOD* at 870 nm, $\alpha_{440-870nm}$ (lower/equal than 0.7) and r_{eff} (higher
581 than 0.6) as criteria, based upon their availability from AERONET. Subsequently, the algorithm was
582 also operated again using satellite (MODIS-Terra, OMI-Aura, EP-TOMS) input data for the days with
583 available retrievals in each of the 7 AERONET stations.

584 In Figure 4, we present the overall scatterplots between satellite and ground *AODs* when intense
585 *DD* episodes have been identified based on the ground (left column) and the satellite (right column)
586 algorithm. Colors in Figs. 4 i-a, 4 ii-a, 4 iii-a represent the associated MODIS-Terra Ångström
587 exponent, effective radius and day cloud fraction retrievals, respectively. In Figs. 4 i-b and 4 ii-b colors
588 represent the AERONET Ångström exponent and effective radius, respectively, while in Figure 4 iii-b
589 represent the day cloud fraction observations derived by MODIS-Terra. Through this approach it is
590 feasible to assess furthermore the performance of the satellite algorithm, specify its drawbacks and
591 check the validity of the defined thresholds (green boxes in Figure 2 in Gkikas et al., (2013)).

592 It is apparent that the agreement between MODIS-Terra and AERONET *AODs* is better when *DD*
593 episodes are identified from the ground, as shown by the increased correlation coefficients (from 0.521
594 to 0.704), increased slopes (from 0.6 to 0.9-1.0) and decreased biases (from 0.16 to -0.03). In
595 particular, when *DD* episodes are identified from space, the MODIS-Terra *AOD* retrievals are
596 overestimated (bias=0.163) with regards to AERONET, particularly at low *AOD* values (< 0.5). In both
597 algorithms, the highest overestimations are associated with cloud fractions higher than 0.7 due to the
598 possible contamination of the satellite *AODs* by clouds (Figure 4 iii-a, iii-b). Given that *DD* episodes'
599 identification based on AERONET retrievals is more efficient, we have used these results in order to
600 check the validity of the defined thresholds for α , *AI*, *FF* and r_{eff} used in the satellite algorithm. For
601 each aerosol optical property, it has been calculated the percentage of intense *DD* episodes for which
602 the corresponding satellite observations are below or above the defined thresholds, depending on the
603 parameter. The results given in Table 2 are satisfactory, since the percentages range from 87 to 99%,
604 and confirm the validity of the defined thresholds.

605 The scatterplots in Figs. 4 i-b and ii-b also reveal some weaknesses of the satellite-based algorithm.
606 More specifically, it is found that for few *DD* episodes identified by the satellite algorithm the
607 corresponding AERONET Ångström exponent and effective radius values are higher than 1 and
608 smaller than 0.4, respectively. These values indicate a predominance of fine particles instead of coarse
609 ones as it would be expected for desert dust aerosols. In order to quantify the number of misclassified
610 pixel level intense *DD* episodes by the satellite algorithm, we have computed the percentage of cases
611 for which the AERONET α values are higher than 1 (15%) and r_{eff} values are lower than 0.4 (17.7%).
612 Also, we have repeated these calculations for all *DD* episodes and the corresponding percentages were
613 found to be equal to 11.8% and 14.5%, respectively. These misclassifications of the satellite algorithm
614 occur in AERONET stations (e.g. Thessaloniki, Rome, Avignon) with a strong presence of
615 anthropogenic aerosols (Kazadzis et al., 2007; Gobbi et al., 2007; Querol et al., 2009a; Yoon et al.,
616 2012). Some misclassifications also occur in AERONET stations (e.g. Evora, El Arenosillo, FORTH
617 CRETE) with mixed (natural plus anthropogenic) aerosol loads (Fotiadi et al., 2006; Toledano et al.,
618 2007b; Hatzianastassiou et al., 2009; Pereira et al., 2011). Over these areas, there are converging air
619 masses carrying particles of different origin, as shown by performed back-trajectories analyses (results
620 are not shown here) using the HYSPLIT (HYbrid Single-Particle Lagrangian Integrated Trajectory)
621 model (Draxler and Rolph, 2015). Nevertheless, it must be mentioned that *DD* episodes'
622 misclassifications can be also attributed to the lower accuracy of MODIS aerosol size retrievals over
623 land (Section 2.1.1).

624

625 4.1.2 PM_{10} and dust contribution

626 The satellite algorithm's outputs, apart from AERONET retrievals, have been also compared
627 against ground PM_{10} concentrations ($\mu\text{g m}^{-3}$) measured in 22 Mediterranean stations (green triangles in
628 Figure 1).

629 First, for each station, the number of intense *DD* episodes was calculated, for which coincident
630 satellite and ground measurements (total PM_{10}) are available (Figure 5-i). The number of concurrent
631 *DD* episodes varies from 3 to 53, being in general decreasing from southern to northern stations. For 14
632 out of 22 stations, where at least 10 intense *DD* episodes were identified by the satellite-based
633 algorithm, we have computed the correlation coefficients between satellite *AODs* and surface total
634 PM_{10} concentrations (Fig. 5-ii). The highest *R* values (up to 0.8) are recorded in the central and eastern
635 parts of the Mediterranean while the lowest ones are found in the western stations. It must be noted that
636 the correlation coefficients are affected by outliers, because of the limited number of *DD* episodes in
637 each station, highlighting the sensitiveness of the intercomparison. Such outliers can be expected when
638 satellite-based columnar *AODs* and surface-based PM_{10} data are compared, since satellite *AODs* are
639 representative for the whole atmospheric column in contrast to in-situ *PM* measurements which are
640 more representative for the lowest part of the planetary boundary layer affected also by local factors.
641 Therefore, the vertical distribution of desert dust load, as it will be presented in the next sections, can
642 determine the level of agreement between satellite *AODs* and surface *PM* concentrations.

643 The identification method by the satellite algorithm can be considered as correct when dust PM_{10}
644 concentrations are higher than zero (i.e. dust has been recorded at the station). According to this, the
645 ratio between the number of non-zero dust *PM* observations and the number of *DD* episodes
646 (coincident satellite-derived *DD* episodes and total PM_{10} measurements) for each station is defined as
647 success score. The calculated success scores (Figure 5-iii) vary from 68% (Monagrega, northeastern
648 Spain, 28 episodes) to 97% (Boccadifalco, Sicily, 33 episodes) confirming the appropriateness of the
649 *DD* episodes' identification. In the majority of stations, the contribution of dust particles to the total
650 burden (Figure 5-iv) is above 50%, ranging from 44% (Zarra, Spain) to 86.8% (Agia Marina, Cyprus).
651 In order to complete our analysis we have also calculated the mean (Figure 5-v) and the median (Figure
652 5-vi) dust PM_{10} concentrations for the identified intense *DD* episodes in each station. The mean PM_{10}
653 concentrations mainly vary between 20 and 50 $\mu\text{g m}^{-3}$, being higher in the southern stations, as
654 expected. The minimum mean value (17 $\mu\text{g m}^{-3}$) was recorded in Censt (Sardinia) and the maximum

655 one ($223 \mu\text{g m}^{-3}$) in Agia Marina (Cyprus). Our values are much higher than the corresponding ones in
656 Querol et al. (2009b), who obtained that the mean levels of mineral matter in PM_{10} during dusty days
657 range from 8 to $23 \mu\text{g m}^{-3}$ based on ground concentrations derived by 21 Mediterranean stations. These
658 differences are reasonable since here only intense desert dust outbreaks associated with high aerosol
659 optical depths are considered. Finally, the median PM_{10} concentrations are lower compared to the
660 average ones, indicating that outliers (cases with extremely high AOD or PM_{10}) can alter the results,
661 attributed to the fact that both parameters' (AOD and PM_{10}) distributions are not Gaussians. For this
662 reason the highest differences are found in Finokalia (Crete) and Agia Marina (Cyprus), where the
663 maximum daily PM_{10} concentrations, equal to 690 and $1291 \mu\text{g m}^{-3}$, respectively, were recorded during
664 an intense dust outbreak affected the eastern Mediterranean on 24 and 25 February 2006.

665 4.2 2D geographical distributions of desert dust episodes' frequency and intensity

666 The mean geographical distributions of strong and extreme DD episodes' frequency of occurrence
667 (episodes yr^{-1}) are presented in Figure 6. Results are given separately as obtained from MODIS-Terra
668 and Aqua for the periods Mar. 2000 – Feb. 2013 and 2003 – 2012, corresponding to local late morning-
669 to-noon (Terra) and afternoon (Aqua) conditions, respectively. It is evident a gradual reduction of
670 frequencies from south to north, while for the strong DD episodes also appears a west to east
671 decreasing gradient. The decreasing south-to-north gradient of intense DD episodes' frequency, which
672 is also in agreement with previous studies based on ground PM measurements (Querol et al., 2009b;
673 Pey et al., 2013), model simulations (Papayannis et al., 2008; 2014) and AERONET AOD retrievals
674 (Basart et al., 2009), can be attributed to the increasing distance from the major dust sources and to the
675 higher precipitation amounts at the northern parts of the basin (e.g. Marriotti et al., 2002; Mehta and
676 Yang, 2008).

677 The maximum frequencies ($9.9 \text{ episodes yr}^{-1}$) of strong DD episodes are observed in the western
678 parts of the study region, for both periods and datasets, while the corresponding values for the extreme
679 ones ($3.3 \text{ episodes yr}^{-1}$) are observed over the central Mediterranean Sea for MODIS-Terra (Mar. 2000
680 – Feb. 2013). In general, there is similar spatial variability between Terra and Aqua, though slightly
681 lower maximum frequencies are found for Aqua. Although dust episodes occur rarely across the
682 northern parts of the study region (< 1 and $0.5 \text{ episode yr}^{-1}$ for strong and extreme episodes), their
683 occurrence proves that dust particles can be transported far away from their sources, up to the central
684 (e.g. Klein et al., 2010) or even northern (e.g. Bègue et al., 2012) European areas under favorable
685 meteorological conditions. Our calculated frequencies are significantly lower than the corresponding

686 ones obtained in Pey et al. (2013), who studied the African dust intrusions towards the Mediterranean
687 basin, based on ground *PM* concentrations, over the period 2001 – 2011. The observed deviations
688 between the two studies are mainly attributed to the different thresholds definition and hence nature of
689 dust episodes. Here, focus is given on the intense dust outbreaks (intensity equal/higher than *Mean* +
690 $2*Std$) while in Pey et al. (2013) the dust occurrences were identified even at very low concentrations
691 ($> 1 \mu\text{g m}^{-3}$).

692 A noticeable difference between the two study periods and platforms is that relatively high
693 frequencies of extreme *DD* episodes are recorded in more northern latitudes in the Mediterranean Sea,
694 i.e. up to 43° N, according to MODIS-Terra over Mar. 2000 – Feb. 2013, while they are restricted
695 south of 40° N parallel for MODIS-Aqua during 2003 – 2012. In order to investigate this difference in
696 detail we have also applied the satellite algorithm, over the period 2003 – 2012, i.e. that of Aqua, using
697 MODIS-Terra retrievals as inputs. Through this analysis (Figures S5 and S6 in the supplementary
698 material), it is evident that there is a very good agreement between the satellite algorithm's outputs, for
699 the periods Mar. 2000 – Feb. 2013 and 2003 – 2012, revealing a constant dust episodes' regime.
700 Therefore, the discrepancy appeared between MODIS-Terra and MODIS-Aqua spatial distributions, is
701 attributed to the diurnal variation of factors regulating the emission and transport of dust particles from
702 the sources areas. Schepanski et al. (2009), analyzed the variation of the Saharan dust source activation
703 throughout the day, based on MSG-SEVIRI satellite retrievals, reporting that dust mobilization is more
704 intense in the local early morning hours after sunrise. Note, that desert dust episodes over the period
705 Mar. 2000 – Feb. 2013 have been identified based on observations retrieved by the Terra satellite,
706 which flies over the study region around noon in contrast to Aqua which provides aerosol
707 measurements at early afternoon hours.

708 The analysis has been also repeated (results not shown here) considering as inputs to the satellite
709 algorithm only *AODs* associated with cloud fractions lower/equal than 0.8, in order to investigate
710 possible modifications to our results due to the cloud contamination effect. As it concerns the strong
711 *DD* episodes, the geographical distributions are similar with those of Fig. 6, but the maximum
712 frequencies (recorded in Morocco) are higher by up to 2 episodes yr^{-1} and 0.3 episodes yr^{-1} for the
713 MODIS-Terra (Mar. 2000 – Feb. 2013) and MODIS-Aqua (2003-2012) data set, respectively. On the
714 contrary, in the case of extreme *DD* episodes the maximum frequencies decrease to 2.5 episodes yr^{-1}
715 for the period 2003 – 2012 and they shift southwards, namely over the northern coasts of Africa, while
716 over the central parts of the Mediterranean Sea are lower than 1 episode yr^{-1} .

717 The maps of intensities (in terms of AOD_{550nm}) of *DD* episodes (Figure 7), show that for both study
718 periods and satellite platforms, the maximum intensities are over the Gulf of Sidra and the Libyan Sea,
719 along the northern African coasts. These intensities reach *AODs* up to about 1.5 for strong and 4.1 for
720 extreme episodes, while the minimum ones (values down to 0.25-0.46) are recorded in the northern and
721 western Mediterranean parts. Note that dissimilar spatial patterns appear between the geographical
722 distributions of *DD* episodes' frequency and intensity, indicating that these two features are determined
723 by different factors (e.g. tracks or strength of depressions). Finally, when the cloud contamination is
724 minimized using only *AODs* associated with *CF* lower than 0.8, then the maximum intensities are
725 shifted southwards, across the northern Africa and eastern coasts of the Mediterranean, being lower
726 than 1 and 2 for strong and extreme *DD* episodes, respectively. Through the rejection of possibly
727 overestimated *AODs* from the dataset, it is found that the threshold levels are decreased (mainly over
728 the most frequently dust affected areas) since both mean and standard deviation values are lower
729 (results not shown here). Nevertheless, even though these *AODs* can be overestimated, in the majority
730 of the cases the collocated AERONET *AODs* are high (but lower than the satellite observations)
731 indicating the occurrence of desert dust outbreaks as it has been shown in Section 4.1.1.4.

732 The analysis has been also repeated applying the alternative METHOD-B described in Section 3.
733 Just to ensure a longer temporal coverage, this analysis was done for the period Mar. 2000 - Feb. 2013
734 using MODIS-Terra data. The obtained results for the frequency of occurrence as well as for the
735 intensity of *DD* episodes are depicted in Figures S7 and S8, respectively, in the supplementary
736 material. The geographical patterns for the frequency of occurrence between the two methodologies are
737 similar; however, the maximum values for the strong and extreme *DD* episodes can reach up to 13.3
738 episodes year⁻¹ (Fig. S7-i) and 8.1 episodes year⁻¹ (Fig. S7-ii), respectively. As it concerns the intensity,
739 the geographical patterns, particularly for the strong *DD* episodes, are dissimilar and less distinct
740 compared to the corresponding ones obtained with the primary methodology. This difference is
741 attributed to the inclusion of more dust episodes with variable intensity, which leads to a not so clear
742 "signal" when all these episodes are averaged. Based on METHOD-B, the maximum intensities (in
743 terms of AOD_{550nm}) of strong *DD* episodes can reach up to 1 (Fig. S8-i) while for the extreme episodes
744 (Fig. S8-ii) it can be as large as 3. The main finding, based on the intercomparison of the two
745 methodologies for the identification of *DD* episodes, is that the frequency of the episodes is higher for
746 the METHOD-B with respect to the primary methodology, while the intensity is decreased. Both facts
747 are expected and can be explained by the lower calculated *AOD* thresholds with METHOD-B thus
748 yielding more *DD* episodes of lower intensity.

750 4.3 Vertical structure of the Mediterranean desert dust outbreaks

751 The ability of the developed satellite algorithm to detect intense dust episodes has been proved
752 adequate through the comparison analysis against AERONET retrievals and PM_{10} concentrations
753 (Section 4.1). Nevertheless, its main limitation is that it uses columnar satellite retrievals and not
754 vertical resolved data prohibiting thus the description of the vertical structure of these dust outbreaks.
755 In order to address this issue, the CALIOP-CALIPSO retrievals are used as a complementary tool to
756 the satellite algorithm's outputs. First, for the identified dust episodes by the satellite algorithm, the
757 spatially and temporally collocated vertically resolved CALIOP lidar observations are selected. For
758 these cases and for each $1^\circ \times 1^\circ$ grid cell, we have divided the lower troposphere, up to 8 km, in 16
759 layers of 500 meters height. In this way, 14400 boxes of $1^\circ \times 1^\circ$ surface area and 500 meters height
760 have been produced. Then, for each one of them, we have calculated the overall number of dust and
761 polluted dust observations (hereafter named as dust) according to the aerosol subtyping scheme of the
762 CALIOP Vertical Feature Mask (*VFM*). Note that dust and polluted dust were chosen because in
763 previous studies (Mielonen et al., 2009) they were shown to be the best two defined aerosol types
764 among the other ones classified by the CALIOP *VFM*. Nevertheless, in case of polluted dust, Burton et
765 al. (2013) reported that dust particles can be mixed with marine aerosols instead of smoke or pollution
766 as assumed by the *VFM* retrieval algorithm. In our study, more than 95% of the aerosol type records
767 were pure dust, for the collocated cases between the satellite algorithm and CALIPSO observations. In
768 addition, in the majority of the defined boxes, the percentage of dust from the overall observations is
769 higher than 70%, confirming furthermore the validity of the algorithm *DD* episodes' identification
770 procedure. This is an excellent proof of the successful identification of *DD* episodes by the satellite
771 algorithm, since CALIOP-CALIPSO is an independent and vertically resolved platform and database.
772 Thereby, CALIOP vertical observations were subsequently used to examine the vertical structure of
773 dust outbreaks.

774 In order to analyze the intensity of desert dust outbreaks at different altitudes in the troposphere, the
775 CALIOP data of the total backscatter coefficient at 532 nm (β_{532nm}) have been also acquired. For each
776 box, the average β_{532nm} values have been calculated from all the available CALIOP measurements (day
777 and night), for the identified intense dust episodes by the satellite algorithm. More specifically, the
778 average β_{532nm} values were calculated for the dust observations based on the CALIOP *VFM* associated
779 with *CAD* scores ranging from -100 to -20, as it has been proposed by Winker et al. (2013) for

780 discriminating aerosol from clouds. The selection of β_{532nm} values instead of extinction coefficients
781 ensures that incorrect lidar ratio assumptions in the CALIOP retrieval algorithm do not affect our
782 results. In the literature, it has been documented that the CALIOP lidar ratio is underestimated over the
783 northern African deserts and the surrounding areas affected by Saharan dust particles, leading to an
784 underestimation of the columnar *AOD* compared to MODIS and AERONET retrievals (Redemann et
785 al., 2012; Schuster et al., 2012). Amiridis et al. (2013) stated that an increase of the lidar ratio from 40
786 to 58 sr, along with a series of post-corrections in the CALIOP retrievals and the implementation of
787 several criteria concerning the cloud coverage and the spatial representativeness, can improve
788 substantially the agreement between MODIS-Aqua/AERONET and CALIOP observations.

789 It should be noted that in the present work, we have analyzed all the available CALIOP overpasses
790 (~ 10000) over the study region, during the period Jun. 2006 – Feb. 2013. For brevity reasons,
791 however, only the obtained results based on MODIS-Terra retrievals are presented here, since similar
792 findings are drawn for MODIS-Aqua (Jun. 2006 – Dec. 2012). Moreover, the analysis (results are not
793 shown here) has been made separately for the identified strong and extreme *DD* episodes without
794 revealing remarkable differences in the geometrical characteristics of dust outbreaks. Nevertheless, the
795 β_{532nm} values are higher for the extreme *DD* episodes being consistent with the discrimination of dust
796 episodes' intensity (in terms of *AOD*) which is applied to the satellite algorithm. In order to facilitate
797 the visualization of our results, for each column ($1^\circ \times 1^\circ$ spatial resolution) and latitudinal/longitudinal
798 zone (1° degree), we have calculated the overall number of dust observations and the associated
799 weighted averages of β_{532nm} , depending on the projection plane (latitudinal, longitudinal and columnar),
800 according to dust observations in each box. For both parameters, the analysis has been made on an
801 annual and seasonal basis and the corresponding results are discussed in Sections 4.3.1 and 4.3.2,
802 respectively.

803

804 4.3.1 Annual characteristics

805 In Figure 8, are presented the three dimensional structures of the CALIOP overall dust observations
806 (Fig. 8-i) and the associated total backscatter coefficients at 532 nm (Fig. 8-ii), during intense dust
807 episodes conditions, over the broader Mediterranean area, for the period Jun. 2006 – Feb. 2013. From
808 the latitudinal projection in Fig. 8-i, it is evident that dust particles are mainly detected between 0.5 and
809 6 km, and more rarely up to 8 km, between the parallels 32° N and 38° N. The number of dust
810 observations is increased at higher altitudes with increasing latitudes, up to 40° N, while the altitude

811 range (thickness) where these records are detected is gradually reduced from 4 to 2 km. At northern
812 latitudes, the CALIPSO dust records are drastically reduced and are mainly observed between 1 and 4
813 km. The ascending mode of the transported mineral particles over the Mediterranean is attributed to the
814 prevailing low pressure systems, which mobilize and uplift dust particles from the source areas across
815 the Sahara Desert and the Arabian Peninsula. Dust aerosols are transported over the planetary boundary
816 layer (Hamonou et al., 1999) due to the upward movement of dry and turbid air masses (Dulac et al.,
817 1992), while the prevailing synoptic conditions determine also the spatial and temporal characteristics
818 of desert dust outbreaks over the Mediterranean (Gkikas et al., 2015).

819 In general, our results are in agreement with previous studies, based on lidar profiles, which have
820 been made in several Mediterranean sites. More specifically, Papayannis et al. (2008) found that dust
821 layers, over the EARLINET Mediterranean stations, extend from 0.5 to 10 km above mean sea level,
822 their center of mass is located between 2.5 and 3.5 km and their thickness ranges from 2.1 to 3.3 km.
823 Hamonou et al. (1999) reported that dust layers are mainly detected between 1.5 and 5 km based on
824 lidar measurements in the northwestern and northeastern Mediterranean. According to di Sarra et al.
825 (2001), who studied the Saharan dust intrusions in Lampedusa (central Mediterranean) for the period
826 May-June 1999, dust particles can be detected up to 7-8 km, which is in line with our findings for the
827 corresponding latitudinal zones (35° N - 36 ° N). Balis (2012), analyzed 33 Raman/lidar profiles of
828 Saharan dust intrusions over Thessaloniki (northern Greece), and found that the mean base and top of
829 dust layers were equal to 2.5 ± 0.9 and 4.2 ± 1.5 km, respectively.

830 As to the variation of vertical extension with longitude (Fig. 8-i), it is revealed that the base height
831 of dust layers is decreased towards the eastern parts of the study region. In the western Mediterranean,
832 the mineral particles are mainly detected between 2 and 6 km while over the central and eastern
833 Mediterranean the corresponding altitudes are equal to 0.5 and 6 km, respectively. It is well known,
834 that dust is transported over the western Mediterranean mainly in summer (e.g. Moulin et al., 1998)
835 favored by low pressure systems located over the northwestern Africa (Gkikas et al., 2015) and the
836 enhanced thermal convection, uplifting effectively dust aerosols at high altitudes in the troposphere.
837 Moreover, air masses carrying dust particles are “convected” towards higher altitudes due to the
838 existence of the Atlas Mountains Range. Therefore, the combination of strong convective processes
839 over North Africa along with topography can explain the identification of dust aerosols at higher
840 tropospheric levels over the western Mediterranean. It is the presence of mineral particles at high
841 altitudes in western Mediterranean that can explain the poor-to-moderate agreement between PM_{10}
842 concentrations and MODIS AODs found in the Iberian Peninsula (Fig. 5-ii). In order to give a better

843 insight to how the dust outbreaks' vertical extension can affect the level of agreement between
844 columnar *AOD* satellite retrievals and ground *PM*₁₀ concentrations, emphasis is given at specific dust
845 events and the relevant findings will be discussed in section 4.4. In the central and eastern parts of the
846 Mediterranean basin, air masses carrying African dust aerosols travel at lower altitudes over Africa
847 because of absence of significant topographical objects on their route, as suggested by Pey et al.
848 (2013).

849 Previous studies have shown that dust layers over the Mediterranean are characterized by a
850 multilayered structure (e.g. Hamonou et al., 1999; Mona et al., 2006; Papayannis et al., 2008). This is
851 also depicted in the longitudinal projection of Figure 8-i, where several dust layers of different base/top
852 altitudes and geometrical thicknesses are detected. In general, the base heights vary from 0.5 to 2 km,
853 the top heights from 4 to 6 km and the thicknesses from 1 to 4 km. The majority of common
854 observations between the CALIOP profiles and the identified intense *DD* episodes by the satellite
855 algorithm are recorded over the maritime parts of the study region (bottom map of Fig. 8-i). The
856 maximum number of CALIOP dust observations (~ 19000) is recorded along the Atlantic coasts of
857 Morocco, but high numbers (about 10000 – 15000) are also found across the northern African coasts.

858 Apart from the CALIOP dust observations, we have also analyzed the associated β_{532nm} values at
859 the defined altitude ranges in order to describe the variation of intensity of the desert dust episodes with
860 height over the Mediterranean (Fig. 8-ii). The maximum backscatter coefficients (up to $0.006 \text{ km}^{-1} \text{ sr}^{-1}$)
861 are observed below 2 km, being increased towards the southern edges ($30^\circ \text{ N} - 34^\circ \text{ N}$) of the study
862 region, close to dust source areas. This is explained by the fact that dust particles due to their coarse
863 size and large mass, are efficiently deposited and for this reason they are recorded at higher
864 concentrations near to the source areas and at low altitudes. Nevertheless, the decreasing intensity with
865 height towards the north is not so evident. Thus, high β_{532nm} values ($\sim 0.004 \text{ km}^{-1} \text{ sr}^{-1}$) are observed
866 between 2 and 4 km in the latitudinal zone extending from 35° N to 42° N . Though, the uppermost
867 altitudes where relatively high β_{532nm} values gradually decrease from 6 to 4 km, moving from south to
868 north. Any differences in the latitudinal patterns of dust observations and backscatter values (Figs 8-i
869 and 8-ii) can be explained by the fact that β_{532nm} values take into account only the dust records and not
870 the overall observations (all aerosol types).

871 The decrease of backscatter values at higher altitudes has been pointed out in previous studies
872 where lidar profiles have been analyzed over specific Mediterranean locations (e.g. Mona et al., 2006;
873 Papayannis et al., 2008). Nevertheless, it must be considered that in the aforementioned studies the

874 lidar measurements are valid above the retrieved planetary boundary layer (Matthias et al., 2004) which
875 varies depending on the location and the season (McGrath-Spangler et al., 2013). Despite the good
876 agreement, as it concerns the vertical shape of the β_{532nm} curves, between our findings and the
877 corresponding ones based on ground retrievals, in the present analysis the calculated backscatter
878 coefficients are in general higher, which is reasonable since are considered only cases of intense desert
879 dust outbreaks.

880 The longitudinal pattern of β_{532nm} profiles (Fig. 8-ii) is less distinct compared to the corresponding
881 one resulted from the latitudinal projection. Relatively high β_{532nm} values ($\sim 0.004 \text{ km}^{-1} \text{ sr}^{-1}$) are found
882 between 1 and 5 km over the western Mediterranean, while over the central and eastern parts of the
883 study region the desert dust outbreaks' intensity ($\sim 0.006 \text{ km}^{-1} \text{ sr}^{-1}$) is higher below 1.5 km. Among the
884 sub-regions, the backscatter coefficients are higher in the central and eastern Mediterranean, which is
885 also depicted in the bottom map of Fig. 8-ii. It is reminded that higher intensities of dust episodes over
886 the central and eastern Mediterranean have also been noticed based on MODIS retrievals (Figure 7).
887 From the obtained longitudinal projection, it is evident a patchy structure of the total backscatter
888 coefficient profiles, especially in the central and eastern parts, indicating the existence of several dust
889 layers of varying intensities at different altitudes into the atmosphere.

890 The three dimensional plots of Figures 8-i and 8-ii, have been also reproduced considering all the
891 available dust and polluted dust CALIOP-CALIPSO records, without taking into account the satellite
892 algorithm's outputs (intense dust outbreaks). The obtained results for the number of observations and
893 β_{532nm} are presented in Figures S9-i and S9-ii, respectively. Note, that for each studied parameter the
894 colorbar scales in Figure 8 and S9 are not identical because the number of observations for dust
895 average conditions (Fig. S9-i) is extremely larger than the corresponding one during intense dust
896 outbreaks (Fig. 8-i) while the opposite is found for the β_{532nm} values (Fig. 8-ii and Fig. S9-ii). It is
897 apparent that the latitudinal projections calculated for the intense dust outbreaks (Fig. 8-i) and for all
898 the available CALIOP dust records (Fig. S9-i) reveal different patterns. More specifically, when all
899 available CALIOP dust records are considered, it is found that dust aerosols are mainly confined
900 between 1 and 3 km in the southernmost parts of the study region while the number of observations
901 gradually decreases at higher altitudes and towards northern latitudes (Fig. S9-i). On the contrary,
902 during dust outbreaks, mineral particles are transported over the Mediterranean following an ascending
903 path, as it is depicted in the latitudinal projection of Figure 8-i. Nevertheless, it must be mentioned that
904 over the desert areas there is a full coverage (see bottom map in Fig. S9-i) when all dust CALIOP
905 records are considered in contrast to intense dust outbreaks (see bottom map in Fig. 8-i) attributed to

906 the absence of *DT* retrievals, used as inputs to the satellite algorithm, over bright surfaces. The
907 comparison between the longitudinal projections during intense dust outbreaks (Figure 8-i) and during
908 average dust conditions (Fig. S9-i) reveals less remarkable differences than for the latitudinal
909 projections. According to the longitudinal projection of Figure S9-i, in the western Mediterranean, dust
910 layers are confined between 1 and 5 km, while their base and top altitude both decrease down to 0.5
911 and 4 km, respectively, for increasing longitudes. In the easternmost part of the study region, dust
912 layers are mainly confined between 1 and 3 km, while its top height can reach up to 5 km. The intensity
913 of dust loads (in terms of β_{532nm}) is lower than $0.003 \text{ km}^{-1} \text{ sr}^{-1}$ regardless the projection plane for
914 average dust conditions based on CALIOP-CALIPSO lidar profiles (Fig. S9-ii). Moreover, the intensity
915 of dust loads decreases gradually with height as well as from south to north revealing a distinct pattern
916 in all projection planes in contrast to the corresponding ones found during desert dust outbreaks (Fig. 8-
917 ii).

918

919 4.3.2 Seasonal characteristics

920 The vertical structure of the Mediterranean desert dust outbreaks has also been analyzed separately
921 for winter (*DJF*), spring (*MAM*), summer (*JJA*) and autumn (*SON*). The seasonal three dimensional
922 representations of the CALIOP overall dust observations and the associated total backscatter
923 coefficients are depicted in the left and right column of Figure 9, respectively. It must be noted, that for
924 β_{532nm} the colorbars' ranges are common, depending on the projection plane. More specifically, the
925 maximum limits have been set to $0.012 \text{ km}^{-1} \text{ sr}^{-1}$, $0.014 \text{ km}^{-1} \text{ sr}^{-1}$ and $0.021 \text{ km}^{-1} \text{ sr}^{-1}$ for the latitudinal,
926 longitudinal and bottom map projections, respectively. It should be mentioned that β_{532nm} values can
927 reach up to $0.045 \text{ km}^{-1} \text{ sr}^{-1}$, but are associated with a very small number of dust observations.

928 The majority (85%) of dust observations is recorded in spring and summer, attributed to the
929 enhanced production rates of mineral particles and the prevailing atmospheric circulation over the
930 source areas and the Mediterranean. According to the latitudinal projections, it is evident a seasonal
931 variability of the intense Mediterranean desert dust outbreaks' geometrical characteristics. Dust
932 particles are detected at higher altitudes (6-7 km) during warm seasons of the year while in winter are
933 mainly detected below 3 km and in autumn are recorded between 2 and 5 km. Nevertheless, it should
934 be mentioned that during these seasons only a small number of pixels (see bottom maps in Figs. 9 i-a,
935 iv-a) is available considering also that clouds prohibit the satellite observations. Note that in spring,
936 dust can be found at low tropospheric levels while in summer it is mainly observed above 1 km

937 highlighting thus the role of topography and the enhanced thermal convection. During the first half of
938 the year, the maximum dust observations are confined between the parallels 31° N and 37° N while
939 during the second one, are shifted northwards in the latitudinal zone extending from 34° N to 40° N.
940 Similar latitudinal projections were also presented by Luo et al. (2015), for the same zonal areas of the
941 study region, who developed a new algorithm to improve CALIOP's ability to detect optically thin dust
942 layers. From the longitudinal projections as well as from the bottom maps, it is evident that the
943 maximum dust records are found in different Mediterranean sub-regions, depending on the season. The
944 geometrical characteristics, in longitudinal terms, of intense *DD* episodes affecting the western, central
945 and eastern parts of the Mediterranean are similar to those presented in the annual three dimensional
946 structure (Fig. 8-i) being more frequent in the eastern and central Mediterranean in winter, spring and
947 autumn and in the western and central Mediterranean in summer.

948 The seasonal patterns of β_{532nm} latitudinal projections are different than those for the dust
949 observations, while they also differ among the four seasons. The intensity of winter *DD* episodes is
950 stronger (up to $0.012 \text{ km}^{-1} \text{ sr}^{-1}$) below 2 km and at the southern parts of the study region. According to
951 the longitudinal and bottom map projections, these episodes take place over the central and eastern
952 Mediterranean Sea but the number of grid cells with coincident CALIOP observations and *DD* episodes
953 is limited. In spring, the highest β_{532nm} values (up to $0.006 \text{ km}^{-1} \text{ sr}^{-1}$) are recorded between the parallels
954 31° N and 35° N and below 2 km, although, relatively high β_{532nm} values (up to $0.004 \text{ km}^{-1} \text{ sr}^{-1}$) are
955 found up to 5 km (Fig. 9 ii-b). Moving northwards, over the Mediterranean, dust layers are mainly
956 confined between 2 and 4 km, associated with high β_{532nm} values (up to $0.004 \text{ km}^{-1} \text{ sr}^{-1}$) in the
957 latitudinal zone extending from 35° N to 43° N. The existence of these elevated dust layers, has been
958 also confirmed by model simulations through specific (Papayannis et al., 2008; 2014) or averaged
959 (Alpert et al., 2004) cross sections of dust concentrations in the central sector of the Mediterranean.
960 This is in accordance with our longitudinal projection (Fig. 9 ii-b), where β_{532nm} is high varying from
961 0.004 to $0.008 \text{ km}^{-1} \text{ sr}^{-1}$ at these altitude ranges.

962 In summer, the intensity of dust episodes is smoothly decreased at higher altitudes, where dust
963 layers of considerable β_{532nm} values are also found. More specifically, the highest backscatter
964 coefficients (up to $0.008 \text{ km}^{-1} \text{ sr}^{-1}$) are recorded near to the surface but also moderate values (up to
965 $0.006 \text{ km}^{-1} \text{ sr}^{-1}$) are observed between 2 and 5 km, particularly over the southern parts of the study
966 region (Fig. 9 iii-b). Most of these intense *DD* episodes occur in the western Mediterranean, where the
967 highest β_{532nm} values (up to $0.005 \text{ km}^{-1} \text{ sr}^{-1}$) are recorded between 2 and 5 km. Over the central and
968 eastern Mediterranean, even higher β_{532nm} values are found (up to $0.014 \text{ km}^{-1} \text{ sr}^{-1}$) but at lower altitudes

969 (< 1 km). In autumn, the majority of the grid cells of coincident CALIOP profiles and *DD* episodes
970 identified by the satellite algorithm are located between the parallels 33° N and 41° N. In this
971 latitudinal zone, CALIOP profiles are available over the interior parts of the Iberian Peninsula and over
972 western and central parts of the Mediterranean Sea, near to the northern African coasts. According to
973 the latitudinal projection, β_{532nm} values mainly vary from 0.002 to 0.009 km⁻¹ sr⁻¹, revealing an
974 increasing tendency for increasing heights. On the contrary, the total backscatter coefficients do not
975 show a distinct spatial pattern on the longitudinal projection, due to the limited number of grid cells
976 participating in the calculations. Throughout the year, based on the CALIOP β_{532nm} retrievals, the *DD*
977 episodes are more intense (up to 0.018 km⁻¹ sr⁻¹) in spring, when massive dust loads are transported
978 from the Sahara desert towards the central and eastern parts of the Mediterranean Sea (bottom map in
979 Fig. 9 ii-b).

980

981 4.4. Intercomparison of satellite AOD and PM₁₀ concentrations for specific desert dust outbreaks

982 In Section 4.1.2, it has been shown that the agreement between the satellite algorithm's outputs and
983 *PM*₁₀ concentrations is better in the central and eastern Mediterranean with regards to the western parts
984 (Figure 5-ii). This discrepancy has been mainly attributed to the higher altitude of dust layers' base
985 over the western sector of the study domain (Figure 8-i), in relation to the existing areal orography.
986 Here, aiming at addressing how dust layers' geometrical characteristics influence the agreement
987 between columnar *AOD* satellite and ground *PM*₁₀ measurements, specific desert dust outbreaks that
988 took place over the *PM*₁₀ stations are analyzed. These outbreaks were selected based on concurrent
989 fulfillment of the following criteria: (i) a *DD* episode must be identified by the satellite algorithm at
990 pixel level (at 1° x 1° grid cell), (ii) total *PM*₁₀ measurement must be available at the station which lies
991 into the geographical limits of the corresponding grid cell and (iii) CALIPSO flies across the grid cell.
992 These criteria were met for 13 desert dust outbreaks, which took place over 9 *PM*₁₀ stations during the
993 period Jun. 2006 – Feb. 2013. Similarities were found among the identified cases and therefore only the
994 results for four desert dust outbreaks of different geometrical characteristics are discussed in the present
995 section. For each case, we have reproduced the cross sections of the β_{532nm} vertical profiles up to 8 km
996 above sea level (a.s.l.) along the CALIOP-CALIPSO track when the satellite flies near the *PM*₁₀ site
997 (Figures 10-12). Moreover, the corresponding aerosol subtype profiles, acquired from the CALIOP
998 website (http://www-calipso.larc.nasa.gov/products/lidar/browse_images/production/), are provided in
999 the supplementary material (Figures S10-S12). Since the *PM*₁₀ concentrations are available only as

1000 daily averages, the optimum solution would be to have the maximum number (2) of CALIOP
1001 overpasses near PM_{10} site throughout the day, in order to reduce the temporal inconsistencies between
1002 satellite vertical resolved retrievals and ground data. However, in 8 out of 13 desert dust outbreaks this
1003 was not feasible.

1004

1005 4.4.1 Case 1: 26th May 2008

1006 The first study case refers to a desert dust outbreak that took place on 26th May 2008 and affected
1007 the station Censt (Lat: 39.064, Lon: 8.457) located in southern Sardinia. At the ground, the measured
1008 mean daily total PM_{10} concentration was $19 \mu\text{g m}^{-3}$ whereas 68% (or $13 \mu\text{g m}^{-3}$) of the load consisted of
1009 dust particles indicating thus their strong presence in the lowest troposphere. Based on MODIS-Terra
1010 retrievals, representative for the whole atmospheric column and grid cell, the aerosol optical depth at
1011 550 nm was equal to 0.81. In order to investigate the vertical distribution of the dust outbreak, the cross
1012 sections of the β_{532nm} vertical profiles along CALIOP track, near the station, during daytime and
1013 nighttime have been reproduced and depicted in Figures 10-i and 10-ii, respectively. In addition, the
1014 corresponding aerosol subtype profiles are provided in Figures S10-i and S10-ii in the supplementary
1015 material. During night, it is evident the predominance of a well-developed dust layer mixed with
1016 polluted aerosols (Figure S10-i) extending from surface up to 5 km a.s.l. between the parallels 33° N
1017 and 38° N, while near the station its top is lowered down to 3 km (left side of Figure 10-i). Moreover,
1018 the β_{532nm} values range mainly from 0.002 to 0.003 $\text{km}^{-1} \text{sr}^{-1}$ without revealing remarkable variations,
1019 thus indicating a rather compact dust layer. According to the daytime CALIOP overpass (Figure 10-ii),
1020 a pure dust layer (Figure S10-ii) is confined between surface and 4 km, affecting the surrounding area
1021 of the station, while its intensity (in terms of β_{532nm}) varies slightly from 0.0015 to 0.002 $\text{km}^{-1} \text{sr}^{-1}$.
1022 Nevertheless, due to the background solar illumination, leading thus to a lower signal-to-noise ratio
1023 (Nowottnick et al., 2015), the “borders” of the dust plume during daytime are not so distinct in contrast
1024 to nighttime. According to the obtained results, the ground-based measurements are able to capture
1025 satisfactorily the dust event when its load is equally distributed in the lowest tropospheric levels,
1026 resulting thus to a good agreement between MODIS and PM_{10} observations.

1027

1028

1029

1030 4.4.2 Case 2 and 3: 16th July 2008 and 12th September 2007

1031 Two dust events that affected Els Torms (NE Spain, Lat: 41.395, Lon: 0.721) and San Pablo
1032 (central Spain, Lat: 39.525, Lon: -4.353) on 16th July 2008 and 12th September 2007, respectively, are
1033 studied here. The daily averages of the total PM_{10} concentrations were equal to 16 and 30 $\mu\text{g m}^{-3}$,
1034 respectively, whereas the dust particles' contribution (dust PM_{10}) to the total amount was zero in Els
1035 Torms and 33 % in San Pablo. On the contrary, the MODIS-Terra level 3 AOD retrievals were high and
1036 equal to 0.56 (Els Torms) and 0.64 (San Pablo), indicating the existence of dust aerosols according to
1037 the satellite algorithm's classification method. In order to give a better insight, aiming at describing the
1038 discrepancies between MODIS-Terra AOD and PM_{10} concentrations, we have reproduced the cross
1039 sections of the total backscatter at 532 nm when CALIPSO flies, during daytime, near Els Torms
1040 (Figure 11-i) and San Pablo (Figure 11-ii). The corresponding profiles of the CALIOP aerosol
1041 classification scheme are also available in Figures S11-i and S11-ii. In Els Torms, where the dust PM_{10}
1042 concentration was zero, a dust layer (Figure S11-i) with its base at 3.5 km a.s.l. and its top at 5 km
1043 a.s.l., is recorded by the CALIOP lidar between the parallels 41° N and 43° N. The intensity of the
1044 elevated dust layer, in terms of β_{532nm} , varies from 0.002 to 0.004 $\text{km}^{-1} \text{sr}^{-1}$ (Figure 11-i). Through
1045 CALIOP lidar profiles, it is confirmed the existence of a dust layer aloft, which cannot be captured by
1046 the PM_{10} measurements in contrast to the MODIS spectroradiometer. In San Pablo, where the dust
1047 particles' contribution to the total PM_{10} load was equal to 33 %, a dust layer abuts the ground extending
1048 up to 5-6 km a.s.l., whereas the dust plume covers a wide range, in latitudinal terms, from the sub-Sahel
1049 to the Celtic Sea, affecting the Iberian Peninsula (Figure S11-ii). Nevertheless, the intensity of the dust
1050 layer, over the surrounding area of the station, differs with altitude being higher between 2.5 and 5 km
1051 a.s.l. (0.004 to 0.007 $\text{km}^{-1} \text{sr}^{-1}$) and lower between ground and 2 km a.s.l. ($< 0.003 \text{ km}^{-1} \text{sr}^{-1}$), as it is
1052 depicted in the middle of Figure 11-ii. The two studied cases here differ from Case 1 (Section 4.4.1)
1053 either with regards to the position of the elevated dust layer (Els Torms) or to its vertical distribution
1054 (San Pablo), which explains the poor agreement between satellite columnar AOD retrievals (MODIS)
1055 and ground PM_{10} concentrations.

1056

1057

1058

1059

1060 4.4.3 Case 4: 25th February 2007

1061 The case studied here, namely the desert dust outbreak recorded in Agia Marina (Cyprus, Lat:
1062 35.039, Lon: 33.058) on 25th February 2007, is the strongest one among the selected cases. More
1063 specifically, the daily average of the dust PM_{10} concentration was equal to $134 \mu\text{g m}^{-3}$ accounting for
1064 the 92 % of the total PM_{10} measured amount at the station, which is indicative of the strong
1065 predominance of dust particles in the lowest troposphere. The MODIS-Terra level 3 AOD value for the
1066 grid cell to which the station it is found is high and equal to 1.04. According to the CALIOP aerosol
1067 classification scheme, during nighttime, a shallow low-elevated dust layer mixed with polluted or
1068 marine aerosols is heading towards the station, whereas above the PM_{10} site (Agia Marina) extends
1069 from close to the ground up to 9 km a.s.l., comprising only pure dust aerosols (Figure S12). The main
1070 part of the dust layer, in the surrounding area of the station, is confined between 2.5 and 4 km a.s.l.
1071 where the maximum β_{532nm} values (up to $0.006 \text{ km}^{-1} \text{ sr}^{-1}$) are observed (Figure 12). Also, similar β_{532nm}
1072 values are recorded below 1 km a.s.l.; however, the dust layer is not well represented in the cross
1073 section of the CALIOP β_{532nm} vertical profiles due to the total attenuation of the lidar beam by clouds
1074 (located between 3 and 4 km a.s.l.) superimposed to the low-elevated dust layer.

1075

1076 5. Summary and conclusions

1077 This study aims at describing the vertical structure of intense desert dust outbreaks affecting the
1078 broader Mediterranean basin. To achieve this target, an updated version of an objective and dynamic
1079 algorithm, which has been introduced by Gkikas et al. (2009; 2013), has been applied for the
1080 identification of strong and extreme desert dust episodes, over the period Mar. 2000 – Feb. 2013. For
1081 its operation, a group of optical properties, retrieved by satellite sensors (MODIS-Terra/Aqua, EP-
1082 TOMS and OMI-Aura) on a daily basis, is used, providing information about aerosols' load, size and
1083 nature. Briefly, the satellite algorithm consists of three parts; at the first one are computed the mean
1084 AOD value ($Mean$) and the associated standard deviation (Std) for the whole study period in each grid
1085 cell of $1^\circ \times 1^\circ$ spatial resolution, at the second one the identified aerosol episodes are classified based
1086 on their intensity to strong and extreme ones. Finally, at the third part the identified aerosol episodes
1087 are categorized as desert dust episodes, separately over land and sea. Through this approach the
1088 selected dataset consists only of intense desert dust episodes since their intensity (expressed in terms of
1089 AOD_{550nm}) is higher/equal than $Mean + 2*Std$. The DD episodes have also been determined by

1090 applying an alternative second methodology (METHOD-B) which excludes dust-affected cases
1091 identified based on the criteria set concerning the aerosol size/nature related optical properties.

1092 Through the comparison of the default version of the satellite algorithm against surface
1093 measurements derived from 109 AERONET and 22 PM_{10} stations, it is found that:

1094 AERONET

- 1095 ➤ The correlation coefficient between MODIS and AERONET AOD_s is increased from 0.505 to
1096 0.750 when level 3 grid cells with higher sub-grid spatial representativeness and homogeneity
1097 are considered.
- 1098 ➤ According to the AERONET volume size distributions, it is evident the predominance of the
1099 coarse mode with a peak ($\sim 0.25 \mu\text{m}^3 \mu\text{m}^{-2}$) for particles radii between 1.70 and 2.24 μm , in
1100 case of intense DD episodes.
- 1101 ➤ The appropriateness of DD episodes' identification method applied to the satellite algorithm is
1102 confirmed since the majority ($> 75\%$) of AERONET $\alpha_{440-870\text{nm}}$ and r_{eff} values are lower than
1103 0.54 and higher than 0.55 μm , respectively.
- 1104 ➤ About 15% of the pixel level intense DD episodes are misclassified by the satellite algorithm
1105 and these drawbacks are encountered in AERONET stations where the aerosol load is
1106 dominated either by fine particles or by complex aerosol types.

1107 PM_{10} and dust contribution

- 1108 ➤ The agreement between surface and satellite measurements is better over the central and eastern
1109 Mediterranean stations.
- 1110 ➤ On a station level, the percentage of the intense DD episodes, for which a dust contribution to
1111 PM_{10} surface concentration has been recorded, varies from 68% (Monagrega, northeastern
1112 Spain) to 97% (Boccadifalco, Sicily).
- 1113 ➤ In the majority of stations, dust particles contribute more than 50% of the total amount reaching
1114 up to 86.8% (Agia Marina, Cyprus).
- 1115 ➤ The mean PM_{10} concentration levels mainly vary from 20 to 50 $\mu\text{g m}^{-3}$ reaching up to 223 $\mu\text{g m}^{-3}$
1116 in Agia Marina (Cyprus).

1117 Based on the satellite algorithm's outputs, an overall view about the regime of Mediterranean desert
1118 dust outbreaks is presented for the periods Mar. 2000 – Feb. 2013 (MODIS-Terra) and 2003-2012

1119 (MODIS-Aqua). The main findings concerning the intense *DD* episodes' frequency (in terms of
1120 episodes yr⁻¹) and intensity (in terms of *AOD* at 550nm) are the following:

- 1121 ➤ Strong *DD* episodes occur more frequently (up to 9.9 episodes yr⁻¹) in the western
1122 Mediterranean while the extreme ones occur more frequently (up to 3.3 episodes yr⁻¹) over the
1123 central parts of the Mediterranean Sea, when the satellite algorithm operates with MODIS-Terra
1124 retrievals.
- 1125 ➤ The intensity of strong and extreme *DD* episodes, in *AOD* terms, can reach to 1.5 and 3-4,
1126 respectively, over the central and eastern parts of the Mediterranean Sea, near off the northern
1127 African coasts.
- 1128 ➤ Slightly lower frequencies and higher intensities are found for the period 2003-2012, when the
1129 satellite algorithm operates with MODIS-Aqua retrievals.
- 1130 ➤ Through the intercomparison between the two applied methodologies, it is revealed that the
1131 geographical patterns of frequency of occurrence are similar both for strong and extreme *DD*
1132 episodes; however, higher frequencies are found based on METHOD-B.
- 1133 ➤ Based on METHOD-B, the *DD* episodes' intensities are decreased whereas the geographical
1134 patterns for the strong *DD* episodes are not so distinct compared to the corresponding results
1135 obtained by the default version of the satellite algorithm.
- 1136 ➤ The similarity between the outputs of the algorithm using the two methodologies shows the
1137 consistency of the algorithm and the validity of its concept.

1138

1139 In order to describe the vertical structure of the intense Mediterranean dust outbreaks, the CALIOP
1140 vertical profiles of aerosol subtyping and total backscatter coefficient at 532 nm, are used as a
1141 complementary tool to the identified intense *DD* episodes by the satellite algorithm. Through this
1142 synergistic approach it is found that:

- 1143 ➤ Dust particles are mainly detected between 0.5 and 6 km, following an ascending mode, up to
1144 40° N, leaving from the source areas and transported towards the Mediterranean.
- 1145 ➤ Over the western Mediterranean, the dust layers are mainly observed between 2 and 6 km while
1146 their base height is decreased down to 0.5 km for increasing longitudes.
- 1147 ➤ During the warm period of the year, dust particles are uplifted at higher altitudes (up to 8 km).
- 1148 ➤ In summer, the transported dust loads over the western Mediterranean are recorded above 1 km
1149 and in spring at lower altitudes over the central and eastern parts of the study region. This

1150 behavior underlies the role of topography (e.g. Atlas Mountains) and the enhanced thermal
1151 convection.

- 1152 ➤ The intensity of dust outbreaks, in terms of β_{532nm} , is maximized (up to $0.006 \text{ km}^{-1} \text{ sr}^{-1}$) below 2
1153 km and at the southern parts ($30^\circ \text{ N} - 34^\circ \text{ N}$) of the study region.
- 1154 ➤ In spring, considerably high β_{532nm} values ($\sim 0.004 \text{ km}^{-1} \text{ sr}^{-1}$) are observed between 2 and 4 km
1155 in the latitudinal zone extending from 35° N to 42° N .
- 1156 ➤ Moderate-to-high β_{532nm} values are observed up to 6 km, near to the source areas, while the top
1157 of dust layers is gradually decreased down to 4 km towards northern latitudes.
- 1158 ➤ From the longitudinal projection of β_{532nm} , it is evident that *DD* episodes are more intense (\sim
1159 $0.004 \text{ km}^{-1} \text{ sr}^{-1}$) between 1 and 5 km in the western Mediterranean, while over the central and
1160 eastern sectors, the maximum intensities ($\sim 0.006 \text{ km}^{-1} \text{ sr}^{-1}$) are recorded below 1.5 km.
- 1161 ➤ On a seasonal basis, *DD* episodes are found to be more intense (up to $0.018 \text{ km}^{-1} \text{ sr}^{-1}$) in spring,
1162 when dust is transported towards the central and eastern parts of the Mediterranean region.

1163 At the last part of the present study, it is investigated how the desert dust outbreaks' vertical
1164 distribution can affect the level of agreement between columnar satellite *AOD* retrievals (MODIS) and
1165 ground PM_{10} concentrations. For this purpose, four intense Mediterranean desert dust outbreaks of
1166 different geometrical characteristics that took place across the Mediterranean, namely in Spain
1167 (western), Italy (central) and Cyprus (eastern), are studied when satellite algorithm's outputs, ground
1168 PM_{10} concentrations and CALIOP-CALIPSO lidar profiles are available concurrently. Our analysis
1169 clearly shows that when a well-developed and compact dust layer is located in the lowest tropospheric
1170 levels, then the level of agreement between MODIS- PM_{10} is high. On the contrary, when the dust layer
1171 is aloft or its load is not equally distributed in vertical terms then a poor agreement between MODIS-
1172 PM_{10} is found.

1173 This study attempts to highlight the importance of the synergistic use of satellite observations and
1174 the usage of surface-based measurements, targeting to the representation of the 3D structure of dust
1175 outbreaks and the description of their spatial and temporal features. For this reason, the further
1176 development of the satellite algorithm is an ongoing process by our group, aiming at extending the
1177 study domain from regional to global scale, considering the latest version of MODIS retrievals
1178 (Collection 006) as well as the Deep Blue Algorithm retrievals, available over the major dust sources of
1179 the planet.

1180

1181 **Acknowledgements**

1182 The MDRAF project has received funding from the European Union's Seventh Framework
1183 Programme for research, technological development and demonstration under grant agreement no
1184 622662. The Collection 051 MODIS-Terra and MODIS-Aqua data were obtained from NASA's Level
1185 1 and Atmosphere Archive and Distribution System (LAADS) website
1186 (<ftp://ladsweb.nascom.nasa.gov/>). The Earth Probe (TOMS) and OMI aerosol climatology is available
1187 from the Mirador ftp server (<http://mirador.gsfc.nasa.gov/>). The CALIPSO retrievals have been derived
1188 from NASA's Earth Observing System Data and Information System (<http://reverb.echo.nasa.gov/>).
1189 We would like to thank the principal investigators maintaining the AERONET sites used in the present
1190 work. We would like to acknowledge the EMEP Programme and the public European databases
1191 Airbase and ACTRIS, which supplied PM₁₀ data used in this study. J. Pey benefits from a Ramón y
1192 Cajal Research Grant (RYC-2013-14159) from the Spanish Ministry of Economy and Competitiveness.
1193 S. Basart, O. Jorba, S. Gassó and J.M. Baldasano acknowledge the CICYT project CGL2013-46736
1194 and Severo Ochoa (SEV-996 2011-00067) programme of the Spanish Government. The publication
1195 was supported by the European Union Seventh Framework Programme (FP-7-REGPOT-2012-2013-1),
1196 in the framework of the project BEYOND, under Grant Agreement No. 316210 (BEYOND – Building
1197 Capacity for a Centre of Excellence for EO-based monitoring of Natural Disasters. The figures 10, 11
1198 and 12 have been produced with ccplot (<http://ccplot.org/>). This work is contributing to the Chemistry-
1199 Aerosol Mediterranean Experiment (ChArMEx) coordinated effort for the long-term Mediterranean
1200 aerosol characterization using available remote sensing datasets.

1201

1202 **References**

- 1203 Adams, A. M., Prospero, J. M., and Zhang, C.: CALIPSO-derived three-dimensional structure of
1204 aerosol over the Atlantic Basin and adjacent continents, *J. Climate*, 25, 6862–6879, doi:10.1175/JCLI-
1205 D-11-00672.1, 2012.
- 1206 Alados-Arboledas, A., Alcántara, A., Olmo, F. J., Martínez-Lozano, J. A., Estellés, V., Cachorro, V.,
1207 Silva, A. M., Horvath, H., Gangl, A., Díaz, A., Pujadas, M., Lorente, J., Labajo, A., Sorribas, M., and
1208 Pavese, G.: Aerosol columnar properties retrieved from Cimel radiometers during VELETA 2002,
1209 *Atmos. Environ.*, 42, 2630–2642, [doi:10.1016/j.atmosenv.2007.10.006](https://doi.org/10.1016/j.atmosenv.2007.10.006), 2008.

1210 Alam, K., Trautmann, T., Blaschke, T., Subhan, F.: Changes in aerosol optical properties due to dust
1211 storms in the Middle East and Southwest Asia, *Remote Sens. Environ.* 143, 216–227,
1212 doi:10.1016/j.rse.2013.12.021, 2014.

1213 Alpert, P., Kishcha, P., Shtivelman, A., Krichak, S.O., Joseph, J.H.: Vertical distribution of Saharan
1214 dust based on 2.5-year model predictions, *Atmos. Res.*, 70, 109-130,
1215 doi:10.1016/j.atmosres.2003.11.001, 2004.

1216 Amiridis, V., Kafatos, M., Pérez, C., Kazadzis, S., Gerasopoulos, E., Mamouri, R. E., Papayannis, A.,
1217 Kokkalis, P., Giannakaki, E., Basart, S., Daglis, I., and Zerefos, C.: The potential of the synergistic use
1218 of passive and active remote sensing measurements for the validation of a regional dust model, *Ann.*
1219 *Geophys.*, 27, 3155-3164, doi:10.5194/angeo-27-3155-2009, 2009.

1220 Amiridis, V., Wandinger, U., Marinou, E., Giannakaki, E., Tsekeri, A., Basart, S., Kazadzis, S.,
1221 Gkikas, A., Taylor, M., Baldasano, J. M., and Ansmann, A.: Optimizing CALIPSO Saharan dust
1222 retrievals, *Atmos. Chem. Phys.*, 13, 12089-12106, doi:10.5194/acp-13-12089-2013, 2013.

1223 Ångström, A.K.: On the atmospheric transmission of sun radiation and on the dust in the air, *Geogr.*
1224 *Ann.*, 12, 130-159, doi: 10.2307/519399, 1929.

1225 Balis, D., Amiridis, V., Kazadzis, S., Papayannis, A., Tsaknakis, G., Tzortzakis, S., Kalivitis, N.,
1226 Vrekoussis, M., Kanakidou, M., Mihalopoulos, N., Chourdakis, G., Nickovic, S., Pérez, C.,
1227 Baldasano, J. M., and Drakakis, M.: Optical characteristics of desert dust over the East Mediterranean
1228 during summer: a case study, *Ann. Geophys.*, 24, 807-821, doi:10.5194/angeo-24-807-2006, 2006.

1229 Balis, D.: Geometrical characteristics of desert dust layers over Thessaloniki estimated with
1230 backscatter/Raman lidar and the BSC/DREAM model, *Remote Sens. Lett.*, 353-362, doi:
1231 10.1080/01431161.2011.597793, 2012.

1232 Barkan, J., Alpert, P., Kutiel, H., and Kishcha, P.: Synoptics of dust transportation days from Africa
1233 toward Italy and central Europe, *J. Geophys. Res.*, 110, D07208, doi:10.1029/2004JD005222, 2005.

1234 Barnaba, F. and Gobbi, G. P.: Aerosol seasonal variability over the Mediterranean region and relative
1235 impact of maritime, continental and Saharan dust particles over the basin from MODIS data in the year
1236 2001, *Atmos. Chem. Phys.*, 4, 2367-2391, doi:10.5194/acp-4-2367-2004, 2004.

- 1237 Basart, S., Pérez, C., Cuevas, E., Baldasano, J. M., and Gobbi, G. P.: Aerosol characterization in
1238 Northern Africa, Northeastern Atlantic, Mediterranean Basin and Middle East from direct-sun
1239 AERONET observations, *Atmos. Chem. Phys.*, 9, 8265-8282, doi:10.5194/acp-9-8265-2009, 2009.
- 1240 Basart, S., Pay, M. T., Jorba, O., Pérez, C., Jiménez-Guerrero, P., Schulz, M., and Baldasano, J. M.:
1241 Aerosols in the CALIOPE air quality modelling system: evaluation and analysis of PM levels, optical
1242 depths and chemical composition over Europe, *Atmos. Chem. Phys.*, 12, 3363-3392, doi:10.5194/acp-
1243 12-3363-2012, 2012.
- 1244 Ben-Ami, Y., Koren, I., and Altaratz, O.: Patterns of North African dust transport over the Atlantic:
1245 winter vs. summer, based on CALIPSO first year data, *Atmos. Chem. Phys.*, 9, 7867–7875,
1246 doi:10.5194/acp-9-7867-2009, 2009.
- 1247 Ben-Ami, Y., Koren, I., Rudich, Y., Artaxo, P., Martin, S. T., and Andreae, M. O.: Transport of North
1248 African dust from the Bodélé depression to the Amazon Basin: a case study, *Atmos. Chem. Phys.*, 10,
1249 7533-7544, doi:10.5194/acp-10-7533-2010, 2010.
- 1250 Bègue, N., Tulet, P., Chaboureau, J. P., Roberts, G., Gomes, L., and Mallet, M.: Long-range transport
1251 of Saharan dust over north-western Europe during EUCAARI 2008 campaign: Evolution of dust
1252 optical properties by scavenging, *J. Geophys. Res.*, 117,D17201, doi:10.1029/2012JD017611, 2012.
- 1253 Berthier, S., Chazette, P., Couvert, P., Pelon, J., Dulac, F., Thieuleux, F., Moulin, C., and Pain, T.:
1254 Desert dust aerosol columnar properties over ocean and continental Africa from Lidar in-Space
1255 Technology Experiment (LITE) and Meteosat synergy. *J. Geophys. Res.*, 111, D21202,
1256 doi:10.1029/2005JD006999, 2006.
- 1257 Bollasina, M. A., Ming, Y., and Ramaswamy, V.: Anthropogenic Aerosols and the Weakening of the
1258 South Asian Summer Monsoon, *Science*, 334, 502–505, doi:10.1126/science.1204994, 2011.
- 1259 Bösenberg, J., Matthias, V., Amodeo, A., Amoiridis, V., Ansmann, A., Baldasano, J. M., Balin, I.,
1260 Balis, D., Böckmann, C., Boselli, A., Carlsson, G., Chaikovsky, A., Chourdakis, G., Comerón, A., De
1261 Tomasi, F., Eixmann, R., Freudenthaler, V., Giehl, H., Grigorov, I., Hågård, A., Iarlori, M., Kirsche,
1262 A., Kolarov, G., Komguem, L., Kreipl, S., Kumpf, W., Larchevêque, G., Linné, H., Matthey, R.,
1263 Mattis, I., Mekler, A., Mironova, I., Mitev, V., Mona, L., Müller, D., Music, S., Nickovic, S.,
1264 Pandolfi, M., Papayannis, A., Pappalardo, G., Pelon, J., Pérez, C., Perrone, R. M., Persson, R.,
1265 Resendes, D. P., Rizi, V., Rocadenbosch, F., Rodrigues, J. A., Sauvage, L., Schneidenbach, L.,
1266 Schumacher, R., Shcherbakov, V., Simeonov, V., Sobolewski, P., Spinelli, N., Stachlewska, I.,

1267 Stoyanov, D., Trickl, T., Tsaknakis, G., Vaughan, G., Wandinger, U., Wang, X., Wiegner, M.,
1268 Zavrtnik, M. and Zerefos, C.: A European aerosol research lidar network to establish an aerosol
1269 climatology, MPI-Rep. 317, Max-Planck Inst. für Meteorol., Hamburg, Germany, 2003.
1270 http://www.mpimet.mpg.de/fileadmin/publikationen/Reports/max_scirep_348.pdf
1271

1272 Burton, S. P., Ferrare, R. A., Vaughan, M. A., Omar, A. H., Rogers, R. R., Hostetler, C. A., and
1273 Hair, J. W.: Aerosol classification from airborne HSRL and comparisons with the CALIPSO vertical
1274 feature mask, *Atmos. Meas. Tech.*, 6, 1397-1412, doi:10.5194/amt-6-1397-2013, 2013.
1275

1276 Cachorro, V. E., Vergaz, R., de Frutos, A. M., Vilaplana, J. M., Henriques, D., Laulainen, N., and
1277 Toledano, C.: Study of desert dust events over the southwestern Iberian Peninsula in year 2000: two
1278 case studies, *Ann. Geophys.*, 24, 1493-1510, doi:10.5194/angeo-24-1493-2006, 2006.
1279

1280 Cao, C. X., Zheng, S., and Singh, R. P.: Characteristics of aerosol optical properties and meteorological
1281 parameters during three major dust events (2005–2010) over Beijing, China, *Atmos. Res.*, 150, 129–
1282 142, doi:10.1016/j.atmosres.2014.07.022, 2014.
1283

1284 Córdoba-Jabonero, C., Sorribas, M., Guerrero-Rascado, J. L., Adame, J. A., Hernández, Y.,
1285 Lyamani, H., Cachorro, V., Gil, M., Alados-Arboledas, L., Cuevas, E., and de la Morena, B.:
1286 Synergetic monitoring of Saharan dust plumes and potential impact on surface: a case study of dust
1287 transport from Canary Islands to Iberian Peninsula, *Atmos. Chem. Phys.*, 11, 3067-3091,
1288 doi:10.5194/acp-11-3067-2011, 2011.
1289

1290 Di Sarra, A., Di Iorio, T., Cacciani, M., Fiocco, G., and Fuà, D.: Saharan dust profiles measured by
1291 lidar at Lampedusa, *J. Geophys. Res.*, 106, 10 335–10 348, doi:10.1029/2000JD900734, 2001.
1292

1293 Díaz, J., Tobías A., and Linares, C.: Saharan dust and association between particulate matter and case-
1294 specific mortality: a case crossover analysis in Madrid (Spain), *Environ. Health*, doi:10.1186/1476-
1295 069X-11-11, 2012.
1296

1297 Draxler, R.R. and Rolph, G.D., 2015. HYSPLIT (HYbrid Single-Particle Lagrangian Integrated
1298 Trajectory) Model access via NOAA ARL READY Website (<http://ready.arl.noaa.gov/HYSPLIT.php>).
1299 NOAA Air Resources Laboratory, Silver Spring, MD.
1300

1301 Dubovik, O., Smirnov, A., Holben, B. N., King, M. D., Kaufman, Y. J., and Slutsker, I.: Accuracy
1302 assessments of aerosol optical properties retrieved from AERONET sun and sky radiance
1303 measurements, *J. Geophys. Res.*, 105, 9791–9806, doi: 10.1029/2000JD900040, 2000.
1304

1305 Dubovik, O. and King, M. D.: A flexible inversion algorithm for retrieval of aerosol optical properties
1306 from Sun and sky radiance measurements, *J. Geophys. Res.*, 105, 20673-20696, doi:
1307 10.1029/2000JD900282, 2000.
1308

1309 Dulac, F., Moulin, C., Lambert, C.E., Guillard, F., Poitou, J., Guelle, W., Quétel, C.R., Schneider, X.,
1310 Ezat, U., and Buat-Ménard, P.: Dry deposition of mineral aerosol particles in the atmosphere:
1311 Significance of the large size fraction, in *Precipitation Scavenging and Atmosphere-Surface Exchange*,
1312 edited by S. E. Schwartz and W.G. N. Slinn, pp. 841-854, Hemisphere. Richland, Wash., 1992.
1313

1314 Eck, T. F., Holben, B. N., Reid, J. S., Dubovik, O., Smirnov, A., O’Neill, N. T., Slutsker, I., and Kinne,
1315 S.: Wavelength dependence of optical depth of biomass burning, urban and desert dust aerosols, *J.*
1316 *Geophys. Res.*, 104, 31333–31350, doi: 10.1029/1999JD900923, 1999.
1317

1318 Eguchi, K., Uno, I., Yumimoto, K., Takemura, T., Shimizu, A., Sugimoto, N., and Liu, Z.: Trans-
1319 pacific dust transport: integrated analysis of NASA/CALIPSO and a global aerosol transport model,
1320 *Atmos. Chem. Phys.*, 9, 3137-3145, doi:10.5194/acp-9-3137-2009, 2009.
1321

1322 Escudero, M., Querol, X., Pey, J., Alastuey, A., Pérez, N., Ferreira, F., Alonso, S., Rodríguez, S., and
1323 Cuevas, E.: A methodology for the quantification of the net African dust load in air quality monitoring
1324 networks, *Atmos. Environ.*, 41, 5516–5524, doi:10.1016/j.atmosenv.2007.04.047, 2007.
1325

1326 Fotiadis, A., Hatzianastassiou, N., Drakakis, E., Matsoukas, C., Pavlakakis, K.G., Hatzidimitriou, D.,
1327 Gerasopoulos, E., Mihalopoulos, N., and Vardavas, I.: Aerosol physical and optical properties in the

1328 Eastern Mediterranean Basin, Crete, from Aerosol Robotic Network data, *Atmos. Chem. Phys.*, 6,
1329 5399–5413, doi:10.5194/acp-6-5399-2006, 2006.

1330

1331 Ginoux, P., Prospero, J. M., Gill, T. E., Hsu, N. C., and Zhao, M.: Global-scale attribution of
1332 anthropogenic and natural dust sources and their emission rates based on MODIS Deep Blue aerosol
1333 products, *Rev. Geophys.*, 50, RG3005, doi:10.1029/2012rg000388, 2012.

1334

1335 Gkikas, A., Hatzianastassiou, N., and Mihalopoulos, N.: Aerosol events in the broader Mediterranean
1336 basin based on 7-year (2000–2007) MODIS C005 data, *Ann. Geophys.*, 27, 3509-3522,
1337 doi:10.5194/angeo-27-3509-2009, 2009.

1338

1339 Gkikas, A., Hatzianastassiou, N., Mihalopoulos, N., Katsoulis, V., Kazadzis, S., Pey, J., Querol, X.,
1340 and Torres, O.: The regime of intense desert dust episodes in the Mediterranean based on contemporary
1341 satellite observations and ground measurements, *Atmos. Chem. Phys.*, 13, 12135-12154,
1342 doi:10.5194/acp-13-12135-2013, 2013.

1343 Gkikas, A., Houssos, E. E., Lolis, C. J., Bartzokas, A., Mihalopoulos, N. and Hatzianastassiou, N.:
1344 Atmospheric circulation evolution related to desert-dust episodes over the Mediterranean. *Q.J.R.*
1345 *Meteorol. Soc.*, 141: 1634–1645. doi: 10.1002/qj.2466, 2015.

1346 Gkikas, A., Hatzianastassiou, N., Mihalopoulos, N., Torres, O.: Characterization of aerosols episodes
1347 in the greater Mediterranean Sea area from satellite observations (2000 – 2007), *Atmos. Environ.*, 128,
1348 286 – 304, [doi:10.1016/j.atmosenv.2015.11.056](https://doi.org/10.1016/j.atmosenv.2015.11.056), 2016.

1349 Gobbi, G.P., Barnaba, F., Giorgi, R., Santacasa, A.: Altitude-resolved properties of a Saharan dust
1350 event over the Mediterranean, *Atmos. Environ.*, 34, 5119-5127, doi:10.1016/S1352-2310(00)00194-1,
1351 2000.

1352 Gobbi, G. P., Kaufman, Y. J., Koren, I., and Eck, T. F.: Classification of aerosol properties derived
1353 from AERONET direct sun data, *Atmos. Chem. Phys.*, 7, 453-458, doi:10.5194/acp-7-453-2007, 2007.

1354 Gobbi, G. P., Angelini, F., Barnaba, F., Costabile, F., Baldasano, J. M., Basart, S., Sozzi, R., and
1355 Bolignano, A.: Changes in particulate matter physical properties during Saharan advections over Rome
1356 (Italy): a four-year study, 2001–2004, *Atmos. Chem. Phys.*, 13, 7395–7404, doi:10.5194/acp-13-7395-
1357 2013, 2013.

1358 Hamonou, E., Chazette, P., Balis, D., Dulac, F., Schneider, X., Galani, E., Ancellet, G., and
1359 Papayannis, A.: Characterization of the vertical structure of Saharan dust export to the Mediterranean
1360 basin, *J. Geophys. Res.*, 104, 22 257–22 270, doi:10.1029/1999JD900257, 1999.

1361 Hara, Y., Yumimoto, K., Uno, I., Shimizu, A., Sugimoto, N., Liu, Z., and Winker, D. M.: Asian dust
1362 outflow in the PBL and free atmosphere retrieved by NASA CALIPSO and an assimilated dust
1363 transport model, *Atmos. Chem. Phys.*, 9, 1227-1239, doi:10.5194/acp-9-1227-2009, 2009.

1364 Hatzianastassiou, N., Gkikas, A., Mihalopoulos, N., Torres, O., and Katsoulis, B. D.: Natural versus
1365 anthropogenic aerosols in the eastern Mediterranean basin derived from multiyear TOMS and MODIS
1366 satellite data, *J. Geophys. Res.*, 114, D24202, doi:10.1029/2009JD011982, 2009.

1367 Heinold, B., Helmert, J., Hellmuth, O., Wolke, R., Ansmann, A., Marticorena, B., Laurent, B. and
1368 Tegen, I.: Regional modeling of Saharan dust events using LM-MUSCAT: Model description and case
1369 studies, *J. Geophys. Res.*, 112, D11204, doi:10.1029/2006JD007443, 2007.

1370 Heinold, B., Tegen, I., Schepanski, K., and Hellmuth, O.: Dust Radiative feedback on Saharan
1371 boundary layer dynamics and dust mobilization. *Geophys. Res. Lett.*, 35, L20817,
1372 doi:10.1029/2008GL035319, 2008.

1373 Herman, J. R., Bhartia, P. K., Torres, O., Hsu, N.C., Seftor, C. J., and Celarier E.: Global distribution of
1374 UV-absorbing aerosols from Nimbus-7/ TOMS data, *J. Geophys. Res.*, 102, 16911– 16923, doi:
1375 10.1029/96JD03680, 1997.

1376 Holben, B. N., Eck, T. F., Slutsker, I., Tanré, D., Buis, J. P., Setzer, A., Vermote, E., Reagan, J. A.,
1377 Kaufman, Y. J., Nakajima, T., Lavenu, F., Jankowiak, I., and Smirnov, A.: AERONET – A federated
1378 instrument network and data archive for aerosol characterization, *Remote Sens. Environ.*, 66, 1–16,
1379 doi:10.1016/S0034-4257(98)00031-5, 1998.

1380 Huang, J., Minnis, P., Lin, B., Wang, T., Yi, Y., Hu, Y., Sun-Mack, S. and Ayers, K.: Possible influences
1381 of Asian dust aerosols on cloud properties and radiative forcing observed from MODIS and CERES,
1382 *Geophys. Res. Lett.*, 33, L06824, doi:[10.1029/2005GL024724](https://doi.org/10.1029/2005GL024724), 2006.

1383 Huang, J., Zhang, C., and Prospero, J. M.: African dust outbreaks: a satellite perspective of temporal
1384 and spatial variability over the tropical Atlantic Ocean, *J. Geophys. Res.*, 115, D05202,
1385 doi:10.1029/2009JD012516, 2010.

1386 Hubanks, P. A., King, M. D., Platnick, S. A., and Pincus, R. A.: MODIS Atmosphere L3 Gridded
1387 Product Algorithm Theoretical Basis Document, MODIS Algorithm Theoretical Basis Document No.
1388 ATBD-MOD-30 for Level-3 Global Gridded Atmosphere Products (08 D3, 08 E3, 08M3), online:
1389 [http://modis-atmos.gsfc.nasa.gov/docs/L3 ATBD 2008 12 04.pdf](http://modis-atmos.gsfc.nasa.gov/docs/L3_ATBD_2008_12_04.pdf), 2008.

1390 Hunt, W. H, Winker, D. M., Vaughan, M. A., Powell, K. A., Lucker, P. L., and Weimer, C.: CALIPSO
1391 Lidar Description and Performance Assessment, *J. Atmos. Ocean. Technol.*, 26, 1214–1228,
1392 doi:10.1175/2009JTECHA1223.1, 2009.

1393 IPCC, 2013: Summary for Policymakers. In: *Climate Change 2013: The Physical Science Basis.*
1394 *Contribution of Working Group I to the Fifth Assessment Report of the Intergovernmental Panel on*
1395 *Climate Change* [Stocker, T.F., D. Qin, G.-K. Plattner, M. Tignor, S. K. Allen, J. Boschung, A. Nauels,
1396 Y. Xia, V. Bex and P.M. Midgley (eds.)]. Cambridge University Press, Cambridge, United Kingdom
1397 and New York, NY, USA.

1398 Kalivitis, N., Gerasopoulos, E., Vrekoussis, M., Kouvarakis, G., Kubilay, N., Hatzianastassiou, N.,
1399 Vardavas, I., and Mihalopoulos, N.: Dust transport over the eastern Mediterranean derived from
1400 TOMS, AERONET and surface measurements, *J. Geophys. Res.*, 112, D03202,
1401 doi:10.1029/2006JD007510, 2007.

1402 Karanasiou, A., Moreno, N., Moreno, T., Viana, M., de Leeuw, F., Querol, X.: Health effects from
1403 Sahara dust episodes in Europe: literature review and research gaps, *Environ. Int.*, 15, 107–
1404 114, doi:10.1016/j.envint.2012.06.012, 2012.

1405 Karyampudi, V. M., Palm, S. P., Reagen, J. A., Fang, H., Grant, W. B., Hoff, R. M., Moulin, C.,
1406 Pierce, H. F., Torres, O., Browell, E. V., and Melfi, S. H.: Validation of the Saharan dust plume
1407 conceptual model using lidar, *Meteosat and ECMWF*, *B. Am. Meteorol. Soc.*, 80, 1045–1075, doi:
1408 10.1175/1520-0477(1999)080<1045:VOTSDP>2.0.CO;2, 1999.

1409 Kaufman, Y. J., Tanré, D., Remer, L. A., Vermote, E. F., Chu, A., and Holben, B. N.: Operational
1410 remote sensing of tropospheric aerosol over land from EOS Moderate-resolution Imaging
1411 Spectroradiometer, *J. Geophys. Res.*, 102, 17051–17065, doi: 10.1029/96JD03988, 1997.

1412 Kaufman, Y. J., Smirnov, A., Holben, B. N., and Dubovik, O.: Baseline maritime aerosol: methodology
1413 to derive the optical thickness and the scattering properties, *Geophys. Res. Lett.*, 28, 3251– 3254, doi:
1414 10.1029/2001GL013312, 2001.

1415 Kaufman, Y. J., Tanre, D., Holben, B. N., Mattoo, S., Remer, L. A., Eck, T. F., Vaughan, J., and
1416 Chatenet, B.: Aerosol radiative impact on spectral solar flux at the surface, derived from principal-
1417 plane sky measurements, *J. Atmos. Sci.*, 59, 635–646, doi: 10.1175/1520-
1418 0469(2002)059<0635:AROSS>2.0.CO;2, 2002.

1419 Kazadzis, S., Bais, A., Amiridis, V., Balis, D., Meleti, C., Kouremeti, N., Zerefos, C. S.,
1420 Rapsomanikis, S., Petrakakis, M., Kelesis, A., Tzoumaka, P., and Kelektsoylou, K.: Nine years of UV
1421 aerosol optical depth measurements at Thessaloniki, Greece, *Atmos. Chem. Phys.*, 7, 2091-2101,
1422 doi:10.5194/acp-7-2091-2007, 2007.

1423 Kishcha, P., Barnaba, F., Gobbi, G. P., Alpert, P., Shtivelman, A., Krichak, S. O., and Joseph, J. H.:
1424 Vertical distribution of Saharan dust over Rome (Italy): Comparison between 3-year model predictions
1425 and lidar soundings, *J. Geophys. Res.*, 110, D06208, doi:10.1029/2004JD005480, 2005.

1426

1427 Klein, H., Nickovic, S., Haunold, W., Bundke, U., Nillius, B., Ebert, M., Weinbruch, S., Schuetz, L.,
1428 Levin, Z., Barrie, L. A., and Bingemer, H.: Saharan dust and ice nuclei over Central Europe, *Atmos.*
1429 *Chem. Phys.*, 10, 10211–10221, doi:10.5194/acp- 10-10211-2010, 2010.

1430

1431 Kubilay, N., Cokacar, T., and Oguz, T.: Optical properties of mineral dust outbreaks over the
1432 northeastern Mediterranean, *J. Geophys. Res.*, 108, 4666, doi:10.1029/2003JD003798, 2003.

1433 Lau, K. M., Kim, M. K., and Kim, K. M.: Asian summer monsoon anomalies induced by direct forcing:
1434 The role of the Tibetan plateau, *Clim. Dynam.*, 26, 855–864, doi: 10.1007/s00382-006-0114-z, 2006.

1435 Levy, R. C., Remer, L. A., Tanré, D., Kaufman, Y. J., Ichoku, C., Holben, B. N., Livingston, J. M.,
1436 Russell, P. B., and Maring, H.: Evaluation of the Moderate-Resolution Imaging Spectroradiometer
1437 (MODIS) retrievals of dust aerosol over the ocean during PRIDE, *J. Geophys. Res.*, 108, 8594,
1438 doi:10.1029/2002JD002460, 2003.

1439 Levy, R. C., Remer, L. A., Kleidman, R. G., Mattoo, S., Ichoku, C., Kahn, R., and Eck, T. F.: Global
1440 evaluation of the Collection 5 MODIS dark-target aerosol products over land, *Atmos. Chem. Phys.*, 10,
1441 10399–10420, doi:10.5194/acp-10-10399-2010, 2010.

1442 Liu, D., Wang, Z., Liu, Z., Winker, D., and Trepte, C.: A height resolved global view of dust aerosols
1443 from the first year CALIPSO lidar measurements, *J. Geophys. Res.*, 113, D16214,
1444 doi:10.1029/2007JD009776, 2008.

1445 Liu, Z., Vaughan, M., Winker, D., Kittaka, C., Getzewich, B., Kuehn, R., Omar, A., Powell, K., Trepte,
1446 C., and Hostetler, C.: The CALIPSO Lidar Cloud and Aerosol Discrimination: Version 2 Algorithm
1447 and Initial Assessment of Performance, *J. Atmos. Ocean. Technol.*, 26, 1198–1213,
1448 doi:10.1175/2009jtech1229.1, 2009.

1449 Luo, T., Wang, Z., Zhang, D., Liu, X., Wang, Y., and Yuan, R.: Global dust distribution from improved
1450 thin dust layer detection using A-train satellite lidar observations, *Geophys. Res. Lett.*, 42,
1451 doi:10.1002/2014GL062111, 2015.

1452 Lyamani, H., Olmo, F. J., and Alados-Arboledas, L.: Saharan dust outbreak over southeastern Spain as
1453 detected by sun photometer, *Atmos. Environ.*, 39, 7276–7284,
1454 doi:10.1016/j.atmosenv.2005.09.011, 2005.

1455 Mallet, M., Tulet, P., Serça, D., Solmon, F., Dubovik, O., Pelon, J., Pont, V., and Thouren, O.: Impact
1456 of dust aerosols on the radiative budget, surface heat fluxes, heating rate profiles and convective
1457 activity over West Africa during March 2006, *Atmos. Chem. Phys.*, 9, 7143-7160, doi:10.5194/acp-9-
1458 7143-2009, 2009.

1459 Mallet, M., Dubovik, O., Nabat, P., Dulac, F., Kahn, R., Sciare, J., Paronis, D., and Léon, J. F.:
1460 Absorption properties of Mediterranean aerosols obtained from multi-year ground-based remote
1461 sensing observations, *Atmos. Chem. Phys.*, 13, 9195-9210, doi:10.5194/acp-13-9195-2013, 2013.

1462 Marriotti, A., Struglia, M.V., Zeng, N., Lau, K.-M.: The Hydrological Cycle in the Mediterranean
1463 Region and Implications for the Water Budget of the Mediterranean Sea, *J. Clim.*, 15, 1674-1690, doi:
1464 10.1175/1520-0442(2002)015<1674:THCITM>2.0.CO;2, 2002.

1465 Matthias, V., Balis, D., Bösenberg, J., Eixmann, R., Iarlori, M., Komguem, L., Mattis, I., Papayannis,
1466 A., Pappalardo, G., Perrone, M. R., and Wang, X.: Vertical aerosol distribution over Europe: Statistical
1467 analysis of Raman lidar data from 10 European Aerosol Research Lidar Network (EARLINET)
1468 stations, *J. Geophys. Res.*, 109, D18201, doi:10.1029/2004JD004638, 2004.

1469 McGrath-Spangler, E. L. and Denning, A. S.: Global Seasonal Variations of Midday Planetary
1470 Boundary Layer Depth from CALIPSO Space-borne LIDAR, *J. Geophys. Res. Atmos.*, 118, 1226–
1471 1233, doi: 10.1002/jgrd.50198, 2013.

1472 Mehta, A. V. and Yang, S.: Precipitation climatology over Mediterranean Basin from ten years of
1473 TRMM measurements, *Adv. Geosci.*, 17, 87-91, doi:10.5194/adgeo-17-87-2008, 2008.

1474 Meloni, D., di Sarra, A., Biavati, G., DeLuisi, J. J., Monteleone, F., Pace, G., Piacentino, S., and
1475 Sferlazzo, D. M.: Seasonal behavior of Saharan dust events at the Mediterranean island of Lampedusa
1476 in the period 1999–2005, *Atmos. Environ.*, 41, 3041–3056, [doi:10.1016/j.atmosenv.2006.12.001](https://doi.org/10.1016/j.atmosenv.2006.12.001), 2007.
1477

1478 Meloni, D., di Sarra, A., Monteleone, F., Pace, G., Piacentino, S., and Sferlazzo, D. M.: Seasonal
1479 transport patterns of intense Saharan dust events at the Mediterranean island of Lampedusa, *Atmos.*
1480 *Res.*, 88, 134–148, [doi:10.1016/j.atmosres.2007.10.007](https://doi.org/10.1016/j.atmosres.2007.10.007), 2008.

1481 Middleton, N. J. and Goudie, A. S.: Saharan dust: sources and trajectories, *Trans. Inst. Br. Geogr.*, 26,
1482 165–181, [doi: 10.1111/1475-5661.00013](https://doi.org/10.1111/1475-5661.00013), 2001.

1483 Mielonen, T., Arola, A., Komppula, M., Kukkonen, J., Koskinen, J., de Leeuw, G., and Lehtinen, K. E.
1484 J.: Comparison of CALIOP level 2 aerosol subtypes to aerosol types derived from AERONET
1485 inversion data, *Geophys. Res. Lett.*, 36, L18804, [doi:10.1029/2009gl039609](https://doi.org/10.1029/2009gl039609), 2009.

1486 Mona, L., Amodeo, A., Pandolfi, M. and Pappalardo, G.: Saharan dust intrusions in the Mediterranean
1487 area: Three years of Raman lidar measurements, *J. Geophys. Res.*, 111, D16203,
1488 [doi:10.1029/2005JD006569](https://doi.org/10.1029/2005JD006569), 2006.

1489 Mona, L., Liu, Z., Müller, D., Omar, A., Papayannis, A., Pappalardo, G., Sugimoto, N., and
1490 Vaughan, M.: Lidar Measurements for Desert Dust Characterization: An Overview, *Adv. Meteorol.*,
1491 2012, 356265, [doi:10.1155/2012/356265](https://doi.org/10.1155/2012/356265), 2012.

1492 Mona, L., Papagiannopoulos, N., Basart, S., Baldasano, J. M., Biniotoglou, I., Cornacchia, C., and
1493 Pappalardo, G.: EARLINET dust observations vs. BSC-DREAM8b modeled profiles: 12-year-long
1494 systematic comparison at Potenza, Italy, *Atmos. Chem. Phys.*, 14, 8781-8793, [doi:10.5194/acp-14-](https://doi.org/10.5194/acp-14-8781-2014)
1495 [8781-2014](https://doi.org/10.5194/acp-14-8781-2014), 2014.

1496 Moulin, C., Lambert, C. E., Dulac, F., and Dayan, U.: Control of atmospheric export of dust from
1497 North Africa by the North Atlantic Oscillation, *Nature*, 387, 691–694, 1997.

1498 Moulin, C., Lambert, C., Dayan, U., Masson, V., Ramonet, M., Bousquet, P., Legrand, M., Balkanski,
1499 Y., Guelle, W., Marticorena, B., Bergametti, G., and Dulac, F.: Satellite climatology of African dust
1500 transport in the Mediterranean atmosphere, *J. Geophys. Res.*, 103, 13137–13144, [doi:](https://doi.org/10.1029/98JD00171)
1501 [10.1029/98JD00171](https://doi.org/10.1029/98JD00171), 1998.

1502 Nabat, P., Somot, S., Mallet, M., Chiapello, I., Morcrette, J. J., Solmon, F., Szopa, S., Dulac, F.,
1503 Collins, W., Ghan, S., Horowitz, L. W., Lamarque, J. F., Lee, Y. H., Naik, V., Nagashima, T., Shindell,
1504 D., and Skeie, R.: A 4-D climatology (1979–2009) of the monthly tropospheric aerosol optical depth
1505 distribution over the Mediterranean region from a comparative evaluation and blending of remote
1506 sensing and model products, *Atmos. Meas. Tech.*, 6, 1287–1314, doi:10.5194/amt-6-1287-2013, 2013.

1507 Nowottnick, E. P., Colarco, P. R., Welton, E. J., and da Silva, A.: Use of the CALIOP vertical feature
1508 mask for evaluating global aerosol models, *Atmos. Meas. Tech.*, 8, 3647–3669, doi:10.5194/amt-8-
1509 3647-2015, 2015.

1510 Omar, A. H., Winker, D. M., Kittaka, C., Vaughan, M. A., Liu, Z. Y., Hu, Y. X., Treppe, C. R., 20
1511 Rogers, R. R., Ferrare, R. A., Lee, K. P., Kuehn, R. E., and Hostetler, C. A.: The CALIPSO automated
1512 aerosol classification and lidar ratio selection algorithm, *J. Atmos. Ocean. Technol.*, 26, 1994–2014,
1513 doi:10.1175/2009jtech1231.1, 2009.

1514 O’Neill, N. T., Eck, T. F., Smirnov, A., Holben, B. N., and Thulasiraman, S.: Spectral discrimination of
1515 coarse and fine mode optical depth, *J. Geophys. Res.-Atmos.*, 108, 4559, doi:10.1029/2002JD002975,
1516 2003.

1517 Pace, G., di Sarra, A., Meloni, D., Piacentino, S., and Chamard, P.: Aerosol optical properties at
1518 Lampedusa (Central Mediterranean). 1. Influence of transport and identification of different aerosol
1519 types, *Atmos. Chem. Phys.*, 6, 697–713, doi:10.5194/acp-6-697-2006, 2006.

1520 Papadimas, C. D., Hatzianastassiou, N., Mihalopoulos, N., Querol, X., and Vardavas, I.: Spatial and
1521 temporal variability in aerosol properties over the Mediterranean basin based on 6-year (2000–2006)
1522 MODIS data, *J. Geophys. Res.*, 113, D11205, doi:10.1029/2007JD009189, 2008.

1523 Papadimas, C. D., Hatzianastassiou, N., Mihalopoulos, N., Kanakidou, M., Katsoulis, B. D., and
1524 Vardavas, I.: Assessment of the MODIS Collections C005 and C004 aerosol optical depth products
1525 over the Mediterranean basin, *Atmos. Chem. Phys.*, 9, 2987– 2999, doi:10.5194/acp-9-2987-2009,
1526 2009.

1527 Papayannis, A., Balis, D., Amiridis, V., Chourdakis, G., Tsaknakis, G., Zerefos, C., Castanho, A.D.A.,
1528 Nickovic, S., Kazadzis, S., and Grabowski, J.: Measurements of Saharan dust aerosols over the Eastern
1529 Mediterranean using elastic backscatter-Raman lidar, spectrophotometric and satellite observations in
1530 the frame of the EARLINET project, *Atmos. Chem. Phys.*, 5, 2065–2079, doi:10.5194/acp-5-2065-
1531 2005, 2005.

1532 Papayannis, A., Amiridis, V., Mona, L., Tsaknakis, G., Balis, D., Bösenberg, J., Chaikovski, A., De
1533 Tomasi, F., Grigorov, I., Mattis, I., Mitev, V., Müller, D., Nickovic, S., Pérez, C., Pietruczuk, A.,
1534 Pisani, G., Ravetta, F., Rizi, V., Sicard, M., Trickl, T., Wiegner, M., Gerding, M., Mamouri, R. E.,
1535 D'Amico, G., and Pappalardo, G.: Systematic lidar observations of Saharan dust over Europe in the
1536 frame of EARLINET (2000–2002), *J. Geophys. Res.*, 113, D10204, doi:10.1029/2007JD009028, 2008.

1537 Papayannis, A., Mamouri, R. E., Amiridis, V., Kazadzis, S., Pérez, C., Tsaknakis, G., Kokkalis, P., and
1538 Baldasano, J. M.: Systematic lidar observations of Saharan dust layers over Athens, Greece in the
1539 frame of EARLINET project (2004–2006), *Ann. Geophys.*, 27, 3611–3620, doi:10.5194/angeo-27-
1540 3611-2009, 2009.

1541 Papayannis, A., Nicolae, D., Kokkalis, P., Biniotoglou, I., Talianu, C., Belegante, L., Tsaknakis, G.,
1542 Cazacu, M.M., Vetres, I., Ilic, L.: Optical, size and mass properties of mixed type aerosols in Greece
1543 and Romania as observed by synergy of lidar and sunphotometers in combination with model
1544 simulations: A case study, *Sci. Total Environ.*, Volumes: 500-501, 277–294,
1545 doi:10.1016/j.scitotenv.2014.08.101, 2014.

1546 Pereira, S. N., Wagner, F., and Silva, A. M.: Seven years of measurements of aerosol scattering
1547 properties, near the surface, in the southwestern Iberia Peninsula, *Atmos. Chem. Phys.*, 11, 17–29,
1548 doi:10.5194/acp-11-17-2011, 2011.

1549 Pérez, C., Nickovic, S., Pejanovic, G., Baldasano, J.M. and Özsoy, E.: Interactive dust-radiation
1550 modeling: A step to improve weather forecasts, *J. Geophys. Res.*, 111, D16206,
1551 doi:10.1029/2005JD006717, 2006.

1552 Pérez García-Pando, C., Stanton, M. C., Diggle, P. J., Trzaska, S., Miller, R. L., Perlwitz, J. P.,
1553 Baldasano, J. M., Cuevas, E., Ceccato, P., Yaka, P., and Thomson, M. C.: Soil Dust Aerosols and Wind
1554 as Predictors of Seasonal Meningitis Incidence in Niger, *Environ. Health Perspect.*, 122, 679–686,
1555 doi:10.1289/ehp.1306640, 2014.

1556 Pey, J., Querol, X., Alastuey, A., Forastiere, F., and Stafoggia, M.: African dust outbreaks over the
1557 Mediterranean Basin during 2001–2011: PM10 concentrations, phenomenology and trends, and its
1558 relation with synoptic and mesoscale meteorology, *Atmos. Chem. Phys.*, 13, 1395–1410, doi:
1559 10.5194/acp-13-1395-2013, 2013.

1560 Pisani, G., Boselli, A., Spinelli, N., Wang, X.: Characterization of Saharan dust layers over Naples
1561 (Italy) during 2000–2003 EARLINET project, *Atmos. Res.* 102, 286 – 299,
1562 doi:10.1016/j.atmosres.2011.07.012, 2011.

1563 Prospero, M. J., Ginoux, P., Torres, O., Nicholson, S. E., and Gill, T. E.: Environmental
1564 characterization of global sources of atmospheric soil dust identified with the Nimbus 7 Total Ozone
1565 Mapping Spectrometer (TOMS) absorbing aerosol product, *Rev. Geophys.*, 40, 1002,
1566 doi:10.1029/2000RG000095, 2002.

1567 Prospero, J. M. and Lamb, P. J.: African droughts and dust transport to the Caribbean: climate change
1568 implications, *Science*, 302, 1024–1027, doi:10.1126/science.1089915, 2003.

1569 Querol, X., Alastuey A., Lopez-Soler A., Plana F. Puigercus J.A, Mantilla E., Miro J.V.; Artiñano B.:
1570 Seasonal evolution of atmospheric suspended particles around a coal-fired power station: Particulate
1571 levels and sources, *Atmos. Environ.*, 32, 11, 1963–1978, doi: 10.1016/S1352-2310(97)00504-9, 1998.

1572 Querol, X., Alastuey, A., Pey, J., Cusack, M., Pérez, N., Mihalopoulos, N., Theodosi, C.,
1573 Gerasopoulos, E., Kubilay, N., and Koçak, M.: Variability in regional background aerosols within the
1574 Mediterranean, *Atmos. Chem. Phys.*, 9, 4575–4591, doi:10.5194/acp-9-4575-2009, 2009a.

1575 Querol, X., Pey, J., Pandolfi, M., Alastuey, A., Cusack, M., Pérez, N., Moreno, T., Viana, N.,
1576 Mihalopoulos, N., Kallos, G. and Kleanthous, S.: African dust contributions to mean ambient PM10
1577 mass-levels across the Mediterranean basin, *Atmos. Environ.*, 43, 4266–4277,
1578 doi:10.1016/j.atmosenv.2009.06.013, 2009b.

1579 Redemann, J., Vaughan, M. A., Zhang, Q., Shinozuka, Y., Russell, P. B., Livingston, J. M.,
1580 Kacenelenbogen, M., and Remer, L. A.: The comparison of MODIS-Aqua (C5) and CALIOP (V2 &
1581 V3) aerosol optical depth, *Atmos. Chem. Phys.*, 12, 3025–3043, doi:10.5194/acp-12-3025-2012, 2012.

1582 Remer, L. A., Tanré, D., Kaufman, Y. J., Ichoku, C., Mattoo, S., Levy, R., Chu, D. A., Holben, B.,
1583 Dubovik, O., Smirnov, A., Martins, J. V., Li, R.-R., and Ahman, Z.: Validation of MODIS aerosol
1584 retrieval over ocean, *Geophys. Res. Lett.*, 29, 8008, doi:10.1029/2001GL013204, 2002.

1585 Remer, L. A., Kaufman, Y. J., Tanré, D., Mattoo, S., Chu, D. A., Martins, J. V., Li, R. R., Ichoku, C.,
1586 Levy, R. C., Kleidman, R. G., Eck, T. F., Vermote, E., and Holben, B. N.: The MODIS aerosol
1587 algorithm, products and validation, *J. Atmos. Sci.*, 62, 947–973,
1588 doi: <http://dx.doi.org/10.1175/JAS3385.1>, 2005.

1589 Remer, L. A., Kleidman, R. G., Levy, R. C., Kaufman, Y. J., Tanré, D., Mattoo, S., Martins, J. V.,
1590 Ichoku, C., Koren, I., Yu, H., and Holben, B. N.: Global aerosol climatology from the MODIS satellite
1591 sensors, *J. Geophys. Res.*, 113, D14S07, doi:10.1029/2007JD009661, 2008.

1592 Rodríguez, S., Querol, X., Alastuey, A., Kallos, G., Kakaliagou, O.: Saharan dust contributions to
1593 PM10 and TSP levels in Southern and Eastern Spain, *Atmos. Environ.*, 35, 2433–2447,
1594 doi:10.1016/S1352-2310(00)00496-9, 2001.

1595 Salvador, P., Alonso-Pérez, S., Pey, J., Artíñano, B., de Bustos, J. J., Alastuey, A., and Querol, X.:
1596 African dust outbreaks over the western Mediterranean Basin: 11-year characterization of atmospheric
1597 circulation patterns and dust source areas, *Atmos. Chem. Phys.*, 14, 6759-6775, doi:10.5194/acp-14-
1598 6759-2014, 2014.

1599 Schepanski, K., Tegen, I., Todd, M. C., Heinold, B., Bönisch, G., Laurent, B., and Macke, A.:
1600 Meteorological processes forcing Saharan dust emission inferred from MSG-SEVIRI observations of
1601 subdaily dust source activation and numerical models, *J. Geophys. Res.*, 114, D10201,
1602 doi:10.1029/2008jd010325, 2009.

1603 Schuster, G. L., Vaughan, M., MacDonnell, D., Su, W., Winker, D., Dubovik, O., Lapyonok, T., and
1604 Trepte, C.: Comparison of CALIPSO aerosol optical depth retrievals to AERONET measurements, and
1605 a climatology for the lidar ratio of dust, *Atmos. Chem. Phys.*, 12, 7431-7452, doi:10.5194/acp-12-
1606 7431-2012, 2012.

1607 Smirnov, A., Holben, B. N., Eck, T. F., Dubovik, O. and Slutsker, I.: Cloud screening and quality
1608 control algorithms for the AERONET database, *Remote Sens. Environ.*, 73, 337–349,
1609 doi:10.1016/S0034-4257(00)00109-7, 2000.

1610 Solmon, F., Mallet, M., Elguindi, N., Giorgi, F., Zakey, A. and Konaré, A.: Dust aerosol impact on
1611 regional precipitation over western Africa, mechanisms and sensitivity to absorption properties,
1612 *Geophys. Res. Lett.*, 35, L24705, doi:10.1029/2008GL035900, 2008.

1613 Stephens, G. L., Vane, D. G., Boain, R. J., Mace, G. G., Sassen, K., Wang, Z., Illingworth, A. J.,
1614 O’Conner, E. J., Rossow, W. G., Durden, S. L., Miller, S. D., Austin, R. T., Benedetti, A., and
1615 Mitrescu, C.: The CloudSat mission and the A-Train, *Bull. Amer. Meteorol. Soc.*, 83, 1771–1790, doi:
1616 10.1175/BAMS-83-12-1771, 2002.

1617 Tafuro, A.M., Barnaba, F., De Tomassi, F., Perrone, M.R., Gobbi, G.P.: Saharan dust particle
1618 properties over the Central Mediterranean, *Atmos. Res.*, 81, 67-93,
1619 [doi:10.1016/j.atmosres.2005.11.008](https://doi.org/10.1016/j.atmosres.2005.11.008), 2006.

1620 Tanré, D., Kaufman, Y. J., Herman, M., and Mattoo, S.: Remote sensing of aerosol properties over
1621 oceans using the MODIS/EOS spectral radiances, *J. Geophys. Res.*, 102, 16971–16988, doi:
1622 10.1029/96JD03437, 1997.

1623 Tegen, I.: Modelling the mineral dust aerosol cycle in the climate system, *Quat. Sci. Rev.*, 22, 1821–
1624 1834, doi:10.1016/S0277-3791(03)00163-X, 2003.

1625 Toledano, C., Cachorro, V. E., de Frutos, A. M. Sorribas, M., Prats, N., and de la Morena, B. A.:
1626 Inventory of African desert dust events over the southwestern Iberian Peninsula in 2000–2005 with an
1627 AERONET Cimel Sun Photometer, *J. Geophys. Res.*, 112, D21201, doi:10.1029/2006JD008307,
1628 2007a.

1629

1630 Toledano, C., Cachorro, V.E., Sorribas, M., Berjón, A., de la Morena, B.A., de Frutos, A.M. and
1631 Gouloub, P.: Aerosol optical depth and Ångström exponent climatology at El Arenosillo AERONET
1632 site (Huelva, Spain), *Q. J. R. Meteorol. Soc.*, 133, 795–807, doi:10.1002/qj.54, 2007b.

1633

1634 Torres, O., Bhartia, P.K., Herman, J.R., Ahmad, Z. and Gleason, J.: Derivation of aerosol properties
1635 from a satellite measurements of backscattered ultraviolet radiation: Theoretical basis, *J. Geophys.*
1636 *Res.*, 103, 17099–17110, doi: 10.1029/98JD00900, 1998.

1637

1638 Torres, O., Bhartia, P. K., Herman, J. R., Sinyuk A., Holben, B.: A long term record of aerosol optical
1639 thickness from TOMS observations and comparison to AERONET measurements, *J. Atmos. Sci.*,
1640 59398-413, doi: 10.1175/1520-0469(2002)059<0398:ALTROA>2.0.CO;2, 2002.

1641

1642 Torres, O., Bhartia, P.K., Sinyuk, A., Welton, E.J., and Holben, D.: Total Ozone Mapping
1643 Spectrometer measurements of aerosol absorption from space: Comparison to SAFARI 2000 ground-
1644 based observations, *J. Geophys. Res.*, 110, D10S18, doi:10.1029/2004JD004611, 2005.

1645

1646 Torres, O., A. Tanskanen, B. Veihelman, C. Ahn, R. Braak, P. K. Bhartia, P. Veefkind, and P. Levelt,
1647 Aerosols and Surface UV Products from OMI Observations: An Overview, *J. Geophys. Res.*, 112,
1648 D24S47, doi:10.1029/2007JD008809, 2007.

1649

1650 Trigo, I. F., Bigg, G. R., and Davies, T. D.: Climatology of cyclogenesis in the Mediterranean, *Mon.*
1651 *Weather Rev.*, 130, 549–569, doi: 10.1175/1520-0493(2002)130<0549:COCMIT>2.0.CO;2, 2002.

1652 Tsamalis, C., Chédin, A., Pelon, J., and Capelle, V.: The seasonal vertical distribution of the Saharan
1653 Air Layer and its modulation by the wind, *Atmos. Chem. Phys.*, 13, 11235-11257, doi:10.5194/acp-13-
1654 11235-2013, 2013.

1655 Varga, G., Újvári, G., Kovács, J.: Spatiotemporal patterns of Saharan dust outbreaks in the
1656 Mediterranean Basin, *Aeolian Res.*, Vol. 15, 151-160, [doi:10.1016/j.aeolia.2014.06.005](https://doi.org/10.1016/j.aeolia.2014.06.005), 2014.

1657 Vaughan, M. A., Powell, K. A., Kuehn, R. E., Young, S. A., Winker, D. M., Hostetler, C. A., Hunt, W.
1658 H., Liu, Z. Y., McGill, M. J., and Getzewich, B. J.: Fully automated detection of cloud and aerosol
1659 layers in the CALIPSO lidar measurements, *J. Atmos. Ocean. Tech.*, 26, 2034–2050,
1660 doi:10.1175/2009jtecha1228.1, 2009.

1661 Winker, D., Vaughan, M., Omar, A., Hu, Y., Powell, K., Liu, Z., Hunt, W., and Young, S.: Overview
1662 of the CALIPSO mission and CALIOP data processing algorithm, *J. Atmos. Ocean. Technol.*, 26,
1663 2310–2323, doi: <http://dx.doi.org/10.1175/2009JTECHA1281.1>, 2009.

1664 Winker, D. M., Tackett, J. L., Getzewich, B. J., Liu, Z., Vaughan, M. A., and Rogers, R. R.: The global
1665 3-D distribution of tropospheric aerosols as characterized by CALIOP, *Atmos. Chem. Phys.*, 13, 3345-
1666 3361, doi:10.5194/acp-13-3345-2013, 2013.

1667 Yoon, J., von Hoyningen-Huene, W., Kokhanovsky, A. A., Vountas, M., and Burrows, J. P.: Trend
1668 analysis of aerosol optical thickness and Ångström exponent derived from the global AERONET
1669 spectral observations, *Atmos. Meas. Tech.*, 5, 1271-1299, doi:10.5194/amt-5-1271-2012, 2012.

1670 Zhang, J. L., Reid, J. S., and Holben, B. N.: An analysis of potential cloud artifacts in MODIS over
1671 ocean aerosol optical thickness products, *Geophys. Res. Lett.*, 32, L15803,
1672 doi:10.1029/2005GL023254, 2005.

1673 Zhang, L., Li, Q. B., Gu, Y., Liou, K. N., and Meland, B.: Dust vertical profile impact on global
1674 radiative forcing estimation using a coupled chemical-transport–radiative-transfer model, *Atmos.*
1675 *Chem. Phys.*, 13, 7097-7114, doi:10.5194/acp-13-7097-2013, 2013.

1676

1677

1678

1679

1680

1681

1682

1683

1684

1685

1686

1687

1688

1689

1690

1691

1692

1693

1694

1695

1696 **Table 1:** AERONET stations, depicted with cyan colors in Figure 1, which have been used for the identification of desert
 1697 dust (*DD*) episodes based on ground retrievals.

Stations	Latitude	Longitude	Study period
Blida	N 36° 30' 28"	E 02° 52' 51"	7 Nov. 2003 – 18 Feb. 2012
El Arenosillo	N 37° 06' 18"	W 06° 43' 58"	1 Mar. 2000 – 21 Feb. 2010
Evora	N 38° 34' 04"	W 07° 54' 43"	4 Jul. 2003 – 28 Feb. 2013
FORTH CRETE	N 35° 19' 58"	E 25° 16' 55"	23 Jan. 2003 – 6 Aug. 2011
IMC Oristano	N 39° 54' 36"	E 08° 30' 00"	30 May 2000 – 28 Feb. 2003
IMS METU Erdemli	N 36° 33' 54"	E 34° 15' 18"	1 Mar. 2000 – 28 Feb. 2013
Nes Ziona	N 31° 55' 19"	E 34° 47' 20"	1 Feb. 2000 – 28 Feb. 2013

1698

1699 **Table 2:** Percentages of the satellite Ångström exponent, Fine fraction, Effective Radius and Aerosol Index retrievals
 1700 satisfying the defined thresholds in the satellite algorithm for the identification of desert dust episodes.

Parameter	Valid	Invalid	Number of <i>DD</i> episodes
Ångström exponent	97.8%	2.2%	232
Fine fraction	98.7%	1.3%	232
Effective radius	94.5%	5.5%	117
Aerosol Index	86.9%	13.1%	206

1701

1702

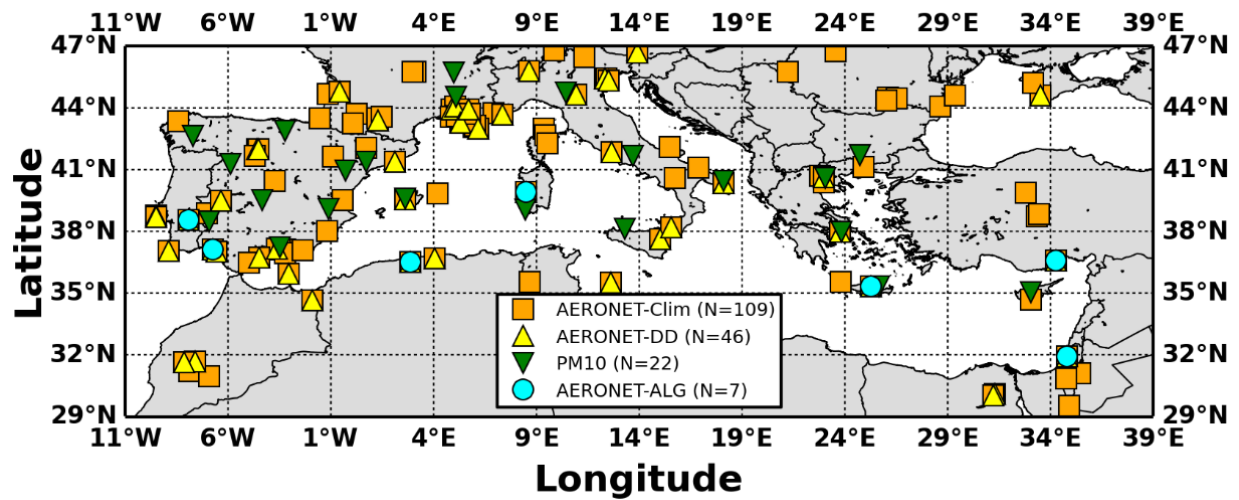
1703

1704

1705

1706

1707



1708

1709 **Figure 1:** Locations of the AERONET and PM_{10} stations which have been used for the evaluation of the algorithm's
 1710 outputs. More specifically, with orange squares are denoted the AERONET stations located into the study region, with the
 1711 yellow triangles the AERONET stations with coincident satellite and ground retrievals under dust episodes conditions, with
 1712 the cyan circles the AERONET stations which have been used for the evaluation of the defined algorithm thresholds and
 1713 with the green triangles are depicted the PM_{10} stations.

1714

1715

1716

1717

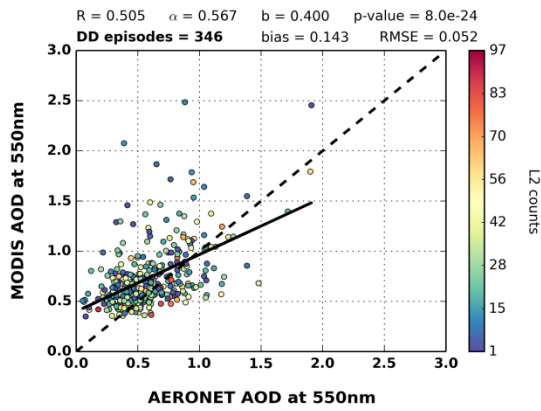
1718

1719

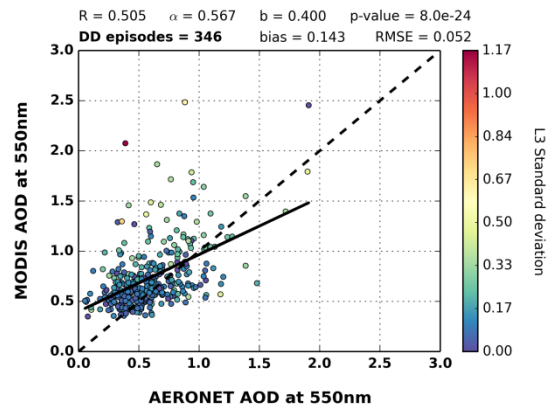
1720

1721

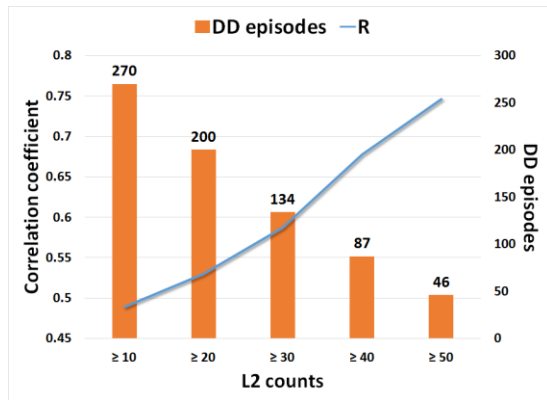
1722



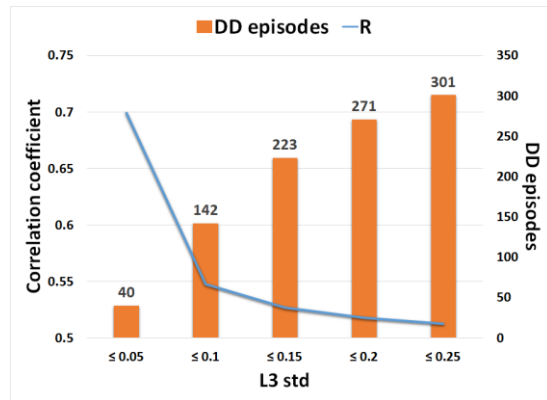
(i-a)



(i-b)



(ii-a)



(ii-b)

1723 **Figure 2:** (i) Scatterplots between MODIS-Terra and AERONET aerosol optical depths at 550 nm under intense desert dust
 1724 episodes conditions related to the: (a) number of level 2 counts which are used for the calculation of the level 3 retrievals
 1725 and (b) spatial standard deviation inside the 1° x 1° grid cells (level 3 retrievals). (ii) Sensitivity analysis for the calculated
 1726 correlation coefficients between satellite and ground AODs, depending on the: (a) number of level 2 retrievals and (b) sub-
 1727 grid standard deviation of level 3 retrievals.

1728

1729

1730

1731

1732

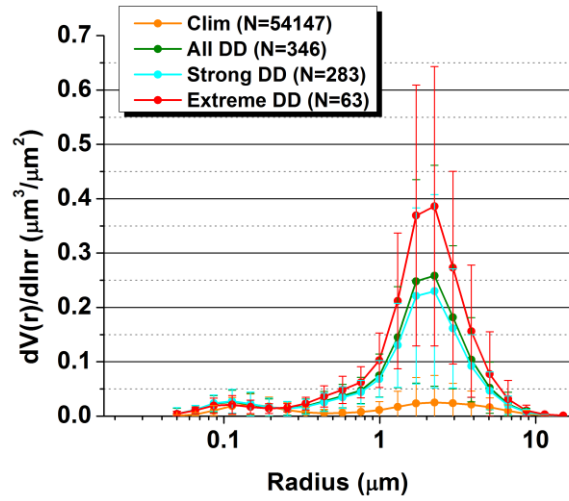
1733

1734

1735

1736

1737



1738

1739 **Figure 3:** AERONET size distributions averaged for all available retrievals (orange curve) as well as for the total (green
 1740 curve), strong (cyan curve) and extreme (red curve) desert dust episodes, occurred over the broader area of the
 1741 Mediterranean basin, during the period Mar. 2000 – Feb. 2013. The error bars represent the calculated standard deviations.

1742

1743

1744

1745

1746

1747

1748

1749

1750

1751

1752

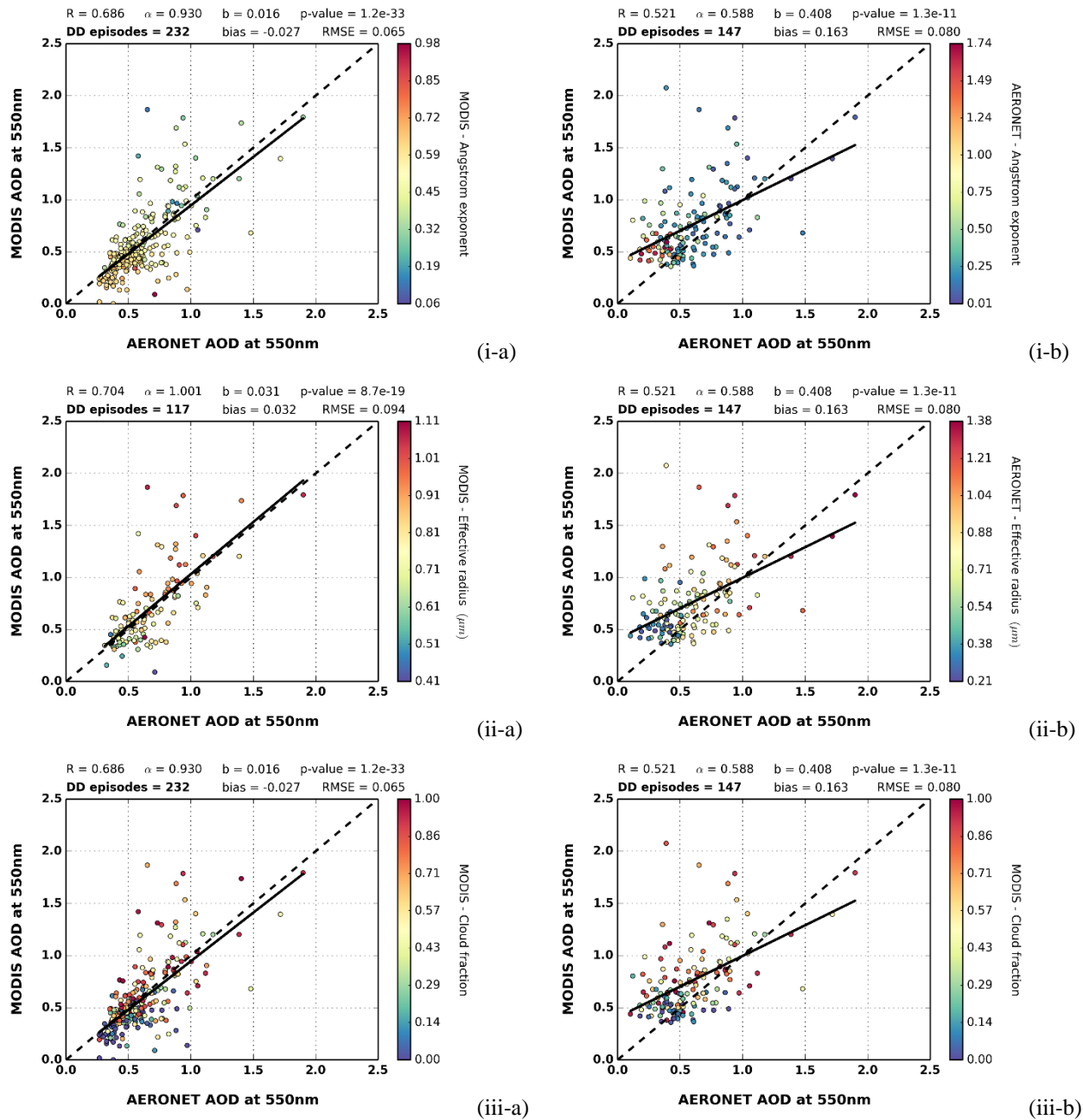
1753

1754

1755

1756

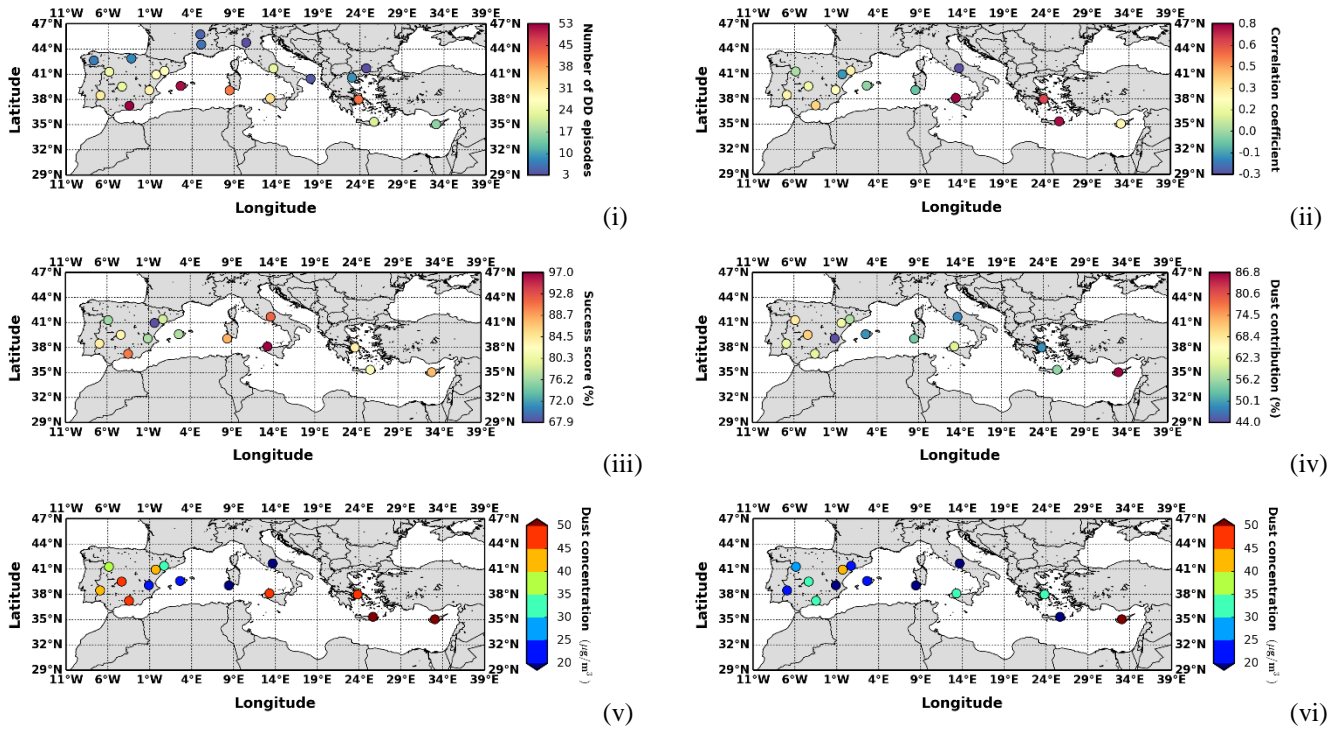
1757



1758 **Figure 4:** Scatterplots of MODIS-Terra and AERONET aerosol optical depths at 550 nm when intense dust episodes have
 1759 been identified based on: (a) AERONET retrievals and (b) satellite algorithm, respectively. In the left column, colormaps
 1760 indicate the corresponding values of: (i) Ångström exponent, (ii) Effective radius and (iii) Day cloud fraction derived by
 1761 MODIS-Terra retrievals. In the right column, colormaps indicate the corresponding values of: (i) AERONET Ångström
 1762 exponent, (ii) AERONET Effective radius and (iii) MODIS day cloud fraction retrievals. For each scatterplot, are provided
 1763 the correlation coefficient (R), slope (α), intercept (b), p-value, number of DD episodes, bias (MODIS – AERONET) and
 1764 root mean square error ($RMSE$).

1765

1766



1767 **Figure 5:** (i) Number of concurrent intense *DD* episodes where total PM_{10} concentrations and MODIS-Terra *AOD* retrievals
 1768 are available, (ii) Computed correlation coefficient values between total PM_{10} concentrations and MODIS-Terra *AOD*
 1769 retrievals in stations where at least 10 *DD* episodes have been recorded, (iii) Percentage of intense *DD* episodes where dust
 1770 particles have been identified by the ground stations, (iv) Dust contribution percentages (%) to the total PM_{10}
 1771 concentrations, (v) Calculated mean and (vi) median dust concentrations ($\mu\text{g m}^{-3}$), based on ground measurements for the
 1772 identified intense *DD* episodes by the satellite algorithm.

1773

1774

1775

1776

1777

1778

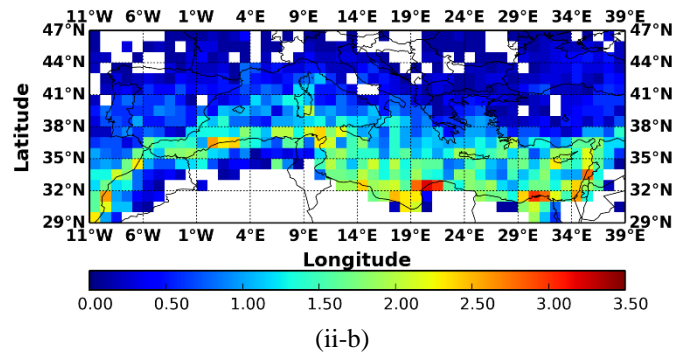
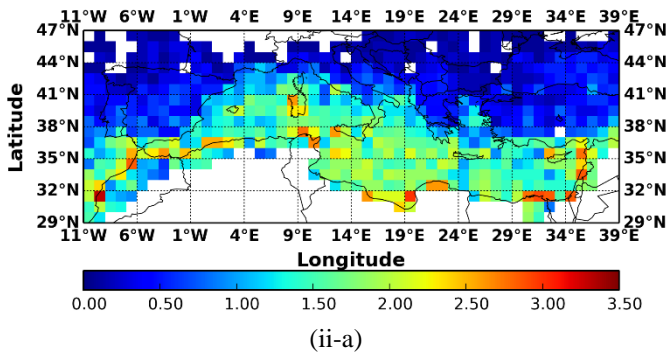
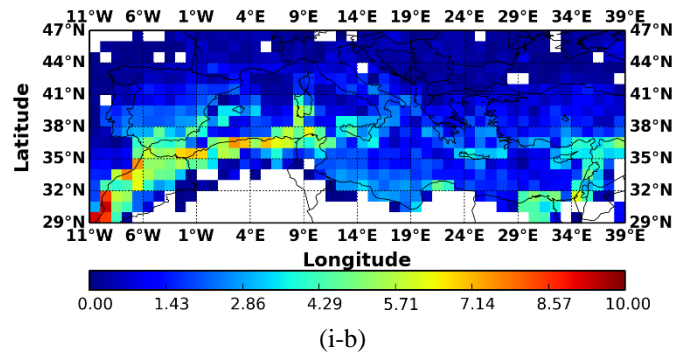
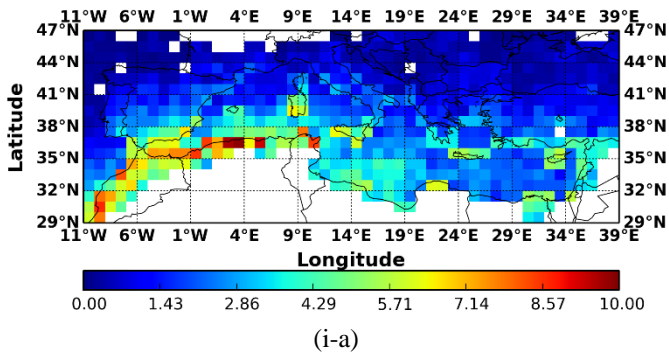
1779

1780

1781

1782

1783



1784 **Figure 6:** Geographical distributions of the occurrence frequency (episodes yr⁻¹) of: (i) strong and (ii) extreme desert dust
 1785 episodes, averaged for the periods: (a) Mar. 2000 – Feb. 2013 (MODIS-Terra) and (b) 2003 – 2012 (MODIS-Aqua), over
 1786 the broader area of the Mediterranean basin.

1787

1788

1789

1790

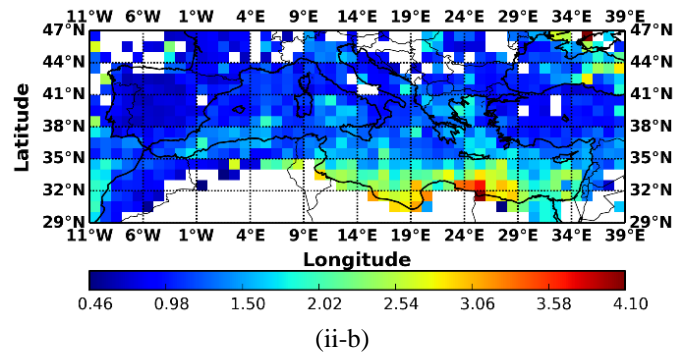
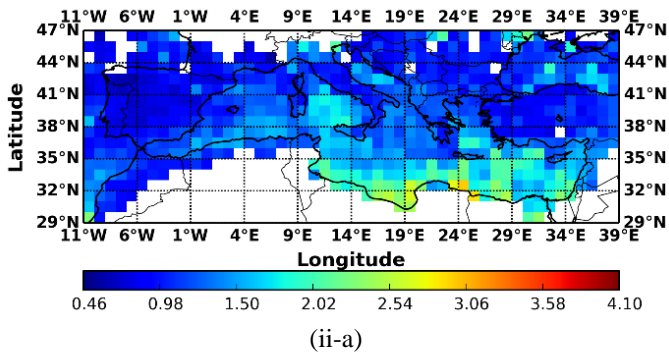
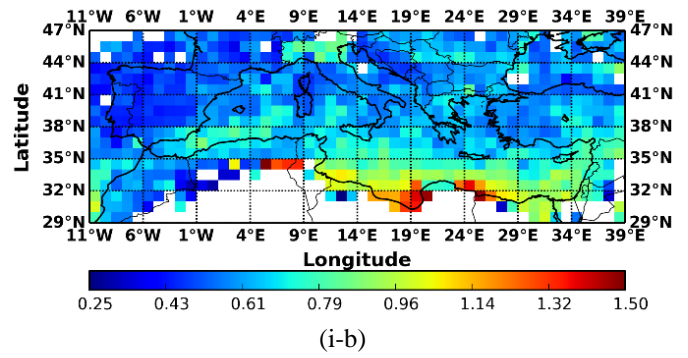
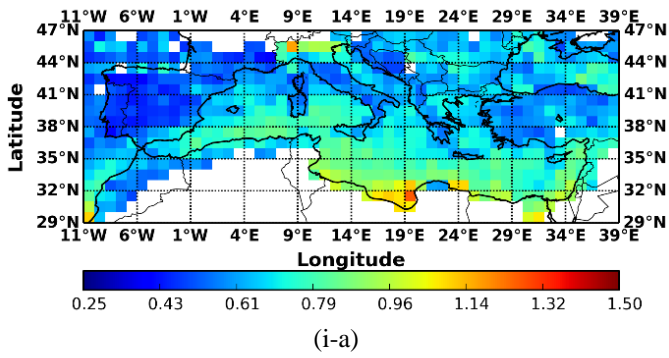
1791

1792

1793

1794

1795



1796 **Figure 7:** Geographical distributions of the intensity (in terms of AOD_{550nm}) of: (i) strong and (ii) extreme desert dust
 1797 episodes, averaged for the periods: (a) Mar. 2000 – Feb. 2013 (MODIS-Terra) and (b) 2003 – 2012 (MODIS-Aqua), over
 1798 the broader area of the Mediterranean basin.

1799

1800

1801

1802

1803

1804

1805

1806

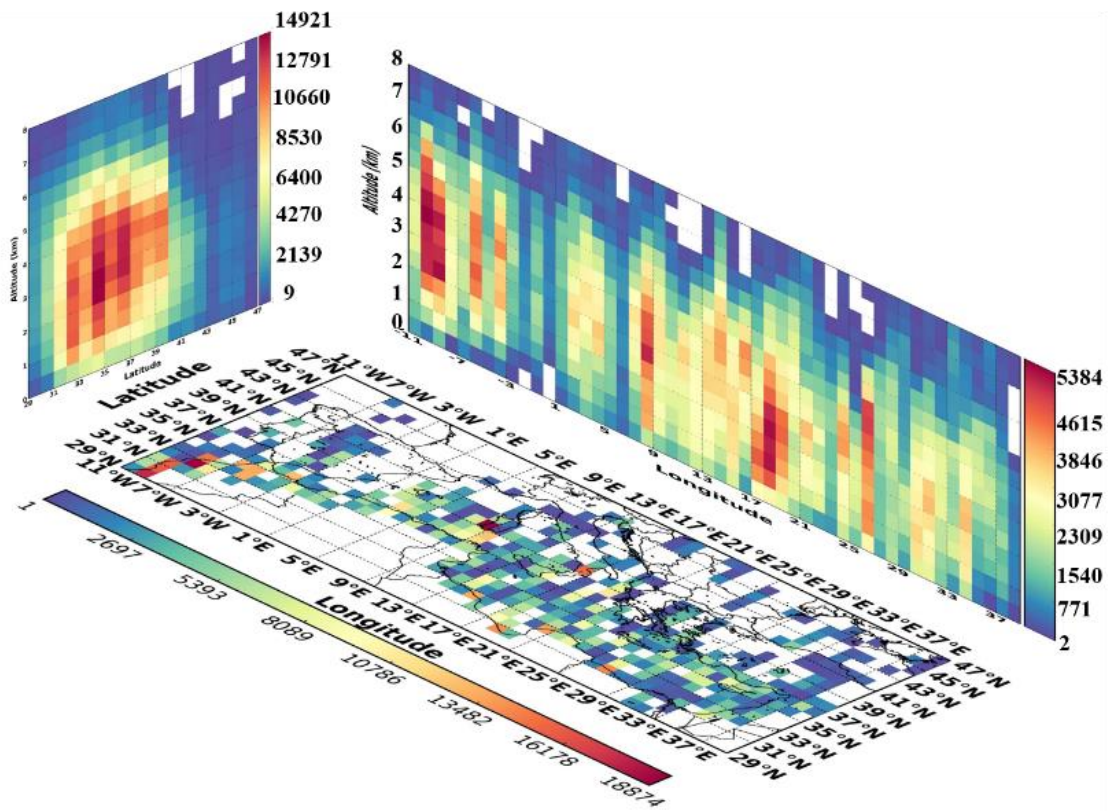
1807

1808

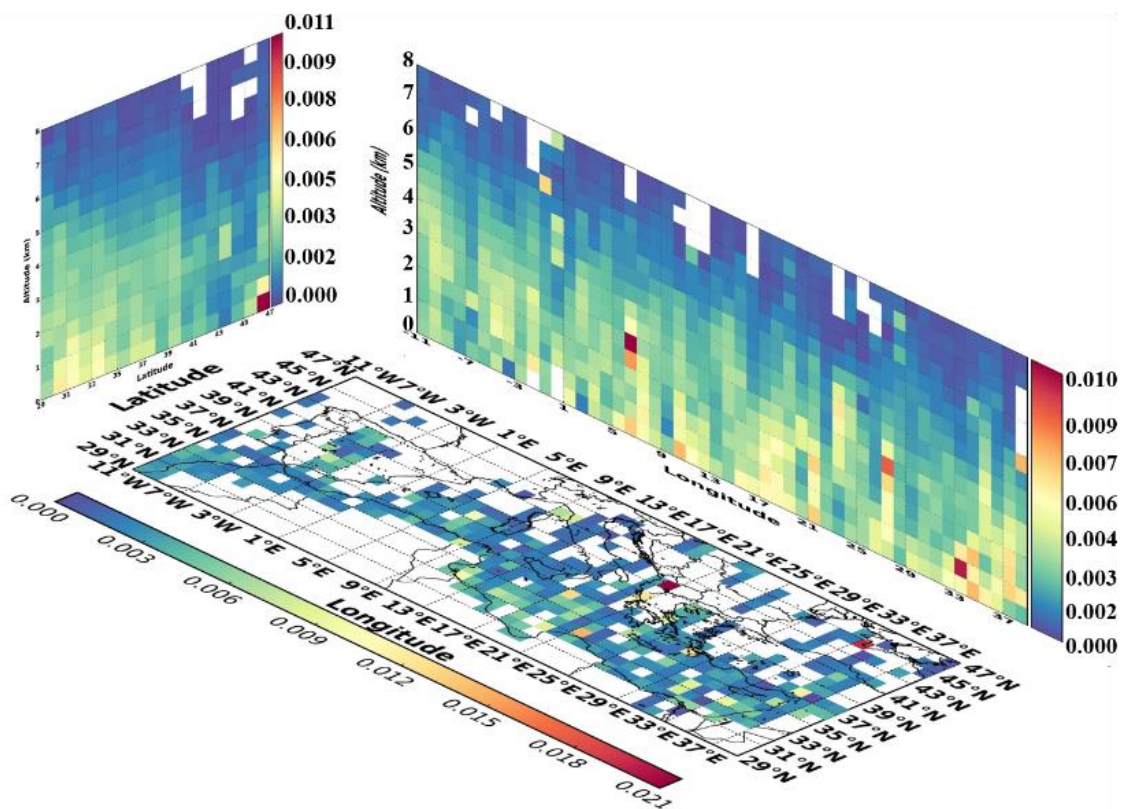
1809

1810

1811

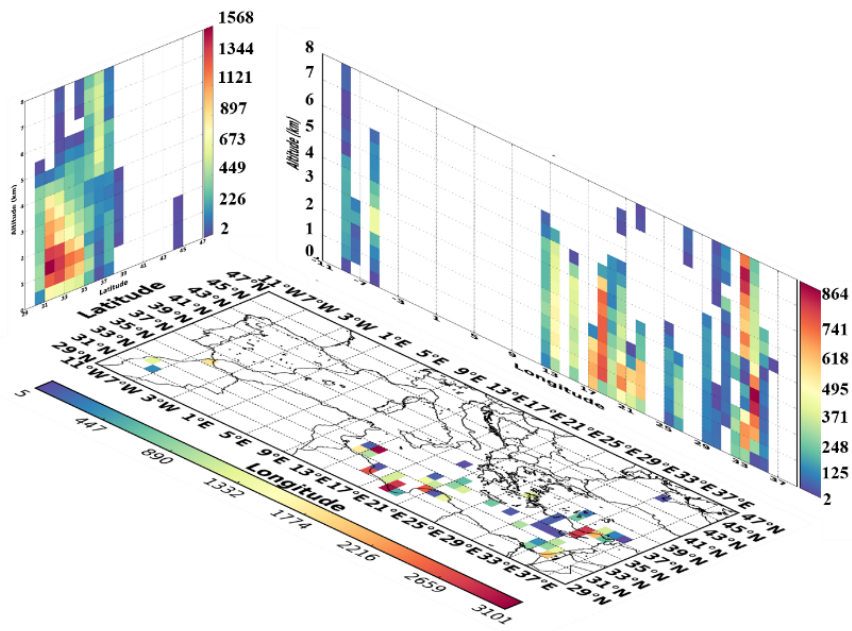


(i)

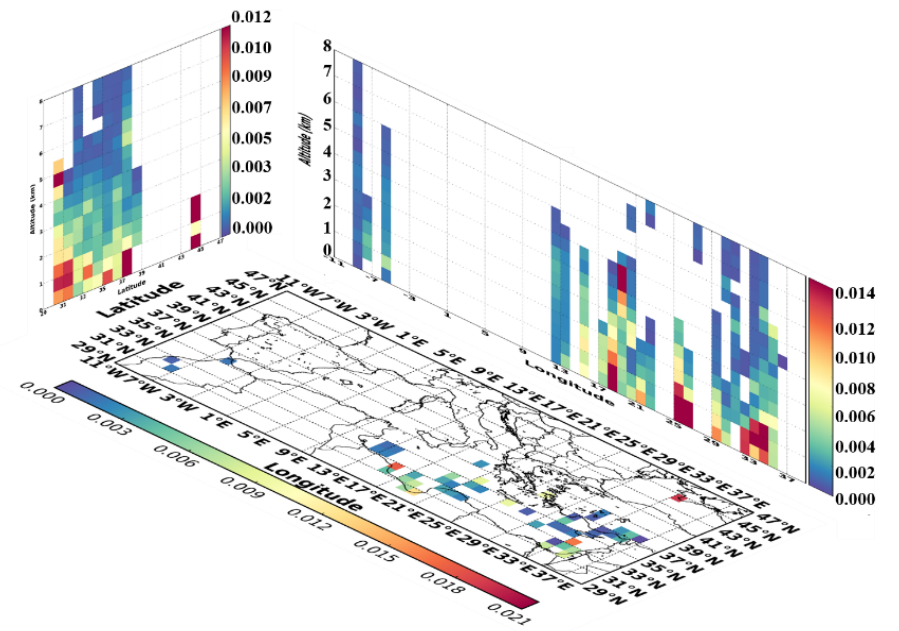


(ii)

Figure 8: Three dimensional structure of the: (i) overall number of dust and polluted dust observations and (ii) total backscatter coefficient at 532 nm (in $\text{km}^{-1} \text{sr}^{-1}$), over the broader Mediterranean basin under *DD* episodes conditions, based on CALIOP-CALIPSO vertical resolved retrievals for the period Jun. 2006 – Feb. 2013.

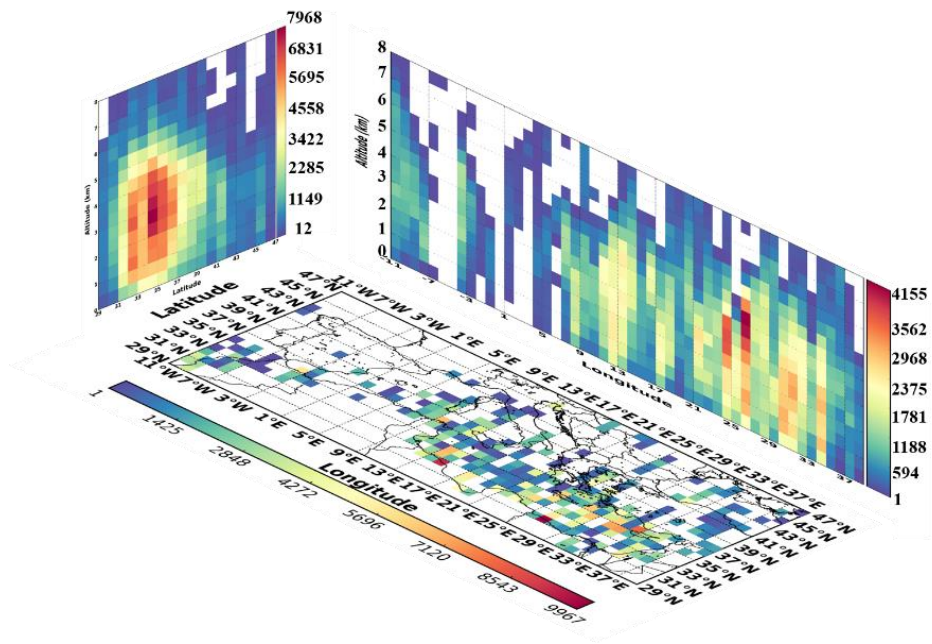


(i-a)

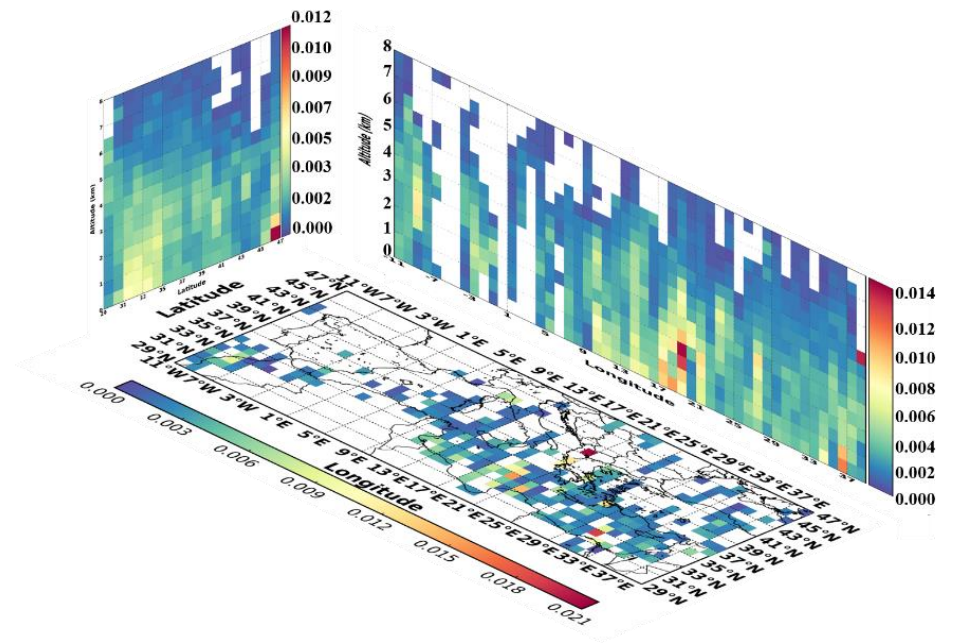


(i-b)

Figure 9: Three dimensional representation of the: (a) overall number of dust and polluted dust observations and (b) total backscatter coefficient at 532 nm (in $\text{km}^{-1} \text{sr}^{-1}$), over the broader Mediterranean basin, under *DD* episodes conditions, for: (i) winter, (ii) spring, (iii) summer and (iv) autumn based on CALIOP-CALIPSO vertical resolved retrievals, over the period Jun. 2006 – Feb. 2013.

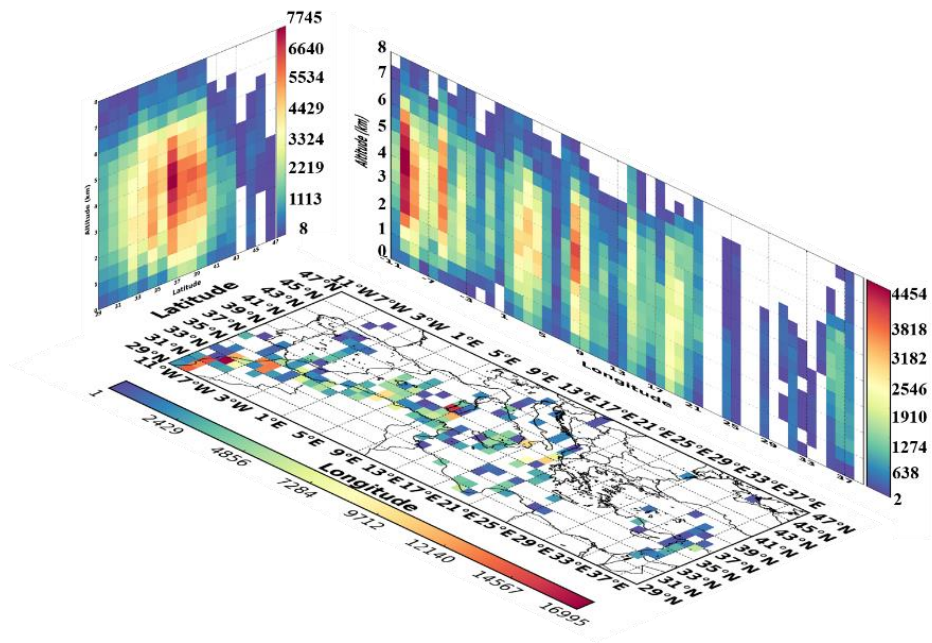


(ii-a)

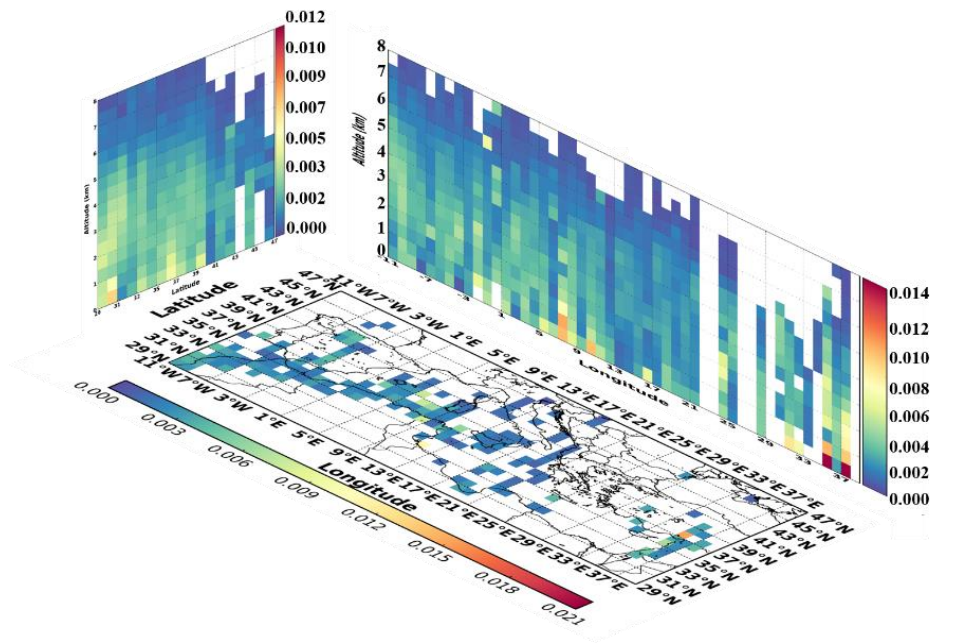


(ii-b)

Figure 9: Continued.

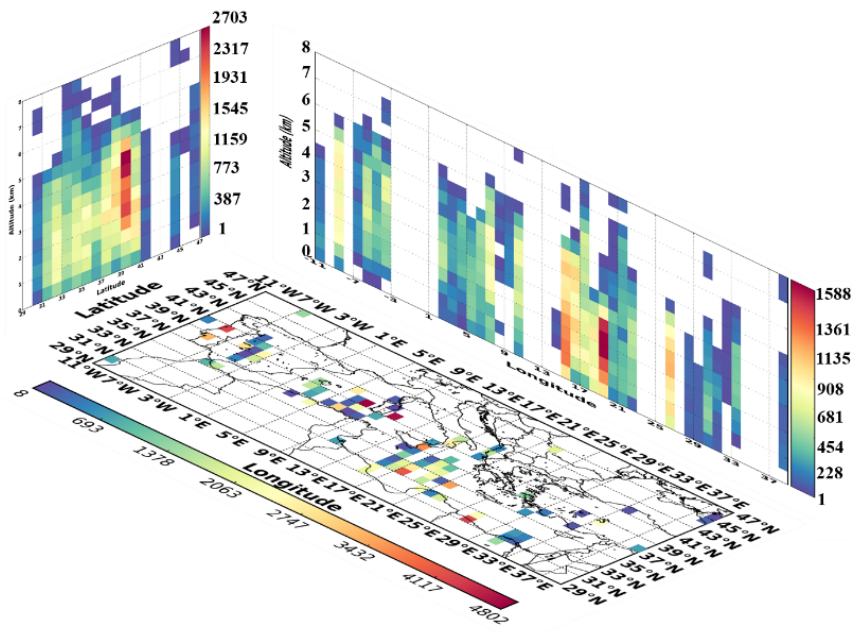


(iii-a)

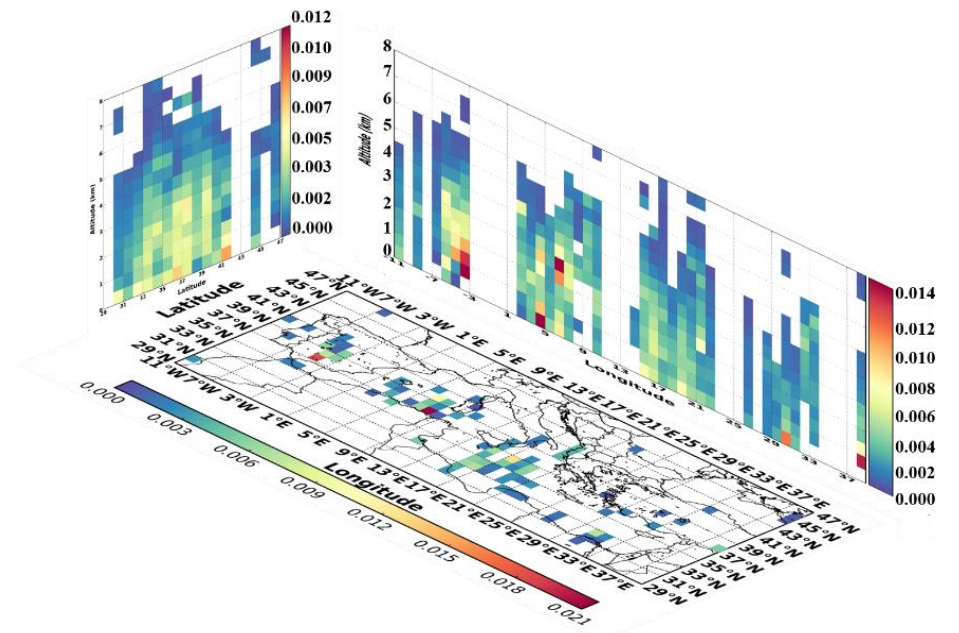


(iii-b)

Figure 9: Continued.

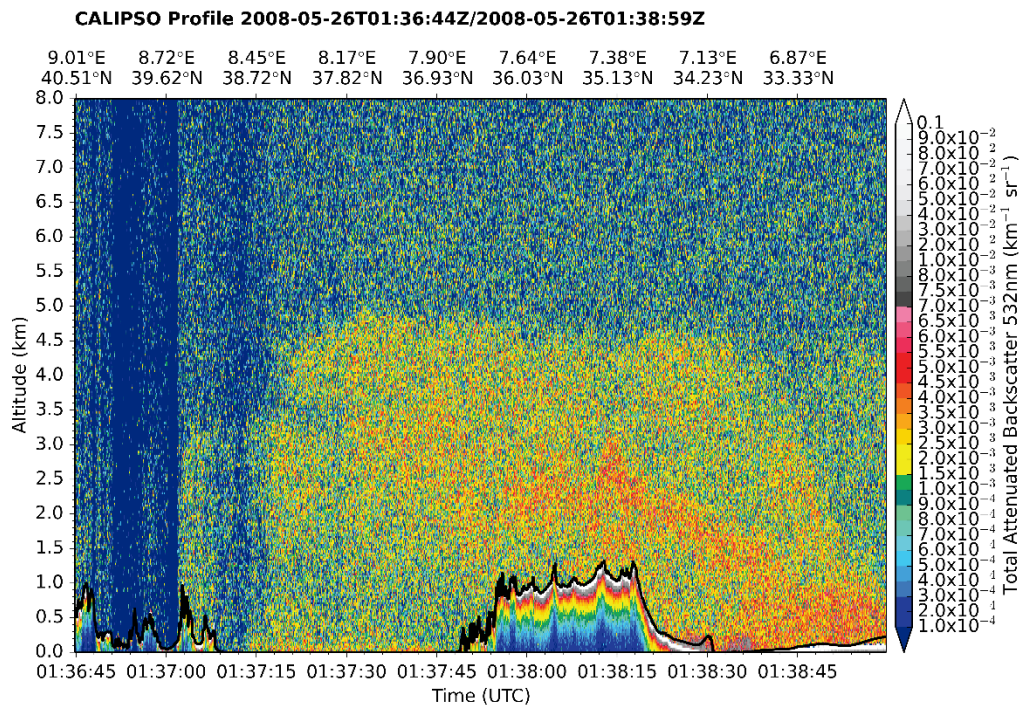


(iv-a)



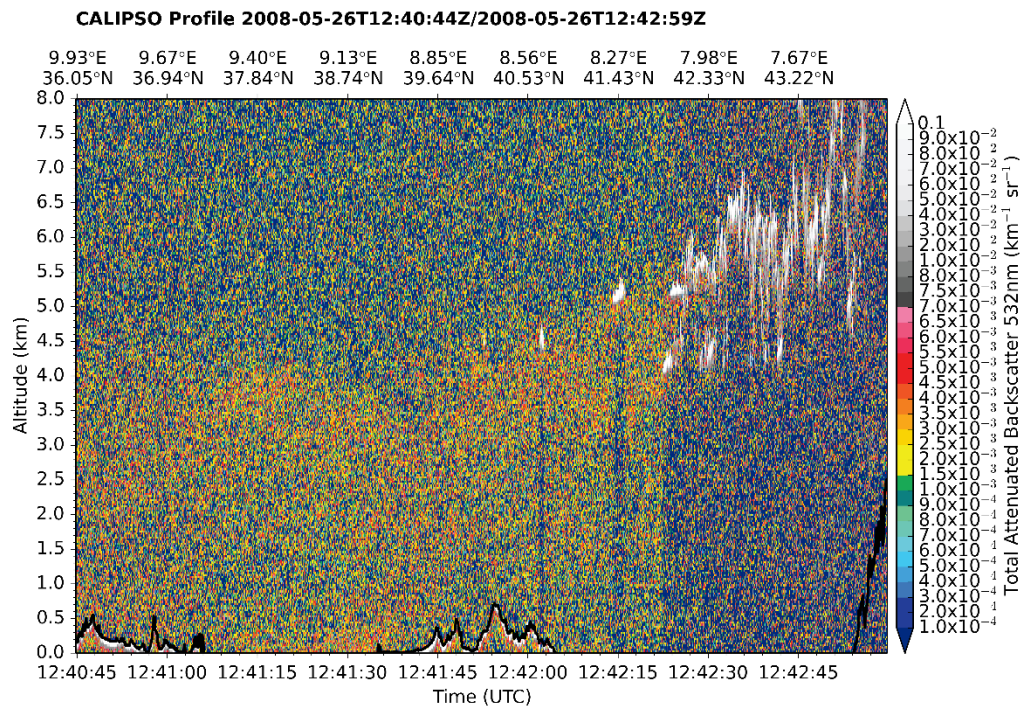
(iv-b)

Figure 9: Continued.



1832

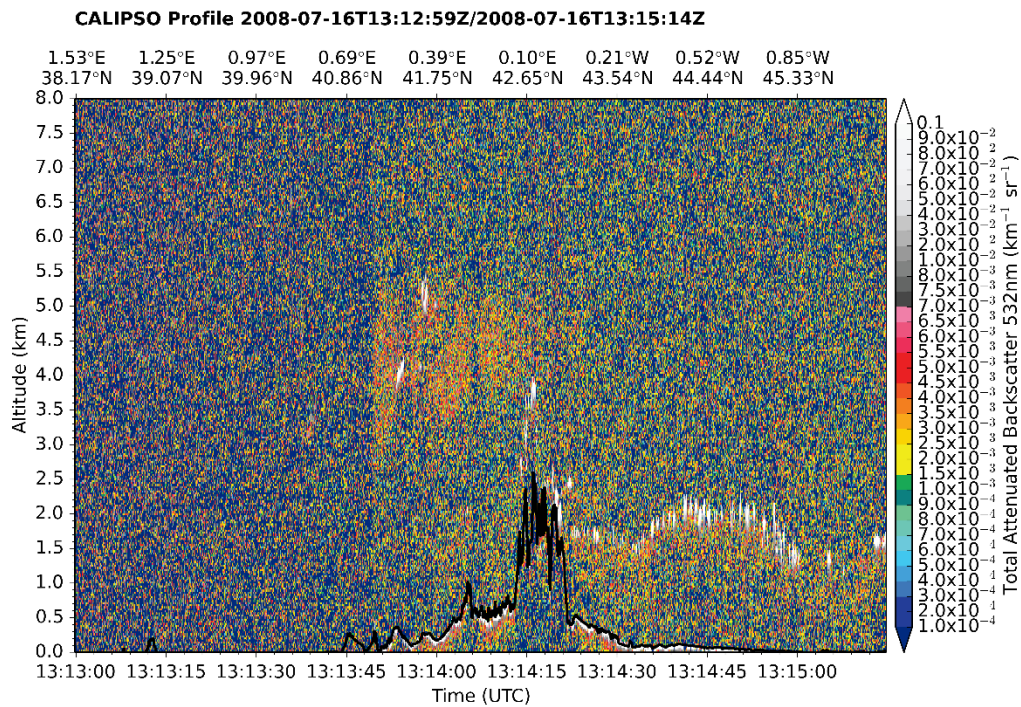
(i)



1833

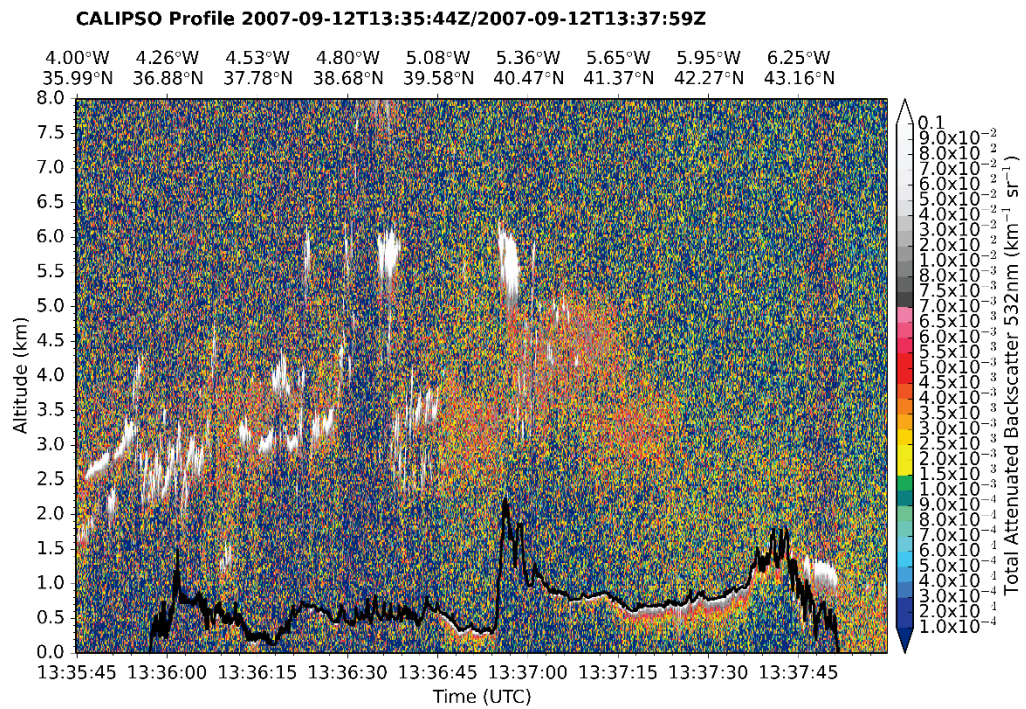
(ii)

1834 **Figure 10:** Cross sections of the total backscatter coefficient at 532 nm (in $\text{km}^{-1} \text{sr}^{-1}$) vertical profiles along the CALIOP-
 1835 CALIPSO track during: (i) nighttime and (ii) daytime, on 26th May 2008, over the station Censt (Lat: 39.064, Lon: 8.457).
 1836 The black thick solid line represents the surface elevation.



1837

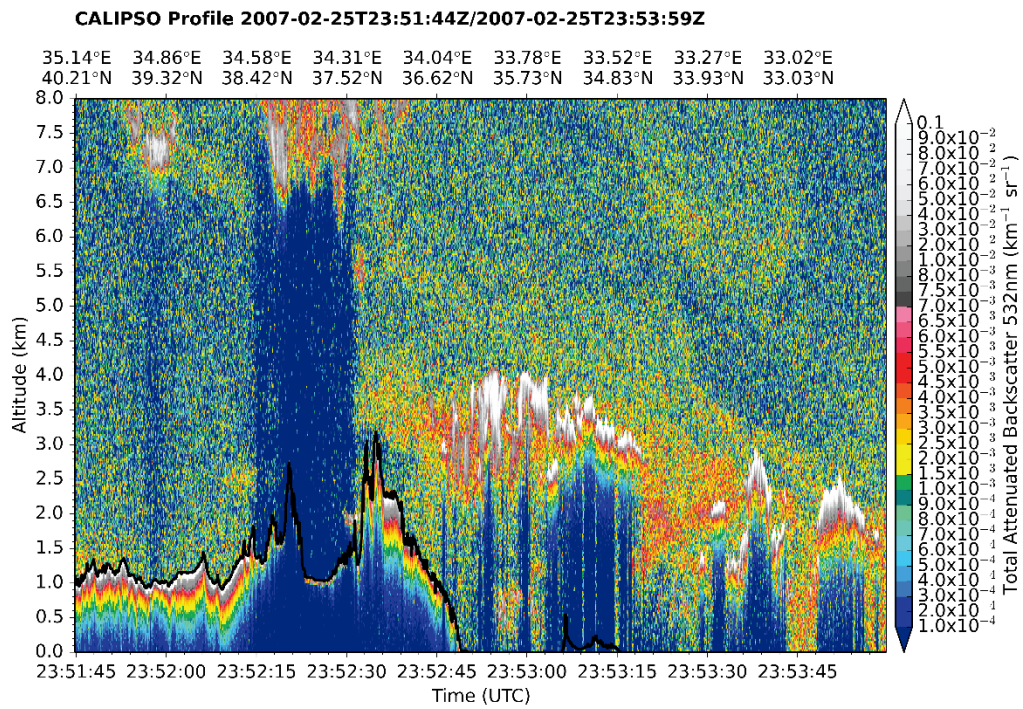
(i)



1838

(ii)

1839 **Figure 11:** Cross sections of the total backscatter coefficient at 532 nm (in $\text{km}^{-1} \text{sr}^{-1}$) vertical profiles along the CALIOP-
 1840 CALIPSO track during daytime over the stations: (i) Els Torns (Lat: 41.395, Lon: 0.721) on 16th July 2008 and (ii) San
 1841 Pablo (Lat: 39.525, Lon: -4.353) on 12th September 2007. The black thick solid line represents the surface elevation.



1842

1843 **Figure 12:** Cross section of the total backscatter coefficient at 532 nm (in km⁻¹ sr⁻¹) vertical profiles along the CALIOP-
 1844 CALIPSO track during nighttime over the station Agia Marina (Lat: 35.039, Lon: 33.058) on 25th February 2007. The black
 1845 thick solid line represents the surface elevation.

1846

1847

1848

1849

1850

1851

1852

1853